MACHINING AND CHATTER AVOIDANCE: PREDICTIVE ANALYTICS AND UNCERTAINTY ANALYSIS

by

Maryam Hashemitaheri

A dissertation submitted to the faculty of
The University of North Carolina at Charlotte
in partial fulfillment of the requirements
for the degree of Doctor of Philosophy in
Mechanical Engineering

Charlotte

2023

Approved by:

Dr. Harish Cherukuri

Dr. Brigid Mullany

Dr. Konstantinos Falaggis

Dr. Taufiquar R. Khan

ABSTRACT

MARYAM HASHEMITAHERI. Machining and Chatter Avoidance: Predictive Analytics and Uncertainty Analysis. (Under the direction of DR. HARISH CHERUKURI)

The main focus of this study is on chatter avoidance during machining. Self-excited regenerative vibration or “chatter" is a significant obstacle in machining which results in poor surface quality and damage to the tool, workpiece, and even machine. To avoid chatter, usually, a 2D diagram called Stability Lobe Diagram (SLD) is constructed to plot the depth of cut limit vs. the spindle speed. The SLD depends on the cutting parameters such as start and exit angle, the number of flutes, cutting force coefficients, and structural dynamics parameters such as the natural frequencies, stiffness, and damping ratios. Here, a few sub-problems on the chatter problem are investigated, as follows. This study covers the prediction of the specific cutting force and the maximum tool temperature during machining. Assuming the machine is working under stable conditions and has parameters like rake angle, chip thickness, and cutting speed, is it possible to build a Machine Learning (ML) model to predict the cutting force and the tool temperature? Here, different ML algorithms e.g. Support Vector Machine (SVM) and Gaussian Process Regression (GPR) are utilized and the results are compared for performance evaluation. In addition, this dissertation focuses on the inverse problem in chatter avoidance. Having the cutting and structural dynamics parameters, one can construct the SLD. But having the SLD, and fixing the cutting parameters, is it possible to get structural dynamics parameters such as frequency, stiffness, and damping ratio? The main motivation here is that theoretically, chatter can be avoided using the optimal values of spindle speed and depth of cut based on physic-based SLD. But in practice, there is a gap between the empirical results and what the theory supports. This happens because there are discrepancies between the structural dynamics parameters in idle (zero speed) and the dynamic states of the machine. Thus, to address this issue, in-process structural dynamics parameters are extracted using a multivariate Newton method approach and the empirical data sets. Finally, this work includes defining and measuring the uncertainty of each structural dynamics parameter derived through the inverse approach. In other words, this study investigates to what extent does each input parameter's uncertainty lead to the uncertainty in the SLD? The results derived from the algorithm were used to discover the sensitivity of the stability boundary with respect to each parameter. Two different methods were utilized for this purpose. Although the stability border shifts as any structural dynamics parameter changes, the results show that the natural frequency is the most influential parameter.

ACKNOWLEDGEMENTS

This work would have not been possible without the generous support of the Department of Mechanical Engineering and Engineering Science and the Graduate School at UNC Charlotte. I would like to thank the UNC system research opportunities initiative which provided funding for this research. I am very grateful for all of my advisor support, Dr. Harish Cherukuri, during my time here at UNCC. Also, here I would like to express my gratitude to my Ph.D. committee, Dr. Mullany, Dr. Falaggis, and Dr. Khan.

I cannot thank Shervin enough for all his emotional and technical support. The completion of this work would not have been possible without him. I would also like to thank my dearest friends Tuukka, Koda, Jax, Hana, Azadeh, Abby, and Mahabadi for their support during my time at UNC Charlotte.

TABLE OF CONTENTS

LIST OF TABLES

LIST OF FIGURES

LIST OF ABBREVIATIONS

ANN: Artificial Neural Network.

ARMA: Auto-Regressive Moving Average.

FEM: Finite Element Method.

FRF: Frequency Response Function.

GA: Genetic Algorithm.

GPR: Gaussian Process Regression.

ML: Machine Learning.

MSE: Mean Square Error.

MSLD: Multidimensional Stability Lobe Diagram.

SLD: Stability Lobe Diagram.

SVM: Support Vector Machine.

SVR: Support Vector Regression.

LIST OF RELATED PUBLICATIONS

Hashemitaheri M, Mittal R, Cherukuri H, Singh R. Extracting the In-Process Structural Dynamics Parameters in Micro-Milling Operations. In International Manufacturing Science and Engineering Conference 2022 Jun 27 (Vol. 85819, p. V002T05A052). American Society of Mechanical Engineers. [9]

Hashemitaheri M, Mekarthy SM, Cherukuri H. Prediction of specific cutting forces and maximum tool temperatures in orthogonal machining by Support Vector and Gaussian Process Regression Methods. Procedia Manufacturing. 2020 Jan 1;48:1000-8. [10]

Mekarthy SM, Hashemitaheri M, Cherukuri H. A combined finite element and machine learning approach for the prediction of specific cutting forces and maximum tool temperatures in machining. Electronic Transactions on Numerical Analysis. 2022;56:66-85. [6]

CHAPTER 1: INTRODUCTION

During milling operations, material removal rates are affected by the selection of spindle speed and depth of cut. Poor selection of these parameters can result in chatter or suboptimal material removal rates. Stability lobe diagrams (SLDs) are often used to select appropriate values for spindle speed and depth of cut to avoid chatter during milling. Figure 1.1 shows an example of the SLD.

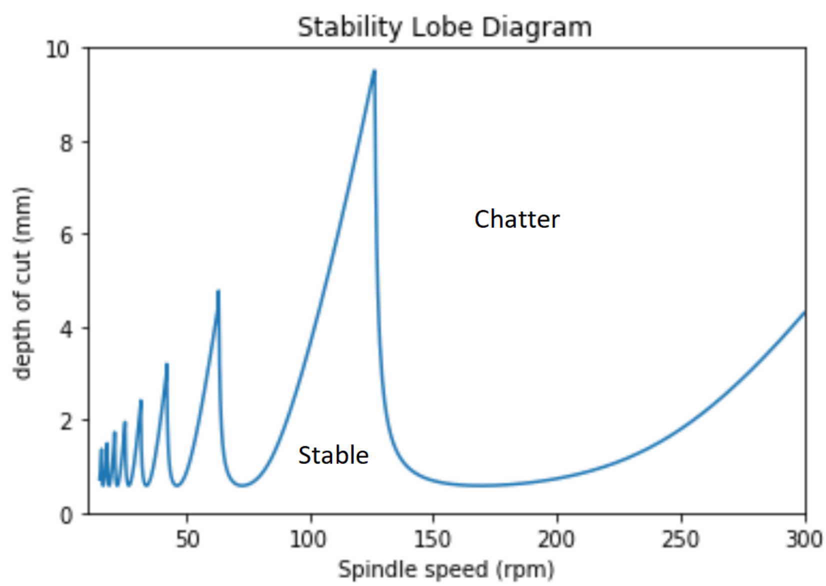

Figure 1.1: Stability Lobe Diagram.

The stability lobe diagram distinguishes the stable and unstable regions by the stability boundary. As this boundary is a plot of the axial depth of cut versus the spindle speed, any combination of these two machining parameters below the boundary represents the stable cut situation while those above reflect the possible unstable settings.

To generate the analytical stability boundary, the Zero-Order Approach (ZOA) on the frequency domain is used. In this approach, the cutting forces are transformed from the time domain into the frequency domain using Fourier transformation and only the mean component of the Fourier series is utilized in the calculation. The dynamic milling expression depends on cutting force coefficients, start and exit immersion angles of the tool to and from the cut, and frequency response function of the structure at tool tip. Assuming a system is critically stable at each chatter frequency value around the structural modes, the critical depth of cut can be derived.

Then, the spindle speed corresponding to each real-valued critical depth of cut can be calculated. Having the pairs of spindle speeds and depths of cut, the SLD is generated by selecting the minimum value of depth of cut for each spindle speed. The details of SLD generation are discussed in Section 2.1.

The stability lobe diagram is defined by knowing the structural dynamics and cutting parameters. Structural dynamics parameters include natural frequency, stiffness, and damping ratio for each mode in feed and cross-feed direction. And cutting parameters include number of flutes, start and exit angle of tool, and specific cutting force coefficients. Structural dynamics parameters or modal parameters are calculated in the idle state of the machine (zero speed) by impact hammer test. However, discrepancies are observed between the structural dynamics parameters calculated at zero speed and during machining conditions, as they vary during the machine operation. As a result of such discrepancies, the stability lobe diagram generated based on the knowledge of the idle state of the machine is not reliable. To generate an in-process stability lobe diagram, the in-process structural dynamics parameters are needed. Since measuring structural dynamics parameters under cutting conditions is difficult, a new method is proposed to determine in-process structural dynamics parameters based on a multivariate Newton-Raphson method. The idea of this hybrid approach is to combine a physics-based process model with the experimental results. By fixing the cutting parameters, the structural dynamics parameters are determined using the proposed inverse approach.

To formulate the governing delay differential equations, the structural dynamics and cutting parameters are needed. The analytical solution for the delay differential equation in frequency domain provides the stability limit. However, any uncertainty in the input parameters (structural dynamics and cutting parameters) results in placing uncertainty on the stability boundary. In this study, the effect of the uncertainty of the structural dynamics parameters on the stability boundary is investigated.

This work also covers the feasibility of machine learning algorithms for the prediction of cutting force and the maximum tool temperature during orthogonal machining. It is important to predict specific cutting forces prior to the actual machining process, since these are used to calculate torque and estimate the power. Also, improving the surface quality and tool life requires the knowledge of tool temperature. Although the finite element method is commonly used to estimate these parameters, simulation-based studies are computationally expensive and it is impractical to conduct them for a wide range of parameters. Thus, here some machine learning algorithms are implemented to predict cutting force and maximum tool temperature. Two methods, namely the Support Vector Regression and the Gaussian Process Regression, are presented in this study.

This thesis contains five chapters, with this chapter including a brief introduction. Chapter 2 (background), discusses regenerative chatter in milling operation and how structural dynamics and cutting parameters are used to provide an analytical solution in the frequency domain for the governing delay differential equation of the systems and develop a stability lobe diagram to avoid chatter. Chapter 3 contains the literature review. Chapter 4 describes, in brief, the methodology for the following sub-problems.

1. Machine Learning (ML) models: Specific cutting forces and maximum tool temperatures prediction during orthogonal machining by Support Vector regressor

(SVR) and Gaussian Regression Process (GPR).

2. A multivariate Newton method for the inverse problem: Usually the stability lobe diagram is constructed having the machining structural parameters. But this study covers the inverse problem: Having the SLD, is it possible to retrieve the structural parameters? Here the possibility of extracting the in-process structural dynamics parameters is examined, given the SLD.

3. Uncertainty and Sensitivity Analysis in Stability Lobe Diagram: This work includes defining and measuring the uncertainty of each structural dynamics parameter derived through the inverse approach. Here the main question is: To what extent, the uncertainty of each input parameter leads to the uncertainty in the SLD?

The results for each of the sub-problems are presented in each section right after the methodology is explained. This is followed by Chapter 5 where the work is summarized and conclusions are provided.

CHAPTER 2: BACKGROUND

Machine tool vibrations or chatter have been always been the principal obstacle to productivity in machining industry, since it results in non-smooth surface of the workpiece (Figure 2.1), tool wear or even damage to the tool. Chatter can be avoided by choosing proper values for spindle speed and depth of cut using the stability lobe diagram. Based on the Stability lobe diagram, at each value of spindle speed, there is a specific value of depth of cut which exceeding that value will result in an unstable cut, that unfavorably affects the surface quality, causes excessive or uneven tool wear, causes damage to dynamically moving parts of the machine, and impacts the optimum material removal rate, and leads to loss of productivity.

(a) No chatter.

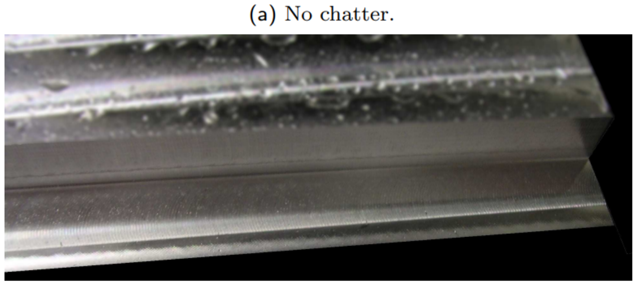

(b) Chatter.

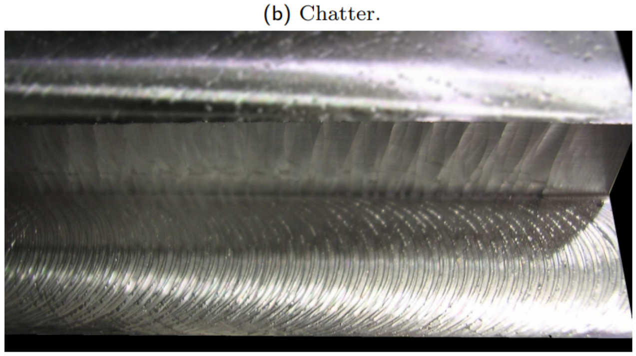

Figure 2.1: The workpiece surface with and without chatter marks [3].

Regenerative chatter is the most common type of chatter that happens during most machining cases. During milling, cutting forces could cause displacement between the tool and the workpiece, and result in tool vibration. Due to the tool's structural vibration, a wavy surface is created on the workpiece surface, as shown in Figure 2.2. Therefore, during the next tooth passing period, the tool faces the wavy surface imprinted by the previous teeth and creates a new wavy surface. The waviness imprinted on the surface could make the cutting force change rapidly, as the chip thickness changes. The chatter built up based on the phase difference between waves is named regenerative chatter.

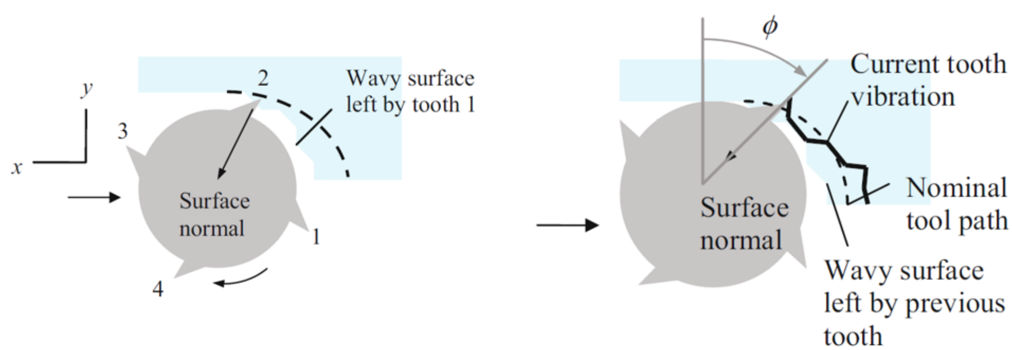

Figure 2.2: Regeneration in milling [4].

The dynamics of the milling process for chatter prediction is defined by the delay differential equations to include the regenerative effect in the model. A significant amount of research has been conducted to obtain the proper stability properties for milling. The stability properties can be calculated in the time domain. Although many details can be included in the calculation in time domain simulations, the computational time and cost can be high. Thus, the frequency domain solution is the fastest solution to determine the stability properties. The stability lobe diagram is generated based on knowing two different categories of parameters: structural dynamics and cutting parameters. Cutting parameters are comprised of number of teeth, start and exit angle, and tangential and radial coefficients. Structural dynamics parameters can be determined by modal analysis experimentally on the combination of tool, tool-holder, and spindle. A common approach is performing impact hammer test at the tip of the tool. Vibration signals resulting from the tool excitement are collected by an accelerometer. Structural dynamics parameters are extracted by frequency response function (FRF) analysis. These parameters include the natural frequency, stiffness, and damping ratio.

There are two physics-based models to derive analytical solutions in the frequency domain, namely the average tooth angle and the Fourier series approach. The average tooth angle approach is introduced by Tlusty [11, 12, 13] as an analytical solution in the frequency domain to obtain the stability boundary. In this method, they considered an average angle of the tooth in the cut to overcome the issue of time-variant cutting force direction. In addition, direction orientation factors were defined to project the cutting forces onto the surface normally. The directional orientation factors are used to calculate the oriented frequency response function.

Altintas and Budak [14] represented another method in the frequency domain, named the Fourier series approach, to analyze the stability of the milling process. They suggested a different approach to solving the issue of the time dependency of the cutting forces. In their method, Fourier series expansion of the time-dependent coefficients in the dynamic equations is implemented. In the following, a brief review of analytical stability equations using the Fourier series approach is presented, since this approach will be used in the present work to determine the stability boundary.

2.1 Fourier Approach to Calculate Stability Lobe Diagram in Milling

In the following, the calculation of the stability lobe diagram in milling based on the Fourier approach is explained [5]. It is assumed that the tool is non-rigid. The milling system is considered as a 2 degree-of-freedom system in directions X and Y as shown in Figure (2.3).

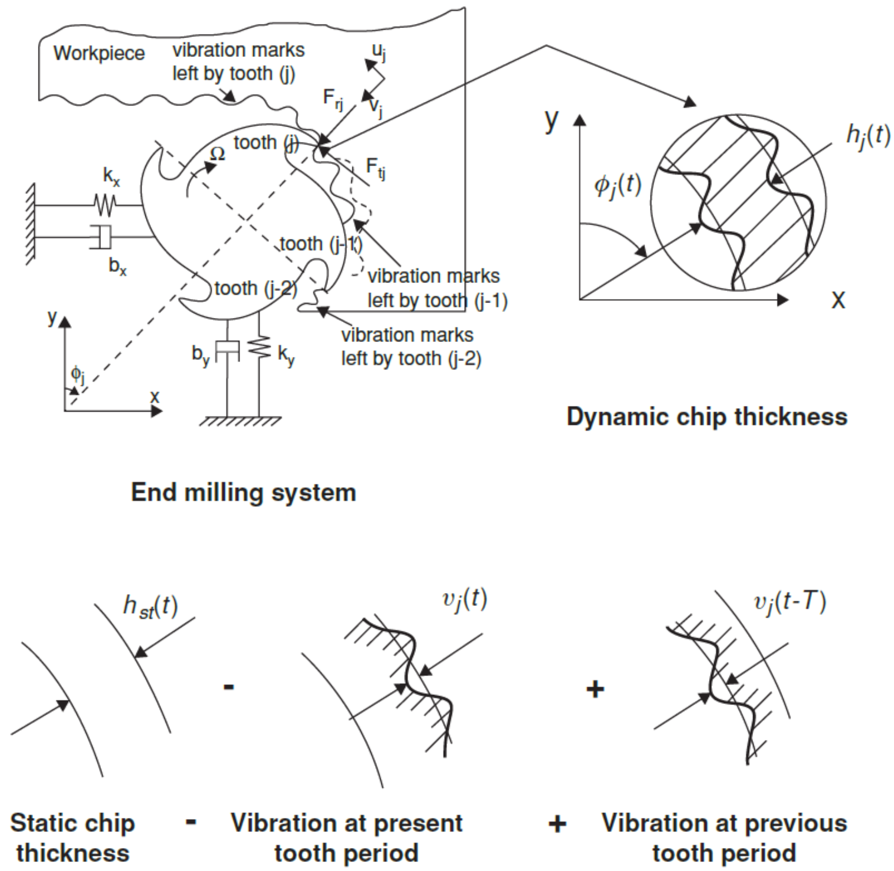

Figure 2.3: 2-DOF milling system [5].

The chip thickness during the milling can be expressed as

$$h(\phi_j) = f_t \sin\phi_j(t) - [-x(t)\sin\phi_j(t) - y(t)\cos\phi_j(t)] \\ + [-x(t-T)\sin\phi_j(t) - y(t-T)\cos\phi_j(t)] \tag{2.1}$$

where instantaneous immersion angle of tooth j varies with time $\phi_j(t) = \Omega t$. Also, f_t is feed per tooth which is defined by feed rate (f), spindle speed (Ω) and number of teeth (N):

$$f_t = \frac{f}{\Omega N} \tag{2.2}$$

The first term in the Equation (2.1) can be dropped, as it explains the static chip load and does not contribute to the dynamic chip load calculation. Therefore, the dynamic chip load can express as:

$$h(\phi_j) = [\Delta x \sin \phi_j + \Delta y \cos \phi_j] g(\phi_j)$$
$$\begin{cases} g(\phi_j) = 1 \quad \phi_{st} < \phi_j < \phi_{ex} \\ g(\phi_j) = 0 \quad \phi_j < \phi_{st} or \phi_j > \phi_{ex} \end{cases} \tag{2.3}$$

where Δx and Δy are the differences between the dynamic displacement of the current

and previous teeth in X and Y directions, respectively. The tangential (F_{tj})and radial ($F_r j$) cutting forces on tooth j are determined as follows

$$\begin{aligned} F_{tj} &= k_t b h(\phi_j) \\ F_{rj} &= k_r F_{tj} \end{aligned} \tag{2.4}$$

where b is depth of cut, and k_t and k_r are tangential and radial cutting coefficients, respectively. So the cutting forces in X and Y directions are given by

$$\begin{aligned} F_{xj} &= -F_{tj} \cos \phi_j - F_{rj} \sin \phi_j \\ F_{yj} &= +F_{tj} \sin \phi_j - F_{rj} \cos \phi_j \end{aligned} \tag{2.5}$$

Total dynamic force is determined by summing forces by all the teeth in each direction.

$$\begin{aligned} F_x &= \sum_{j=0}^{N-1} F_{xj}(\phi_j) \\ F_y &= \sum_{j=0}^{N-1} F_{yj}(\phi_j) \end{aligned} \tag{2.6}$$

Cutting forces expression can be rearrenged by substituting Equations (2.4) and (2.3) into Equation (2.5):

$$\begin{Bmatrix} F_x \\ F_y \end{Bmatrix} = \frac{1}{2} b k_t \begin{bmatrix} \alpha_{xx} & \alpha_{xy} \\ \alpha_{yx} & \alpha_{yy} \end{bmatrix} \begin{Bmatrix} \Delta x \\ \Delta y \end{Bmatrix} \tag{2.7}$$

where α terms are directional dynamic milling force coefficients are defined as

$$\begin{aligned} \alpha_{xx} &= \sum_{j=0}^{N-1} -g_j[\sin 2\phi_j + k_r(1-\cos 2\phi_j)] \\ \alpha_{xy} &= \sum_{j=0}^{N-1} -g_j[(1+\cos 2\phi_j) + k_r \sin 2\phi_j] \\ \alpha_{yx} &= \sum_{j=0}^{N-1} -g_j[(1-\cos 2\phi_j) - k_r \sin 2\phi_j] \\ \alpha_{yy} &= \sum_{j=0}^{N-1} -g_j[\sin 2\phi_j - k_r(1+\cos 2\phi_j)] \end{aligned} \tag{2.8}$$

Since the angular position of parameters varies with time, Equation 2.7 can be defined in the time domain as follows:

$$\{F(t)\} = \frac{1}{2} b k_t [A(t)]\{\Delta(t)\} \tag{2.9}$$

By taking the Fourier transform of Equation (2.9), the time domain equation can be expressed in the frequency domain as follows

$$\begin{aligned} \mathcal{F}\{F(t)\} &= \frac{1}{2} b k_t \mathcal{F}\{[A(t)]\{\Delta(t)\}\} = \frac{1}{2} b k_t \mathcal{F}\{[A(t)]\} * \mathcal{F}[\{\Delta(t)\}] \\ \{F(\omega)\} &= \frac{1}{2} b k_t \{[A(\omega)] * \{\Delta(\omega)\}\} \end{aligned} \tag{2.10}$$

The vibration vectors in time domain at current time (t) and the previous tooth period $(t-T)$ are determined as

$$\begin{aligned} \{Q\} &= \{x(t) \quad y(t)\}^T \\ \{Q_0\} &= \{x(t-T) \quad y(t-T)\}^T \end{aligned} \tag{2.11}$$

The vibration vectors in frequency domain can be expressed as

$$\begin{aligned} \{Q(\omega)\} &= [\Phi(i\omega)]\{F(\omega)\} \\ \{Q_0(\omega)\} &= e^{-i\omega T}\{Q(i\omega)\} \end{aligned} \tag{2.12}$$

where $[\Phi(i\omega)]$ is frequency response function of tool and described as

$$[\Phi(i\omega)] = \begin{bmatrix} \Phi_{xx}(i\omega) & \Phi_{xy}(i\omega) \\ \Phi_{yx}(i\omega) & \Phi_{yy}(i\omega) \end{bmatrix} \tag{2.13}$$

Substituting Equation (2.12) into $\{\Delta\} = \{(x - x_0) \quad (y - y_0)\}^T$ yields

$$\{\Delta(i\omega)\} = \{Q(i\omega)\} - \{Q_0(i\omega)\} = [1 - e^{-i\omega T}][\Phi(i\omega)]\{F(\omega)\} \tag{2.14}$$

Substituting Equation (2.14) into Equation (2.10) gives the rearranging of the dynamic milling force equation in the frequency domain:

$$\{F(\omega)\} = \frac{1}{2}bk_t\{[A(\omega)] * [1 - e^{-i\omega T}][\Phi(i\omega)]\{F(\omega)\}\} \tag{2.15}$$

$[A(t)]$ is periodic at tooth passing frequency $\omega_T = N\Omega$ or tooth period $T = 2\pi/\omega_T$. That means $[A(t)] = [A(t - T)]$; thus, it can be expressed by Fourier series as

$$[A(\omega)] = \mathcal{F}[A(t)] \sum_{r=-\infty}^{+\infty} [A_r]\delta(\omega - r\omega_T) = \sum_{r=-\infty}^{+\infty} [A_r]e^{ir\omega_T t} \tag{2.16}$$

where δ and $\mathcal{F}$ represent Direct delta function and Fourier transformation, respectively. So, Fourier coefficients are defined as

$$[A_r] = \frac{1}{T}\int_0^T [A(t)]e^{-ir\omega_T t}dt = \frac{N}{2\pi}\begin{bmatrix} \alpha_{xx}^{(r)} & \alpha_{xy}^{(r)} \\ \alpha_{yx}^{(r)} & \alpha_{yy}^{(r)} \end{bmatrix} \tag{2.17}$$

2.2 Zero-Order Solution of Stability lobe diagram in Milling

To remove the time-dependent terms of Fourier coefficients, only the average component of the Fourier expansion is considered. In other words $r = 0$ in Equation 2.17. Therefore,

$$[A_0] = \frac{1}{T}\int_0^T [A(t)]dt = \frac{N}{2\pi}\begin{bmatrix} \alpha_{xx} & \alpha_{xy} \\ \alpha_{yx} & \alpha_{yy} \end{bmatrix} \tag{2.18}$$

where the α (integrated functions) are given by

$$\begin{aligned} \alpha_{xx} &= \frac{1}{2}[\cos 2\phi - 2k_r\phi + k_r \sin 2\phi]_{\phi_{st}}^{\phi_{ex}} \\ \alpha_{xy} &= \frac{1}{2}[-\sin 2\phi - 2\phi + k_r \cos 2\phi]_{\phi_{st}}^{\phi_{ex}} \\ \alpha_{yx} &= \frac{1}{2}[-\sin 2\phi + 2\phi + k_r \cos 2\phi]_{\phi_{st}}^{\phi_{ex}} \\ \alpha_{yy} &= \frac{1}{2}[-\cos 2\phi - 2k_r\phi - k_r \sin 2\phi]_{\phi_{st}}^{\phi_{ex}} \end{aligned} \tag{2.19}$$

So the dynamic milling equation in Equation (2.15) is reduced as following

$$F(\omega) = \frac{1}{2}bk_t\{[A_0][1 - e^{-i\omega T}][\Phi(i\omega)]\{F(\omega)\}\} \tag{2.20}$$

The roots of characteristic equations are calculated from the determinant:

$$det[[I] - \frac{1}{2}bk_t(1 - e^{-i\omega_c T})[A_0][\Phi(i\omega)]] = 0 \tag{2.21}$$

$$det[[I] + \Lambda[\Phi_0(i\omega_c)]] = 0 \tag{2.22}$$

where ω_c is chatter frequency. The eigenvalue of characteristic function (Equation 2.22) is

$$\Lambda = -\frac{N}{4\pi}bk_t(1 - e^{-i\omega_c T}) \tag{2.23}$$

where the frequency response function (FRF) is

$$[\Phi_0(i\omega_c)] = \begin{bmatrix} \alpha_{xx}\Phi_{xx}(i\omega_c) + \alpha_{xy}\Phi_{yx}(i\omega_c) & \alpha_{xx}\Phi_{xy}(i\omega_c) + \alpha_{xy}\Phi_{yy}(i\omega_c) \\ \alpha_{yx}\Phi_{xx}(i\omega_c) + \alpha_{yy}\Phi_{yx}(i\omega_c) & \alpha_{yx}\Phi_{xy}(i\omega_c) + \alpha_{yy}\Phi_{yy}(i\omega_c) \end{bmatrix} \tag{2.24}$$

Since the FRF is complex, the eigenvalue is complex. By substituting $\Lambda = \Lambda_R + i\Lambda_I$ and $e^{-i\omega_c T} = \cos\omega_c T - i\sin\omega_c T$ in Equation 2.23, the critical depth of cut at chatter frequency is calculated as following

$$b_{lim} = -\frac{2\pi}{Nk_t}[\frac{\Lambda_R(1-\cos\omega_c T) + \Lambda_I \sin\omega_c T}{(1-\cos\omega_c T)} + i\frac{\Lambda_I(1 - cos\omega_c T - \Lambda_R \sin\omega_c T)}{(1-\cos\omega_c T)}] \tag{2.25}$$

Since the depth of cut is a real value, the imaginary part of Equation (2.25) should be zero. Thus, given the chatter frequency, the critical depth of cut can be calculated by

$$b_{lim} = -\frac{2\pi\Lambda_R}{Nk_t}(1+\kappa^2) \tag{2.26}$$

where

$$\begin{aligned} \kappa &= \frac{\Lambda_I}{\Lambda_R} \\ &= \frac{\sin\omega_c T}{1-\cos\omega_c T} \\ &= \frac{\cos(\omega_c T/2)}{\sin(\omega_c T/2)} \\ &= \tan[\pi/2 - (\omega_c T/2)] \end{aligned} \tag{2.27}$$

The phase shift of the eigenvalue is $\psi = \tan^{-1}\kappa$, and tooth passing period can be expressed as $T = \frac{1}{\omega_c}(\pi - 2\psi + 2k\pi)$, where k is the integer number of waves between teeth (i.e. lobes) imprinted on the cut. Also, the phase shift between the inner and outer modulation (present and previous marks) is $\epsilon = \pi - 2\psi$. Therefore, the spindle speed (rev/min) can be calculated by knowing the tooth passing period (T) as follows:

$$T = \frac{1}{\omega_c}(\epsilon + 2k\pi) \tag{2.28}$$

and

$$\begin{aligned} \Omega &= \frac{60}{NT} \\ &= \frac{60\,\omega_c}{N\,(\epsilon\,+2k\,\pi).} \end{aligned} \tag{2.29}$$

CHAPTER 3: Literature Review

During the machining process, the primary obstacle is the chatter phenomenon, which negatively impacts the surface finish quality, causes uneven or excessive tool wear, damages the machine's moving parts, affects the optimal material removal rate, and ultimately results in decreased productivity. There have been numerous research studies conducted to introduce dynamic models to identify stability properties of the cutting process, and also to develop technologies that can detect and prevent chatter in machining processes.

Tlusty [15] introduced a stability law to calculate stability boundary considering the structural dynamics parameters and cutting force coefficients. Tobias [16] applied a similar approach, taking into account the regenerative chatter effect in orthogonal cutting. However, the stability of milling operations cannot be solved by the previous studies, as milling has coupled dynamics in two directions with periodic coefficients. Budak and Altintas [17, 18, 14] introduced an analytical solution in frequency domain to predict the stability properties of the cut as a function of spindle speed and depth of cut. In addition to the frequency domain, some studies have also explored the time domain for calculating stability properties in milling [19, 20, 21]. Altintas et al. [22] provided an overview of numerical simulations and analytical methods used in both time and frequency domains to determine the stability boundary in milling and turning operations.

3.1 The Inverse Problem of Stability Lobe Diagram

Although significant studies have been dedicated to introducing stability law for predicting chatter in both frequency and time domains, there is still a gap between these solutions and reality. To calculate stability boundaries using SLD, it is necessary to measure the dynamic properties of the machining structure accurately. This includes the natural frequency, stiffness, and damping values. While these parameters can be obtained by conducting impact hammer tests on the tip of the cutting tool, studies have shown that these parameters vary significantly during machine loads and lead to inaccurate prediction. Moriwaki and Iwata[23] conducted experiments which demonstrated that the dynamics of the machine change during the cut, and the characteristic parameters of the machine's dynamics differ from those of its idle state. Their experiments showed that these parameters vary due to changes in cutting force loads, which are the result of changes in the depth of cut. A similar study was carried out by Kwiatkowski and Al-Samarai [24] earlier in 1986. Zaghbani and Songmen[25] reported a significant deviation from the stability boundary in static conditions due to changes in stiffness. Numerous studies have been made to derive the in-process structural dynamics parameters, with the aim of obtaining more accurate stability predictions.

Cao et al. [26] showed that the effect of rotational speeds needs to be considered in structural dynamics parameters. They used finite element method to show that the centrifugal forces significantly decrease the stiffness as the speed increases. Cao and Altintas [27] utilized finite element simulations and also carried out some experiments to study the effect of applying preloads and also process loads on machine behavior. Rantatalo et al. [28] measured the structural dynamics parameters of a rotating tool by performing some experiments and using inductive sensors and an electromagnetic actuator. Their results were compared to finite element simulations. The primary challenge in these approaches is modeling the spindle system accurately, which necessitates obtaining the precise geometries of spindle assembly.

Matsubara [29] investigated the changes in the stiffness during the machine operations utilizing magnetic actuators at low spindle speed. Cheng et al. [30] performed an impact hammer test on a standard during rotation to measure the frequency response function. The main drawback of measuring the in-process structural dynamics parameters during machine operation is that artificially exciting the tool may not accurately represent the actual cutting process. This means that the obtained data may not fully reflect the true behavior of the structure and may result in incorrect or misleading conclusions. Frequency Response Function (FRF) at different spindle speeds by the application of the Operational Modal Analysis (OMA) technique is calculated in [31, 25]. However, the OMA-based method is only effective for low spindle speeds.

The inverse stability solution is a possible method to overcome some of the limitations of measuring the in-process structural dynamics during machining loads. Özşahin et al. [32] proposed an inverse approach to identify in-process structural dynamics parameters. They provide analytical solutions by measurement at two different spindle speeds, and calculate changes in damping ratio natural frequency due to the cutting loads. In this study, they used the measurements at zero speed and assumed that the stiffness remains constant during machine loads, which may not always hold true. Grossi et al. [33] also calculated in-process structural dynamics parameters by combining experimental results with the physics-based model. In their proposed method, the difference between the analytical and experimental chatter frequencies and depth of cut are minimized using a Genetic Algorithm (GA). In this study, Similar to [32], it is assumed the stiffness measured in stationary spindle remains constant during material removal and only computes the in-process natural frequency and damping ratio. Suzuki et al. [34] proposed an iterative method to identify in-process machine tool dynamics. For this purpose, they minimize the error between experimental and analytical results by comparing the depth of cuts and phase shifts in each iteration of the algorithm. The phase shift is a function of chatter frequency, number of flutes, and spindle speed. By assigning weights to each difference, the objective function calculates a sum of the error between the predicted chatter frequencies and depth of cuts, and the corresponding values obtained through experimentation. Here, to obtain desirable results, it is essential to include cutting tests with vibration frequencies both above and below the in-process natural frequency (which is not known) to ensure that the calculation of the parameters relies on interpolation rather than extrapolation. Grossi et al. [35] introduced an inverse solution with similar assumptions in [34].

There are also other studies in the literature addressing the inverse problem using either supervised learning or time-series analysis, e.g. Postel et al.[36] built a neural network to identify the cutting coefficient and structural dynamics parameters in milling operations. Their algorithm is trained on experimental cuts to predict underlying parameters. A time-series technique was used by Burney et al.[37, 38] to extract the in-process structural dynamics parameters. In this study, the displacement signal during the cut is analyzed for the ARMA time-series [39] for different cutting operations.

3.2 The Application of Machine Learning in Machining

Many researchers have examined supervised learning methods to determine or predict the system properties and behavior during machining processes. Cho et al. [40] introduce a detection system utilizing Support Vector Regressors (SVRs) to detect the process abnormalities during the milling process given the power consumption and the cutting force. Their study demonstrates that the support vector machine model provides higher accuracy compared to the multilinear regression method. The author concluded that using the support vector regressors can potentially lead to the reduction of production costs and machine downtime. In [41], Jurkovic et al. studied and compared three machine learning models predicting the cutting parameters during high-speed turning operations. They used polynomial (quadratic) regression, support vector regressor, and Artificial Neural Networks (ANNs). In their study, the input parameters included the cutting force and the surface roughness. Their work shows that the polynomial regression and SVR models outperform ANN when predicting surface roughness and cutting force and provide more accurate predictions. Their neural network model only provided higher accuracy in the prediction of the tool life.

The impact of the cutting parameters e.g. the depth of cut and the cutting speed on surface roughness during the face milling process was investigated by Lela et al. [42]. They compared their results from three different machine learning methods, namely support vector regressor, regression analysis, and the Bayesian neural network. The study demonstrated that the Bayesian neural network was the best method in terms of accuracy. However, the other models provided fairly close accuracy. Huseh and Yang in [43] introduced a new diagnosis method for tool breakage during face milling utilizing a support vector machine. Krizek et al. [44] utilized evolutionary computing methods (Genetic Algorithm (GA) & Genetic Programming (GP)), support vector regression, and artificial neural networks to predict the cutting force given input variables such as the cutting depth, the feed rate, and the spindle speed. Kong et al. [45] suggested a new method of predicting tool wear using Gaussian Process Regression (GPR). As their work suggests, the Gaussian process model provided more accurate predictions compared to the artificial neural networks and support vector machines. Zhang et al. [46] worked on a Gaussian process model to predict the surface roughness in end-face milling given different cutting conditions. They achieved an accuracy of 84.3%. Their model reduces of the high cost of the trial-and-error approach to select the appropriate cutting parameters. Liu[47] studied the sequential designs for the quantification of the stability during the machining operation. He achieved a Gaussian process regression model that can predict the stability boundary with 98% accuracy. Lamraoui et al. [48] predicted chatter by analyzing the accelerometer signals during machining process. Two nonlinear neural network models are implemented to learn the dynamic behavior of cutting. Their method predicts chatter accurately, though the algorithm requires massive data.

An online learning approach is proposed by Friedrich et al. [49, 50] to determine the stability boundary during the milling process. In their studies, a multidimensional stability lobe diagram (MSLD) was derived considering depth of cut, width of cut, and spindle speed.The approach, which is a combination of reinforcement learning and the nearest-neighbor-classification model, is able to continuously improve with new input data. The model is validated by analytical solution and capable of predicting with high accuracy. Cherukuri et al. [51] developed a neural network model to classify the stability condition of the turning process. The accuracy obtained with the neural network model shows that the model is well-trained. A Bayesian learning approach is proposed by karandikar et al. [52] to identify the stability boundary. They used an adaptive experimental strategy to optimize operating parameters and maximize the material removal rate. In their method, the model is capable of learning without information regarding the tool frequency response function and cutting force coefficient.

Significant research effort [48, 53, 54, 55, 56, 57, 58, 59] also has been done in chatter detection based on different signals collected during cutting process such as force signal, vibration signals, sound signal, etc. In some of these studies, the features extracted through signal processing methods like wavelet analysis, Hilbert-Huang, etc. are combined with a machine learning algorithm such as neural network, support vector machine, genetic algorithm, etc. to classify stable and unstable cuts. The feasibility of predicting stability boundary in the milling process using support vector machines (SVM) and Artificial neural networks (ANN), and a new method based on kernel interpolation is examined by Denkena et al. [60]. Cutting width, cutting depth, and spindle speed are considered as the inputs for these algorithms. The data was generated with a 10 mm in diameter four-flute tool. The results show that all the models achieved accuracies over 88%. However, the model with kernel interpolation obtained the highest accuracy (94%).

CHAPTER 4: Methodology

The following sub-problems are addressed in this Chapter.

1. Machine Learning (ML) models: Specific cutting forces and maximum tool temperatures prediction during orthogonal machining by Support Vector Regressor (SVR) and Gaussian Regression Process (GPR).

2. A multivariate Newton method for the inverse problem: Usually the stability lobe diagram is constructed having the machining structural parameters. But this study covers the inverse problem: Having the SLD, is it possible to retrieve the structural parameters?

3. Uncertainty and Sensitivity Analysis in Stability Lobe Diagram: This work includes defining and measuring the uncertainty of each structural dynamics parameter derived through the inverse approach. Here the main question is: To what extent, does the uncertainty of each input parameter lead to uncertainty in the SLD?

4.1 Machine Learning Predictive Models

This work includes the prediction of the specific cutting force and the maximum tool temperature during machining [10]. Assuming the machine is working under stable conditions, and having the parameters like rake angle, chip thickness, and cutting speed (as shown in 4.1), is it possible to build a Machine Learning (ML) model to predict the cutting force and the tool temperature? To do that, different ML algorithms e.g. Support Vector Machine (SVM) and Gaussian Process Regression (GPR) are utilized and the results are compared. SVM is a well-known ML method utilized on non-linear numeric data. GPR is an ML model known for its ability to work with small training samples.

The specific cutting force is defined as the cutting force needed to remove the unit area of the workpiece. Here, the prediction of specific cutting forces before the physical machining operation is important to estimate the torque and power requirements. Simultaneously, the knowledge of the maximum tool temperatures will be essential to improving the tool life and the machining operation. For any given cutting tool material and workpiece material, many parameters including but not limited to the rake angle, the cutting speed, and the thickness of the uncut chip can affect those two quantities (tool temperature and the cutting force). A practical model that can incorporate all these parameters and provides reasonably accurate predictions for maximum tool temperature and also the specific cutting force in a real-time scenario is of high practical importance. To do that, one approach is to utilize the finite element method. But, a drawback of that is the significant running time for simulations. Therefore, FE-based approaches are not really practical if the solution is of immediate need. Here, machine learning methods are an attractive alternative, since once ML models are built, they can provide fast or even real-time predictions. Many experts in the field have already applied machine learning techniques to address a variety of problem statements in manufacturing, as discussed in Section 3.2.

Here, two different machine-learning methods are proposed to predict the maximum tool temperature and the cutting forces during orthogonal machining. The main objective in this work is to examine the feasibility of machine learning methods in machining predictive analytics. The two above-mentioned models are utilizing Gaussian Process Regression (GPR) and Support Vector Regression. GPR and SVR are both considered feasible ML models when only a small data sample is available. The synthetic data to train the two models were simulated utilizing the finite element method on orthogonal machining simulations. The details of the finite element simulations are summarized in the next section. The theory behind SVMs and Gaussian Processes is explained in Section 4.1.2 followed by the training of the models, results, and discussion presented in Section 4.3.3.

4.1.1 Generating the data for the Machine Learning methods

Here, only a summary of the finite element model utilized to simulate the training and testing data of the machine learning methods is presented. A more detailed explanation is given in [61].

4.1.1.1 Description of the finite element model

The commercial general-purpose finite element tool (ABAQUS/ EXPLICIT) [62] was utilized to model orthogonal machining of the workpiece made of Aluminum alloy A2024-T351 with the Tungsten Carbide cutting tool. Figure 4.1 illustrates a schematic of the computational model. For the purpose of the model verification, the material properties and the geometry are identical to those utilized by Mabrouki et al. [63]. The cutting tool and the workpiece are meshed utilizing quadrilateral elements (CPE4RT), plane-strain, and triangular elements (CPE3RT) with reduced integration where 22447 total elements are used. The left and bottom nodes in the boundaries of the workpiece are fully constrained. Also, the tool is only given horizontal V_c in the negative x direction. The tool nose radius and the clearance angle are 20 µm and 7°, respectively.

This study assumes that the workpiece constitutive response is governed by the Johnson-Cook constitutive model [63, 64].

The penalty stiffness contact formulation defines the interaction between the chip and the tool. Here, the chip is considered as the slave surface and the tool is considered as the master surface. Moreover, the chip self-contact is also defined using the penalty contact formulation. Inspired by the experimental studies from various experts, the contact region between the cutting tool and the workpiece is divided into two distinct

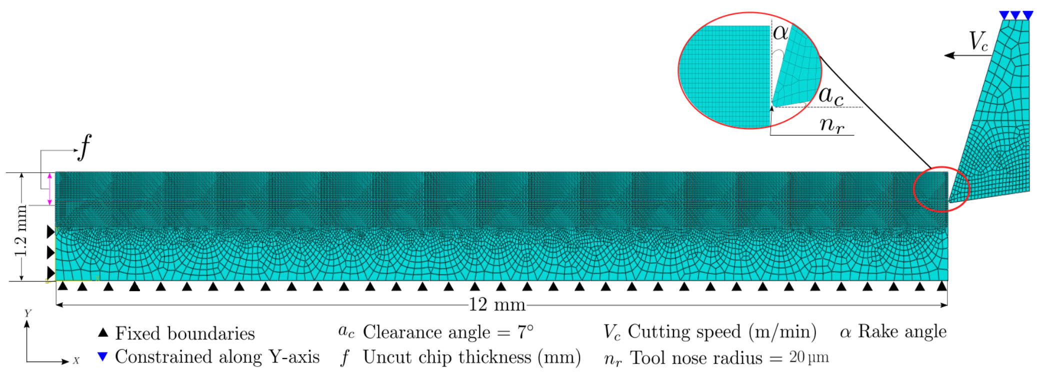

Figure 4.1: Finite element model setup [6].

regions, the slip region and the stick region. The slip region is characterized based on the model proposed by Yang and Liu [65] and the stick region is characterized based on the Zorev friction model [66].

For the chip separation, serration, and breakage, the Johnson-Cook damage model [67] was used. Based on the Johnson-Cook damage model, the overall damage in a material occurs in two steps, namely (1) damage initiation and (2) damage evolution. In a material, the damage initiates when/if the damage parameter exceeds or equals one. In ABAQUS [62], the damage evolution may be modeled either as exponential evolution or linear evolution. In this study, the damage evolution method is adopted from Patel & Cherukuri in [68]. The specific cutting force obtained from FEA simulations was compared to the available experimental results from the literature [69] with similar cutting parameters, similar material properties, and similar geometry to validate the model.

4.1.1.2 Finite Element simulations to generate data

The required data for the machine learning methods were generated using the FE model as explained in subsection 4.1.1.1 by changing the cutting parameters, namely the cutting speeds, the uncut chip thickness, and the rake angle. Here, seven cutting speed values, fthe uncut chip thickness values, and seven rake angles are considered as illustrated in Table 4.2. The different parameters resulted in 196 different simulations

Table 4.1: Material properties of the tool and the workpiece

Physical property	Tool (WC)	Workpiece (Al 2024-T351)
Density: ρ (Kg/m^3)	11900	2700
Young's Modulus: E (Gpa)	534	73
Poisson's ratio: ν	0.22	0.33
Specific heat: (J/Kg/°C)	400	C_p = 0.557 T+877.6
Thermal exp. coeff.: α_d (°C^{-1})	NA	$\alpha = (8.9e^{-3}$ T + 22.6$)e^{-6}$
Thermal conductivity: λ		for: 25 $\leq$ T < 300
(W/(m-°C))	50	λ = 0.247T + 114.4
		for: 300 $\leq$ T $\leq$ T$_{melt}$
	50	λ = 0.125T + 226

($7 \times 4 \times 7 = 196$). The clearance angle and the tool nose radius were kept constant in all simulations. The results were captured for every 1 μs. The total running time of all the simulations was 2352 hrs, indicating that on average, each simulation took around 12 hrs. The output parameters (the maximum tool temperature and the specific cutting force) were obtained in all the simulations.

The generated data set was used to train the proposed machine learning models as follows.

4.1.2 Machine Learning Background

Two machine learning models were considered and examined, namely Gaussian Processes Regression and Support Vector Regression models.

Table 4.2: Parameter choices used for the simulations.

Rake angle (deg)	Uncut chip thickness (mm)	Cutting speed (m/min)
-3.0	0.1	100
0.0	0.2	200
5.0	0.3	400
8.0	0.4	600
15.0		800
17.5		1000
20.0		1200

4.1.2.1 Support Vector Regression (SVR)

In SVR, the objective is to derive a hyperplane in the space that has the most ϵ deviation from all the actual target values for all training data records, while balancing the trade-off between the prediction error and the complexity. (ϵ is a hyperparameter in SVM loss function as illustrated in Figure 4.2.) A convex $\epsilon-$insensitive loss function is adopted as illustrated in Figure 4.2. As shown in the figure, a symmetric tube is defined around the estimated hyper-plane function. It is assumed that any absolute error less than a small pre-specified threshold ϵ is tolerated. Such small errors are ignored for the records above or below the estimated hyper-plane (function) for the purpose of reducing complexity [70]. Note that the One-dimensional form of the SVR is illustrated in Figure 4.3, where the geometrical perspective is easy to understand.

The SVR estimated function can be expressed as:

$$\begin{gathered} f(x) =< w, x > +b = \sum_{j=1}^{M} w_j x_j + b \\ f(x), b \in \mathbb{R} \\ x, w \in \mathbb{R}^M \end{gathered} \tag{4.1}$$

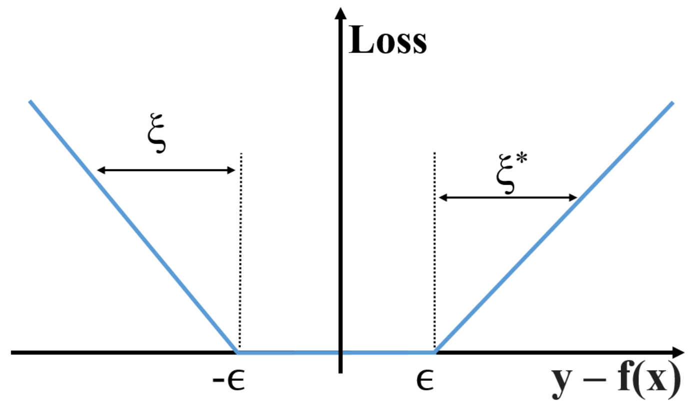

Figure 4.2: Linear $\epsilon-$insensitive loss function for SVR.

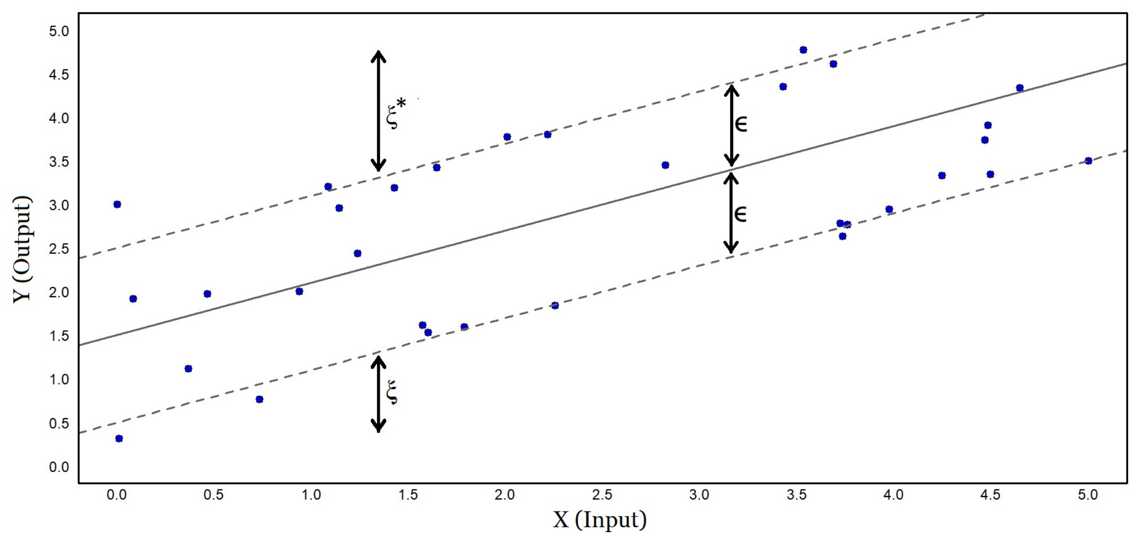

Figure 4.3: One-dimensional regression using SVR.

In the equation, M stands for the order of the polynomial used to construct the hyper-surface (function). The SVR algorithm tries to minimize the errors (for high accuracy) and simultaneously widen the tube centered around the function hyper-plane (to reduce the complexity and provide more stable predictions). Therefore, SVR tries to minimize the objective function as in the Equation 4.2:

$$\begin{gathered} objective\_function := \frac{1}{2}||w||^2 \\ \text{s.t.} \quad |f(x_i) - y_i| \leq \epsilon \end{gathered} \tag{4.2}$$

where y stands for the ground truth (target value). Here, the linear $\epsilon-$insensitive loss function tries to minimize the difference between the prediction using the model and the actual ground truth. Note that in SVR, one may adopt many different loss functions such as the linear function, the quadratic function, or Huber. [71].

In most cases in SVR, small errors are tolerated. However, deviations larger than ϵ are not to be ignored. Hence, nonnegative slack variables (ξ and ξ^*) are utilized in the objective errors [72]:

$$
\begin{aligned}
objective\_function &:= \frac{1}{2}||w||^2 + C\sum_{i=1}^{N} \xi + \xi^* \\
\text{s.t.} \quad y_i - f(x_i) &\leq \epsilon + \xi^*, \quad i = 1, \ldots, N \\
f(x_i) - y_i &\leq \epsilon + \xi, \quad i = 1, \ldots, N
\end{aligned}
\tag{4.3}
$$

In most real-case data sets, the records cannot be linearly separated by a simple hyperplane. To address the issue, a common technique called kernel trick is utilized. The goal of using the kernel trick is to handle nonlinearity in complicated data sets. The kernel function can map low-dimensional data to a high-dimensional space so that a linear separation will be possible. Usually, the Radial Basis Function (RBF) is considered the most commonly used kernel function for SVR, defined as:

$$k(x, x_i) = exp\{-\gamma||x - x_i||^2\}$$

where γ is called the RBF kernel hyperparameter and controls the impact of any single data record on all the other data points located far from it.

4.1.2.2 Gaussian Process Regression (GPR)

Gaussian Process Regression (GPR) is a statistical method designed for supervised learning. GPR proposes many probabilistic predictive functions to interpolate all the training records. Then the probabilistic functions are validated over the training records. Compared to many other supervised learning models, GPR is considered the method that can work with small training data. Moreover, the output of GPR can be the distribution of the predicted values, not only the final number. In practice, those distributions easily provide a confidence interval for each final prediction. GPR extends the common idea of considering a probability space over the numbers to a more sophisticated idea of defining the probability space over the functions. Usually, it is assumed that in a data set, the records are drawn from a distribution characterized by an average vector and a variance-covariance matrix. In GPR's sophisticated setting, one may look for a distribution over functions characterized by an average function and a variance-covariance matrix function. Having a training data sample and a family of the candidate functions, one may fit a distribution of the functions over them. To do that it is needed to choose/find the parameters of the distribution that justify or almost agree with the given function values. Finally, the Gaussian process is characterized by its average function and also its covariance function. For the Gaussian process regression, this covariance function will be characterized by the chosen kernel function which describes how strong is any single data record when impacting all other records. Note that this process can efficiently control how smooth the functions in the distribution will be[73, 74].

Assume that n data points are in the training data X. Also, suppose m points are given as the test data X^*. Moreover, assume the records are normalized. (They have zero-means.)

$$X =< x_1, x_2, \ldots, x_n >$$

$$X^* =< x_1^*, x_2^*, \ldots, x_m^* >$$

Suppose, the training labels and the test labels are:

$$Y =< y_1, y_2, \ldots, y_n >$$

$$Y^* =< y_1^*, y_2^*, \ldots, y_m^* >$$

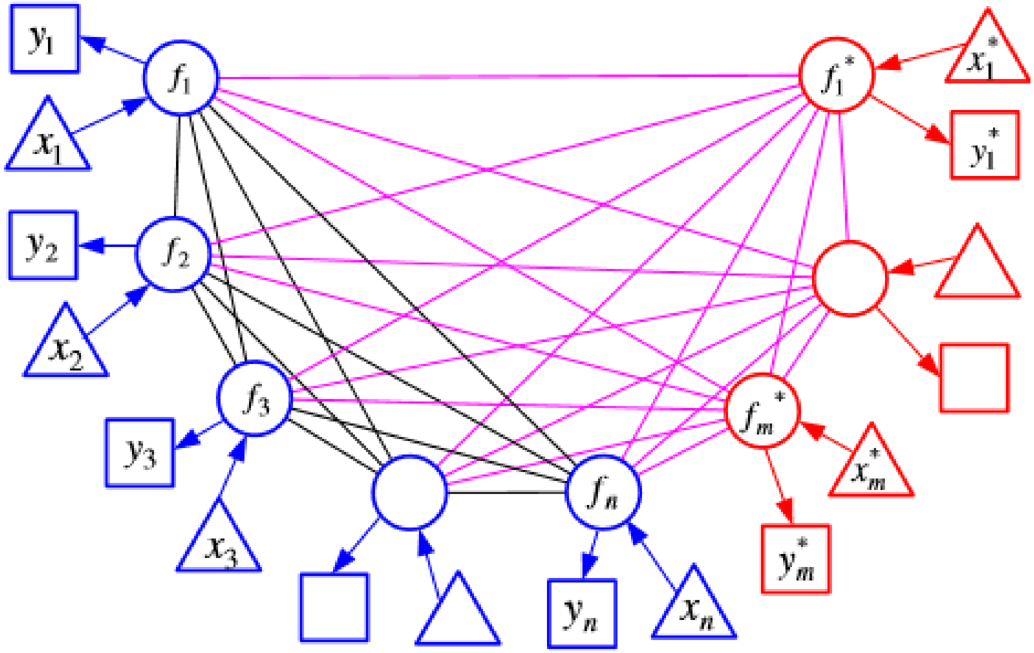

Figure 4.4: Graphical model of the GPR [7][8].

In Gaussian process regression, the core task is finding a set of latent functions $\mathcal{F} = \{f_1, f_2, \ldots, f_n\}$ whose joint distribution can match the data the best. Figure 4.4 illustrates this process in the Gaussian process model. As illustrated in figure 4.4, all of the latent functions are fully connected to each other by a covariance function that is characterized by their influence on each other. Every latent function f_i is here corresponding to a training record x_i. Also, note that having f_i and x_i will suffice for the prediction of y_i. Nonetheless, every f_i is here related to all the other latent functions, meaning that each f_i is also related to all the other values as well [7].

The Gaussian process is intended to be an approach for describing and then deriving the above-mentioned unknown latent functions. Even before observing the data points, a prior distribution is assigned over the functions. The prior distribution is updated when observing the data. The posterior distribution is calculated using the

Bayes theorem. In the Bayes theorem, it is assumed that the combination of data and prior distribution will provide the posterior. Having all the fitted distributions of the functions, one may predict the target y_i^* for any test data record x_i^*. Also, for each prediction, the empirical confidence interval is provided. This will give the upper band and the lower band, in addition to the final prediction.

Assuming a set of latent functions like $\mathcal{F} = \{f_1, f_2, \ldots, f_n\}$, their joint distribution can be defined as:

$$\mathcal{F}|x \sim \mathcal{N}(0, \mathcal{K})$$

where $\mathcal{N}$ stands for Normal (Gaussian) distribution. Usually, the mean in the prior is considered to be zero. Then, for the multivariate normal distribution, the covariance matrix $\mathcal{K}$ characterizes the relations among all the inputs. This symmetric covariance matrix may be computed under different assumptions. Note that the covariance matrix determines the distribution shape along with the predicting functions' characteristics. A popular way to calculate the covariance matrix is to utilize Radial Basis Function (RBF) [74] defined as:

$$\mathcal{K}_{i,j} = \mathcal{K}(x_i, x_j) = \sigma_f^2 \exp\{-\frac{1}{2l^2}(x_i - x_j)^2\}$$

where the amplitude σ_f and length scale l are the hyperparameters. When the length parameter is increased, the influence of the data records on each other is increased, even if they are far away. The kernel function assumes that the data records with close proximity are highly covariant, while the records at a far distance from each other are low covariant.

It is needed to link all the expected test labels Y^* to the train labels Y by assuming a joint distribution over them as:

$$\begin{bmatrix} Y \\ Y^* \end{bmatrix} \sim \mathcal{N}(0, \tilde{\mathcal{K}})$$

assuming

$$\tilde{\mathcal{K}} = \begin{bmatrix} \mathcal{K}(X,X) & \mathcal{K}(X,X^*) \\ \mathcal{K}(X^*,X) & \mathcal{K}(X^*,X^*) \end{bmatrix}$$

where the top-left $\mathcal{K}(X,X)$ is the covariance of the training data records, bottom-right $\mathcal{K}(X^*,X^*)$ is the covariance matrix of the test data points, and also $\mathcal{K}(X,X^*)$ represents the covariance matrix measuring the similarity between the train and the test data records. Note that the kernel function was previously defined for any pair of data points. But here, the kernel function $\mathcal{K}(\mathcal{P},\mathcal{Q})$ is defined on of any given two sets of data points $\mathcal{P} = \{p_1, p_2, \dots\}$ and $\mathcal{Q} = \{q_1, q_2, \dots\}$ as $\mathcal{K}(\mathcal{P},\mathcal{Q})_{i,j} = \mathcal{K}(p_i, q_j)$.

Now, the models are ready for predicting labels of the test data Y^* conditioned on the labels of the training data using the probability distribution:

$$Y^*|Y \sim \mathcal{N}(\mu, \Sigma)$$

where mean μ and covariance Σ are computed using the kernel function:

$$\mu = \mathcal{K}(X^*,X)\mathcal{K}(X,X)^{-1}Y$$

$$\Sigma = \mathcal{K}(X^*,X^*) - \mathcal{K}(X^*X)\mathcal{K}(X,X)^{-1}\mathcal{K}(X,X^*)$$

Note that here, to tune the hyperparameters l and σ_f used in kernel function $\mathcal{K}$, the log-marginal likelihood function $\log \mathbb{P}(Y|X)$ needs to be maximized.

$$\log \mathbb{P}(Y|X) \quad = \quad -\frac{1}{2}Y^T\mathcal{K}(X,X)^{-1}Y - \frac{1}{2}\log|\mathcal{K}(X,X)| - \frac{n}{2}\log 2\pi$$

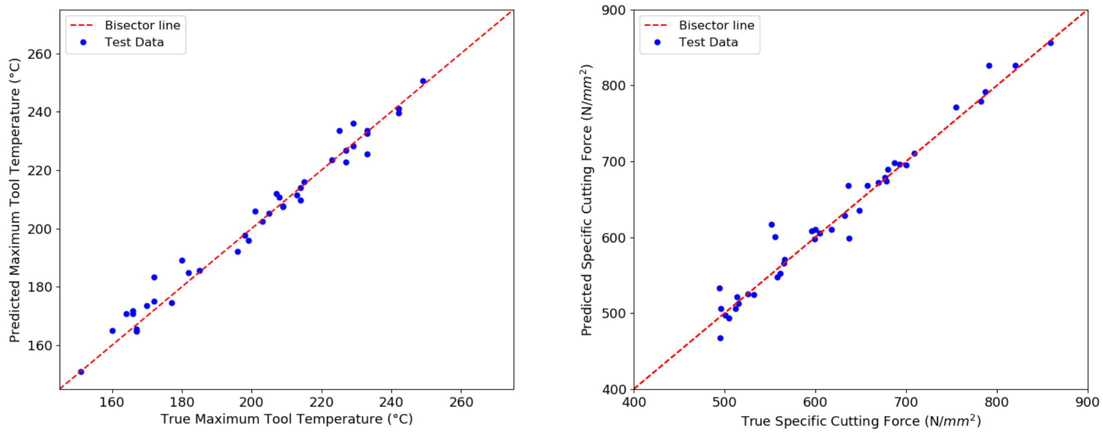

Figure 4.5: Relation between the ground truth and the SVR prediction for the maximum temperature (left) and the specific cutting force (right).

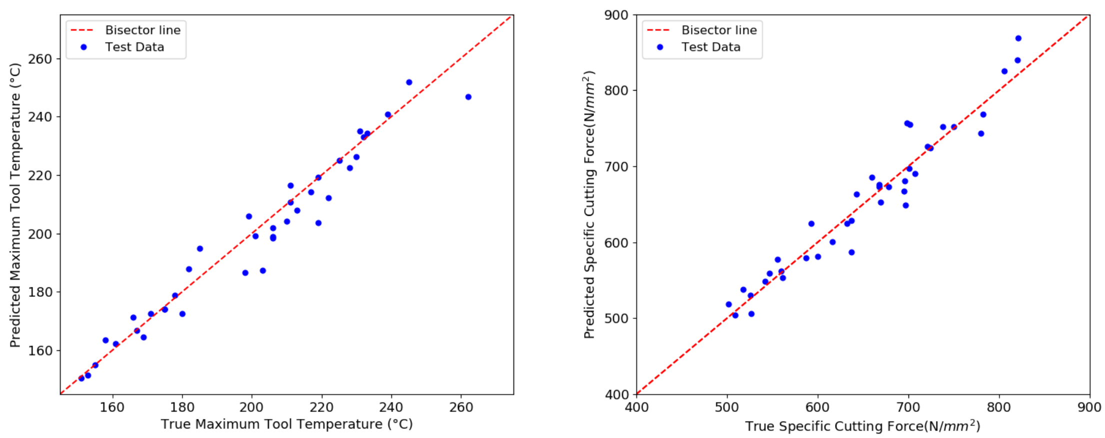

Figure 4.6: Relation between the ground truth and the GPR prediction for (a) the maximum tool temperature (left) and the specific cutting force (right).

4.1.3 Results & Discussion

4.1.3.1 Predicting the response using Support Vector Machine

To predict the maximum tool temperate and the cutting force, two different SVR models are utilized. In both cases, the input variables are cutting speed (V_c), the uncut chip thickness (f), and the rake angle (α). The inputs are normalized to be in the 0-1 range before hyperparameter tuning. The Scikit-learn package in Python is used to develop the SVR models. The data set consisted of 196 observations split into

80% training and 20% testing. The linear ϵ–insensitive as the loss function was used for the model. Also, the regularization parameter C, ϵ, and RBF kernel parameter γ were tuned via grid search for this study. Moreover, cross-validation was used considering 10 folds to minimize the mean square error (MSE) and maximize the coefficient of determination (R^2):

$$MSE = \frac{1}{n}\sum_{i=1}^{n}(y_i - y_i^p)^2 \tag{4.4}$$

$$R^2 = 1 - \frac{\sum_{i=1}^{n}(y_i - y_i^p)^2}{\sum_{i=1}^{n}(y_i - \bar{y})^2} \tag{4.5}$$

Here, y_i, $\bar{y}$, and y_i^p represent the ground truth, mean ground truth, and the prediction, respectively. The goal of SVR here is to achieve the model with the largest R^2 and the smallest value of MSE. To predict maximum temperature, the hyperparameters $\epsilon = 0.001$, $C = 20$, and $\gamma = 0.4$ were found to achieve the best performance. The R^2 and the MSE for this model are mentioned in Table 4.3. The model resulted in values 0.0012 and 0.0015 of MSE for the test and train data, respectively. The negligible values of MSE are confirming that the SVR model predictions are highly accurate. Comparing the MSE values on test and train data shows that the model is performing well since it is observed that the MSE on test data is less than that of the training data, meaning that the model did not overfit.

Similarly, the grid search was done to optimize the hyperparameters for the SVR model that was designed to predict the specific cutting force. It was observed that the hyperparameters $C = 15$, $\epsilon = 0.001$, $\gamma = 0.4$ will let us achieve the best model. Table 4.4 shows the R^2 and MSE results for the SVR model. As observed in the table, the MSE on both test and train data is fairly small. Also, the MSE on the test data is smaller than that of the train data. This is confirming that the model did not overfit. Also, the R^2 on both test and train data is close to 1, meaning that the model has learned the data well.

Table 4.3: The results from SVR predicting the maximum tool temperature.

	$\mathbf{R}^2$	**MSE**
Train Data	0.9680	0.0015
Test Data	0.9748	0.0012

Table 4.4: The results from SVR predicting the specific cutting force.

	$\mathbf{R}^2$	**MSE**
Train Data	0.9400	0.0029
Test Data	0.9635	0.0014

Figure 4.5 illustrates the relation between the ground truth and predictions for the specific cutting force and also the maximum tool temperature using the SVR model. As the figure suggests, for the test data dots are very close to the plot bisector line, meaning that the predictions are very close to the ground truth.

4.1.3.2 Predicting the response using Gaussian process regression

Here, two GPR models were developed to predict the specific cutting force and the maximum tool temperature. The objective here is to maximize the R^2 and minimize the MSE. Again the cross-validation was utilized using 10 folds.

First, the hyperparameter tuning was performed to optimize l and σ_f for the model predicting the maximum tool temperature. Before hyperparameter tuning, the data was normalized to be in the range of 0-1. Similar to the SVR models, the data was split into 20% for testing and 80% for training. In hyperparameter tuning, while maximizing the log marginal likelihood on the train data, it was found that the best model will be achieved using $l = 0.21$ and $\sigma_f = 0.324$. Table 4.5 contains the results applying GPR model on test and train data records. As Table 4.5 suggests, the MSE on the train data is zero. This is justified by the fact that the data is noise free. Hence, the prediction distribution function can exactly fit data records, so the predictions on train data will be exactly equal to the ground truth. As shown in the table, the MSE on the test data is around 0.0027 confirming that the GPR model is performing well on the data set.

A similar procedure was also applied for the prediction of the specific cutting force using a GPR model. the results from hyperparameter tuning on train data showed that $l = 0.196$ and $\sigma_f = 0.287$ will lead us to the best model setting. The GPR model performance results (R^2 and MSE) are shown in Table 4.6. Here, the MSE is zero on the train data, and 0.0021 on the test data. Note that the R^2 values are fairly close to one, in both GPR models. Thus, one may conclude that the GPR models are accurately predicting the maximum tool temperature and the specific cutting force. Also, Figure 4.6 provides the visual interpretation of the GPR models. In the figure, for both models, the predictions are plotted against the ground truth. In such a figure, having most dots close to the bisector means that the models are performing well in terms of accuracy.

Table 4.5: The results from GPR predicting the maximum tool temperature

	$\mathbf{R}^2$	**MSE**
Train Data	1.0000	0.0000
Test Data	0.9533	0.0027

Table 4.6: The results from GPR predicting the specific cutting force.

	$\mathbf{R}^2$	**MSE**
Train Data	1.0000	0.0000
Test Data	0.9423	0.0021

To conclude this section, two machine learning models were examined to predict the maximum tool temperature and the specific cutting force during orthogonal machining. Here, Gaussian Processes Regression and Support Vector Regression were utilized. To examine the machine learning methods, the data simulated with the finite element method using ABAQUS/EXPLICIT were utilized. In the results, it was observed that the SVR outperforms the GPR in the prediction of both the specific cutting force and the maximum tool temperature. Still, the GPR results (MSE and R^2) are fairly close to the corresponding results from SVR for both prediction purposes.

From "No Free Lunch Theorem" [75], it is known that before testing different models e.g. SVM and GPR, it is not possible to certainly determine which one will outperform the other models. Also, once different models are tried, trying to justify the best model, would be more rationalizing than effective interpretation. Thus, without any intention to provide reasoning, this study concludes that SVR slightly outperformed GPR, but both provided reasonably good predictions.

4.2 The Inverse Problem of Stability Lobe Diagram

While there are some conventional methods to construct analytical stability lobe diagrams given the structural parameters, here the research problem is to do the "inverse problem". The goal of this research is to examine the possibility of deriving those structural dynamics variables out of the in-process stability lobe diagram. Here, a multivariate Newton method approach is used and through the algorithm, physics-based and in-process stability lob diagrams are compared to each other in each iteration. A pre-defined objective function measuring the disturbance is calculated and updated in each iteration so the success of the algorithm in providing acceptable guesses for the structural parameters is quantified at the end of each iteration. Thresholding such an objective, the algorithm may stop when the updated guessed parameter set is optimized to justify the empirical stability lobe. The details of the algorithm are explained in Section 4.2.1.

4.2.1 A Brief Sketch of Multivariate Newton Approach

The stability lobe diagram in general is a real-valued function of structural dynamics and cutting parameters. Fixing the cutting parameters, one may assume only the structural parameters are determinants of the stability lobe. The goal of this research is to examine the possibility of deriving the structural dynamics variables, given the empirical stability lobe diagram. Assuming that SLD^{exp} denotes the experimental SLD which is given based on the data points collected during the milling operation. So the target here is to extract the structural dynamics parameters out of SLD^{exp} using a multivariate Newton method. It is assumed that the SLD^{exp} is comprised of n data points (n pairs of (Ω, b)):

$$\Omega^{exp} = \{\Omega_1^{exp}, \cdots, \Omega_n^{exp}\}$$

$$b^{exp} = \{b_1^{exp}, \cdots, b_n^{exp}\}$$

where Ω is spindle speed and b is depth of cut. Having m structural dynamics parameters, the SLD^{exp} is assumed to be a function of those m parameters. Those parameters are the unknowns of the problem and are to be found through the inverse approach.

$$SLD^{exp} = SLD^{exp}(p_1, p_2, \cdots, p_m)$$

The approach is summarized as follows:

STEP 1. To calculate unknown parameters, a multivariate Newton method is used, which starts with an initial guess for the variables. Then, the analytical stability diagram can be generated based on the Fourier series approach.

$$initial\_guess = (p_1^*, \cdots, p_m^*)$$

$$SLD^* = SLD(p_1^*, \cdots, p_m^*)$$

Hence, there are two stability boundaries, the given one called empirical SLD (SLD^{exp}), and the one built upon the physics-based model based on some initial guess (SLD^*). Then, for the same values of spindle speed in the experimental data set, the values of depth of cut are calculated according to SLD^*:

$$b^* = \{SLD^*(\Omega_1^{exp}), \cdots, SLD^*(\Omega_n^{exp})\}$$

STEP 2. After building the analytical SLD based on the initial guess (SLD^*), the guess needs to be evaluated by being compared with the reference stability lobe diagram (SLD^{exp}). Here, Mean squared error is used as the objective function.

$$MSE = MSE(p_1^*, \cdots, p_m^*) = \frac{\Sigma_{i=1}^{n}(b_i^{exp} - b_i^*)^2}{n}$$

STEP 3. Here, the sensitivity of the objective function with respect to each parameter

p_i^* is calculated. For this purpose, the partial derivative of the objective function with respect to each parameter is calculated numerically as follows:

1. Generate $SLD_i^* = SLD(p_1^*, \cdots, p_i^* + \epsilon, p_m^*) \quad ; \quad i = 1, 2, \cdots, m$
2. Generate $MSE_i = MSE(p_1^*, \cdots, p_i^* + \epsilon, p_m^*) \quad ; \quad i = 1, 2, \cdots, m$
3. Get the sensitivity of MSE to p_i^*:

$$S_i = \frac{\partial MSE}{\partial p_i^*} = \frac{MSE_i - MSE}{\epsilon}$$

STEP 4. The last step in the method is to update the values for each unknown parameter based on the objective function and its sensitivity calculated in the previous step:

$$p_i^* \leftarrow p_i^* - \frac{MSE \times S_i}{||S||^2} \times \alpha \quad ; \quad i = 1, 2, \cdots, m.$$

Here, α controls the pace ($\alpha \in (0, 1]$). It is assumed that $\alpha = 1$ for simplicity in this work.

Through the repetitive algorithm, physics-based and given empirical stability lobe diagrams are compared to each other in each iteration. To evaluate the parameters, a pre-defined objective function measuring the disturbance is calculated and updated in each iteration, so the success of the algorithm in providing acceptable guesses for the parameters is quantified at the end of each iteration. Hence, by repeating this algorithm several times and using the updated parameters each time, the method would converge to the right answer for unknown parameters. Thresholding such an objective, the algorithm may stop when the parameter set is optimized enough to justify the empirical stability lobe diagram.

4.2.2 Adjustments & Improvements

Using the multivariate Newton method, one may face some challenges to facilitate the algorithm convergence.

1. The first possible improvement is to find a proper objective function that can evaluate the results effectively. The convergence of the algorithm is extremely sensitive to the choice of the objective function, especially when dealing with the multivariate function.

   In some cases for example, it is observed that replacing MSE (Eq. 4.6) with mean log absolute error (Eq. 4.7) would be helpful since the log is a concave function and is less sensitive to big changes comparing the quadratic function.

$$MSE = MSE(p_1^*, \cdots, p_m^*) = \frac{1}{n}\Sigma_{i=1}^n (b_i^{exp} - b_i^*)^2 \tag{4.6}$$

$$\begin{aligned} Objective\_function &= Obj\_func(p_1^*, \cdots, p_m^*) \\ &= \frac{1}{n}\Sigma_{i=1}^n \log(1 + |b_i^{exp} - b_i^*|) \end{aligned} \tag{4.7}$$

2. The other issue in the Newton method is getting stuck in the local minima. So to overcome this issue, one may add some random jumps, to have a chance of passing the local minima. For example, if in 10 consequent steps, the algorithm did not make good progress, one may add some e.g. 1% or 5% jumps in each/some parameters if it improves the results.

   The jumps may be set to occur after every few steps of the Newton method. Alternatively, the jumps may be set not to occur unless the algorithm is not making good progress during the consecutive steps. For, instance if the algorithm cannot decrease the value of the objective function by a certain threshold during a certain number of consecutive steps, one may assume it is stuck in a local minimum and a jump should follow the Newton steps.

3. Also, looking at the progress of the approach in each step, it seems that sometimes the algorithm failed at the critical points on the Stability boundary. So,

the algorithm will be improved if it is made more sensitive to the evaluation of the critical points. An example of SLD along with the critical points is illustrated in Figure 4.7.

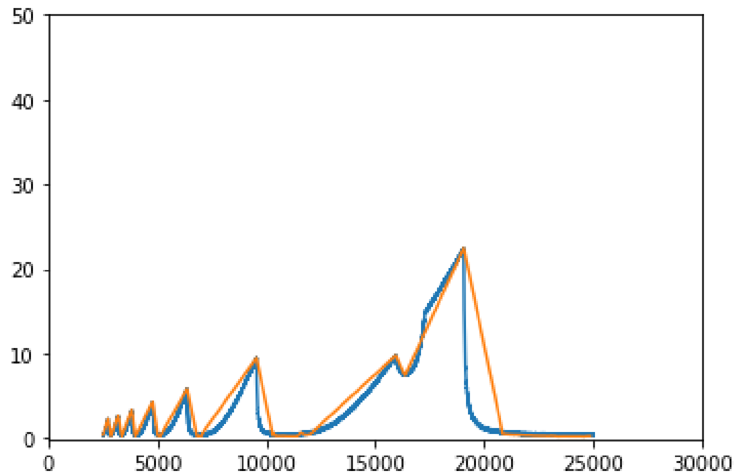

Figure 4.7: Capturing the critical points.

Let C be the set of the critical points on the SLD.

$$C = \{c_1, \cdots, c_l\} \tag{4.8}$$

with

$$c_j = (\omega_j, b_j), \quad j = 1, \cdots, l. \tag{4.9}$$

Then, Eq. 4.7 can be modified to make the objective function more sensitive to the error terms on the critical points:

$$\begin{aligned} Objective\_function = & \frac{1}{n}\Sigma_{i=1}^{n} \log(1 + |b_i^{exp} - b_i^*|) \\ & + \frac{\beta}{l}\Sigma_{j=1}^{l} \log(1 + |b_j^{exp} - b_j^*|) \end{aligned} \tag{4.10}$$

The parameter β in Eq. 4.10 controls the sensitivity of the objective function to the error terms on the critical points. Setting $\beta = 0$ will remove the proposed modification while using a large β makes the algorithm to focus on the critical points and mostly ignore the other points.

4. Since the behavior of the SLD function is not linear with respect to the different parameters, the convergence of the algorithm highly depends on the chosen initial guess. While the algorithm may converge fast using a good initial guess, it may take much longer, or even fail to converge, if another initial guess is utilized. In practice, to overcome the abovementioned issue, one may use different initial guesses and attack the problem from a diverse set of initial guesses.

Note that in this synthetic example, the data set covered around 1000 pairs of the depth of cut and spindle speed. In contrast, there were only 6 unknown parameters found through the Newton method approach. A large number of observations vs. a small number of parameters (inputs of the SLD function) implies that overfitting will not be a serious issue when finding the parameters.

4.2.3 Results & Discussion on Synthetic Data

Here the inverse method is evaluated using synthetic data sets and the results are discussed. Note that the results and discussion on empirical data are discussed in section 4.2.4.

In this example, synthetic data is used. That is, having the structural dynamics parameters and cutting parameters, listed in Table 4.7, the target SLD is generated. Then, it is assumed that structural dynamics parameters are unknown, and are to be found through the inverse method. The cutting parameters are fixed and do not get updated through the iterations.

Table 4.7: Cutting parameters and structural dynamics parameters used to generate synthetic data.

Parameter	Value
Number of flutes: N_t	3
Exit angle: ϕ_e (deg)	180
Start angle: ϕ_s (deg)	126.87
Tang. force coef. k_t (MPa)	2173.3
Normal force coef. k_n	0.267
Natural freq. f_{nx} (Hz)	900
Stiffness: k_x (MN/m)	9
Damping ratio: ξ_x	0.02
Natural freq. f_{ny} (Hz)	950
Stiffness: k_y (MN/m)	10
Damping ratio: ξ_y	0.01

The blue SLD in Figure 4.8 is the target SLD, and the orange SLD is the guessed SLD which is being updated in each iteration. Some of the iterations of the Newton method are visualized in Figure 4.8 to illustrate how gradually the guessed SLD gets close to the target SLD. As shown in the figure, the guessed parameters improve through iterations and the algorithm converges and finds the parameters that can build the given SLD. The predicted values in Table 4.8, are the calculated structural dynamics parameters in step 74. The identified parameters in the last step can be used as the answer to our problem statement, as the calculated error is small enough. In practice, a pre-specified threshold may be used, e.g. 0.1% of the depth of cut (b) range (max - min) in the empirical SLD.

Table 4.8: In-process Structural dynamics parameters calculated using the inverse method for synthetic data.

Parameter	Target Value	Predicted Value
Natural frequency: f_{nx} (Hz)	900.0	895.3
Stiffness: k_x (MN/m)	9.0	9.2019
Damping ratio: ξ_x	0.0200	0.0211
Natural frequency: f_{ny} (Hz)	950.0	947.6
Stiffness: k_y (MN/m)	10.0	9.9809
Damping ratio: ξ_y	0.0100	0.0105

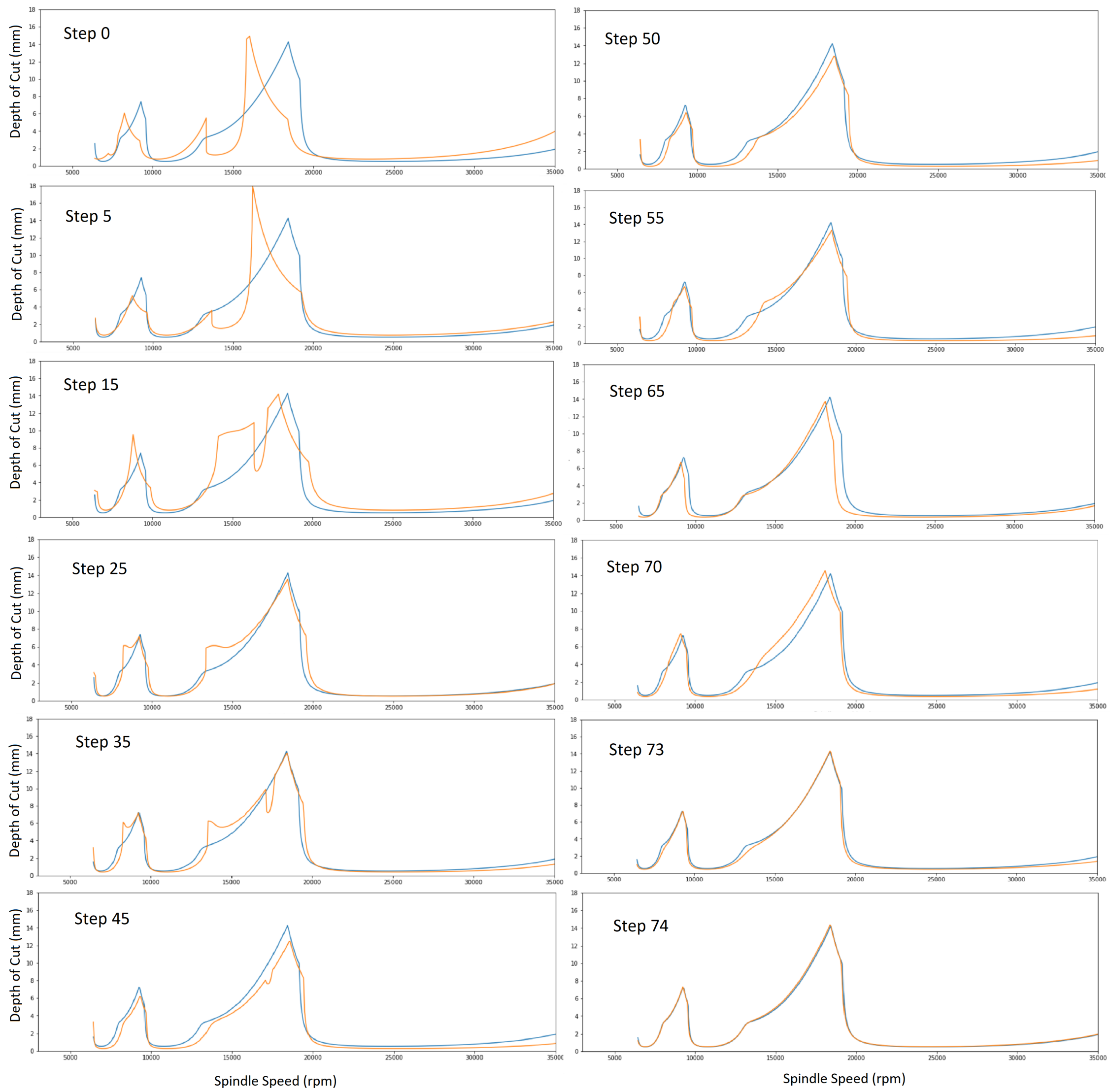

Figure 4.8: Results Using Newton method on synthetic data. The blue curve is the target SLD, while the orange curve represents the guessed SLD at each step.

4.2.4 Results & Discussion on Experimental Data

The inverse method is examined in chatter tests with a three-flute carbide (ZrN) end mill and also another two-flute carbide end mill tool. Also, a data set with a four-flute tungsten end mill reported by Eynian [1] is investigated, and the results are evaluated.

4.2.4.1 Slot milling using a four-flute end mill

To evaluate the Newton method, also an experimental data set presented in [1, 2] was utilized. This experiment was performed with a four-flute tungsten carbide end mill. The workpiece is a plate made of aluminum 7075-T651. The data set contains 21 chatter tests of slot milling on the boundary at spindle speed between 5500 and 6500 rpm, which are illustrated by red points in Figure 4.9. That is, any point below these points is recognized as stable and any point above them is recognized as chatter. The tangential cutting force, calculated in static conditions is 1110 MPa, and the radial cutting force coefficient is 0.22. The modal parameters measured by applying the impact test in the static state of the machine are reported in Table 4.9, where x and y are feed and cross-feed directions, respectively. Stability lobes in zero spindle speed are generated using the information in Table 4.9. This boundary is shown by the black dashed curve in Figure 4.9, which predicts many chatter cuts as stable incorrectly. To capture the in-process structural dynamics parameters, the Newton-Raphson method was applied to the experimental data set. These experimental records are considered as the target SLD. However, there are fewer data points making the boundary comparing the target SLD in synthetic examples. Table 4.10 shows the results derived from the Newton-Raphson method. In this case, it is assumed that the tool-spindle assembly is asymmetric, so the structural dynamics parameters have equal properties in the feed and cross-feed directions. The stability boundary generated using these values is shown in Figure 4.9 with the blue

Table 4.9: Structural dynamics parameters in zero spindle speed for the four-flute tool as reported in [1].

Parameter	Mode.1	Mode.2
Natural frequency: f_{nx} (Hz)	3890.0	4182.0
Stiffness: k_x (MN/m)	22.60	15.40
Damping ratio: ξ_x	0.0196	0.0170
Natural frequency: f_{ny} (Hz)	3872.0	4127.0
Stiffness: k_y (MN/m)	23.40	25.10
Damping ratio: ξ_y	0.0220	0.0177

solid curve. The natural frequency value decreases notably to 4103.4 Hz compared to the results of the impact test (4182 Hz). Thus, the experimental chatter records are shifted to the left-hand side of the stability lobe diagram on stationary speed. The stiffness value reaches 11.65 MN/m which is considerably less than the results of the impact test (15.40 MN/m) while the damping ratio increases from 0.0170 in stationary condition to 0.0269. Table 4.10 also includes the results from two methods used in [1] (Method 1: Two-point Method, Method 2: Regression Method). As the table suggests, the results are almost consistent with the results extracted from these two methods, but as Figure 4.9 shows, the SLD generated based on the results of the Newton-Raphson method covers more chatter records. As mentioned in Table 4.10, the error measured in terms of MSE for the Newton-Raphson method is around 3 times lower than the error from Method 1, and around 20% lower than Method 2. This will be discussed further in Section 4.3.

Table 4.10: In-process structural dynamics parameters calculated using Newton-Raphson method and the methods used in [1].

Parameter	Newton-Raphson	Method.1	Method.2
Natural frequency: f_n (Hz)	4103.4	4124	4103
Stiffness: k (MN/m)	11.65	10.63	8.90
Damping ratio: ξ	0.0269	0.0307	0.0379
Final MSE	0.000459	0.001406	0.000574

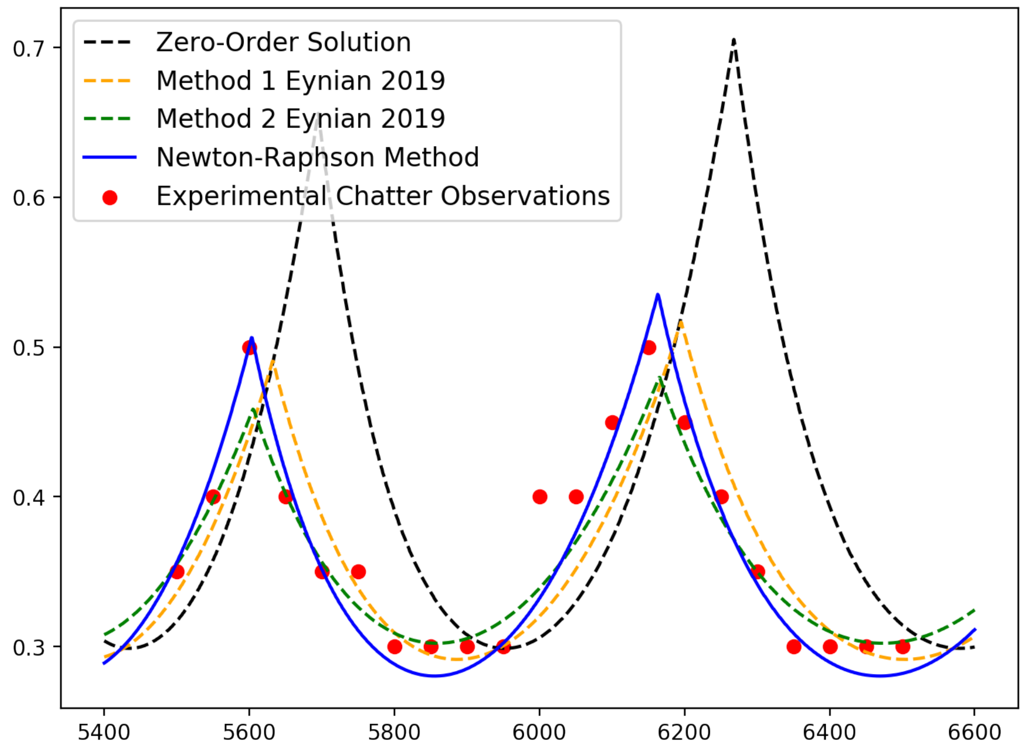

Figure 4.9: Stability lobe diagram on empirical data for Newton-Raphson method and methods used in [1].

4.2.4.2 Slot milling using a three-flute end mill

The second set of experimental data [76] considered in this work consists of full-engagement milling of aluminum 7075 plates with a three-flute carbide (ZrN-coated) end mill. The tool has 0.5 in diameter with a flute helix angle of 30°. The tool was mounted with a 2.4 in stick-out. The tool dynamics flexibility is calculated by performing an impact hammer test on the tip of the tool. The frequency response function in X (feed direction) and Y (cross-feed direction) directions are shown in Figure 4.10.

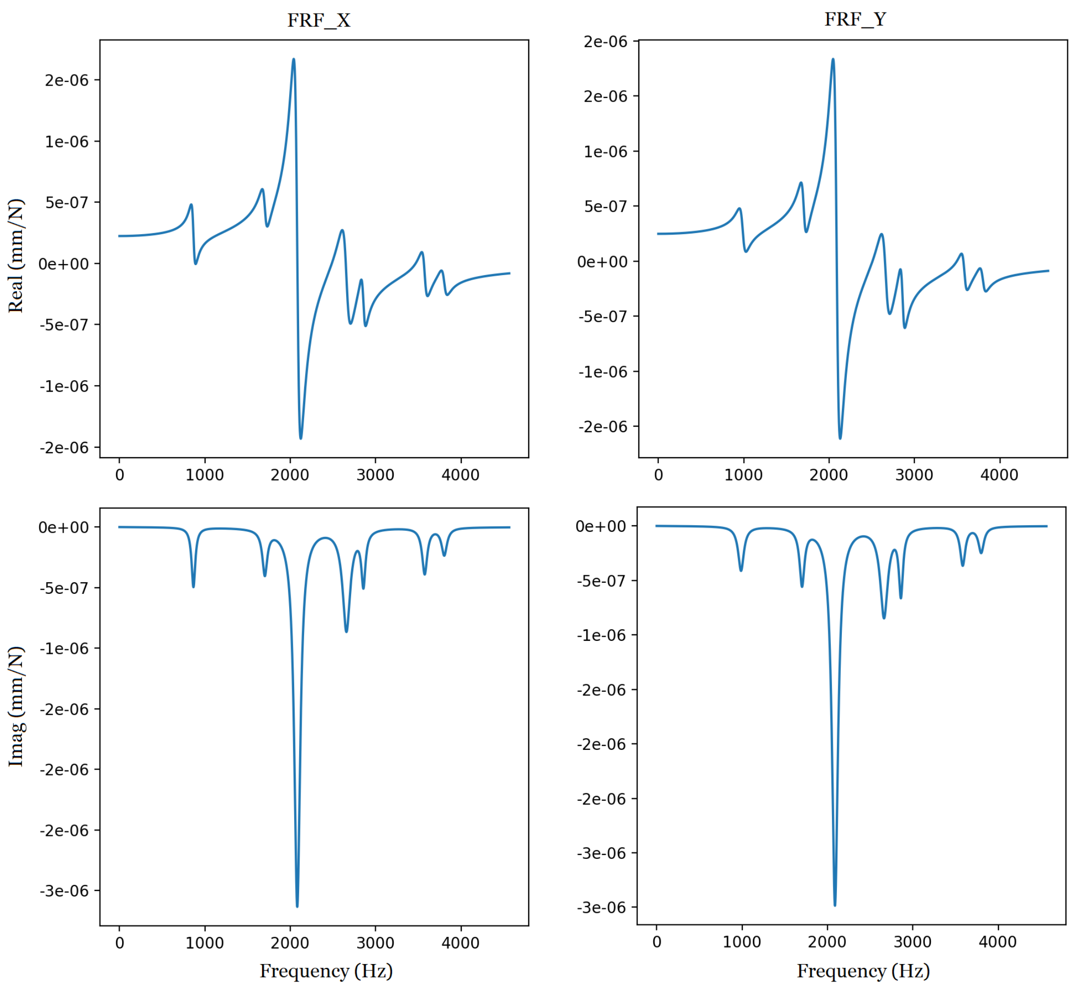

Figure 4.10: Real and Imaginary parts of dynamic flexibility of the 3-flute tool in X and Y directions.

Table 4.11: Modal parameters for the 3-flute end mill at the stationary spindle.

	Feed (X)			Cross-Feed (Y)		
	f_n (Hz)	k (MN/m)	ξ	f_n (Hz)	k (N/m)	ξ
Mode#1	866.93	33.881	0.03	989.04	30.761	0.04
Mode#2	1702.94	68.463	0.02	1702.94	48.481	0.02
Mode#3	2082.79	8.005	0.02	2088.96	7.197	0.02
Mode#4	2658.86	29.770	0.02	2663.40	30.604	0.02
Mode#5	2857.40	113.048	0.01	2860.84	83.683	0.01
Mode#6	3575.20	131.662	0.01	3584.82	141.736	0.01
Mode#7	3804.29	223.404	0.01	3801.07	211.882	0.01

Modal parameters extracted from these tests are listed in Table 4.11. The cutting force coefficients are measured by conducting some experiments in the stable region. The radial and tangential are 0.176 and 787.8 MPa, respectively.

Three different data sets are collected during the cutting tests. For each data set spindle speed increases from 6000 rpm to 12000 rpm by a step size of 100, and the depth of cut increases from 0.2 mm to 1.6 mm with the step size of 0.1. Data set 1 includes 305 data points and data sets 2 and 3 include 278 data points each. The data points are labeled and classified as chatter and stable points for each data set that are shown in Figure 4.11. The values of chatter frequency for the chatter observations on the boundary (chatter point with the minimum depth of cut at each spindle speed value) show that mode 3 in Table 4.11 is the dominant mode and results in chattering in this case. Therefore, only this mode was used in the calculations to generate the stability lobe diagram. Figure 4.11 obviously shows that the stability lobe diagram generated based on the modal parameter measured in static conditions can not justify the experimental observations. It is also observed that some points that are labeled as stable in one data set have turned to chatter, and vice versa. In the study, the inverse approach was used for each data set separately. The identified values for modal parameters for each data set are presented in Table 4.12.

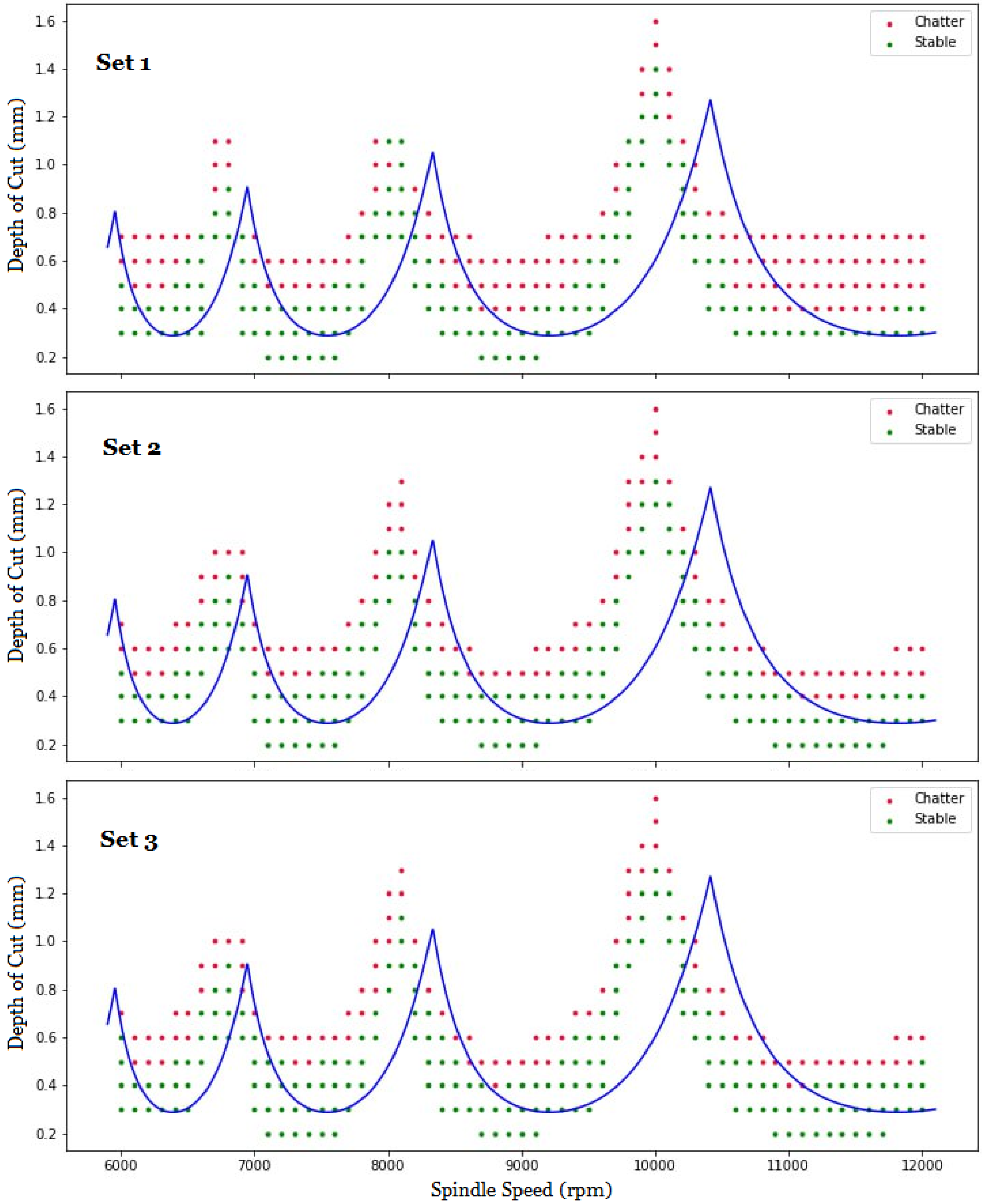

Figure 4.11: Experimental results with 3-flute end mill for three data sets and stability lobe diagrams from impact test on the stationary spindle using zero-order solution.

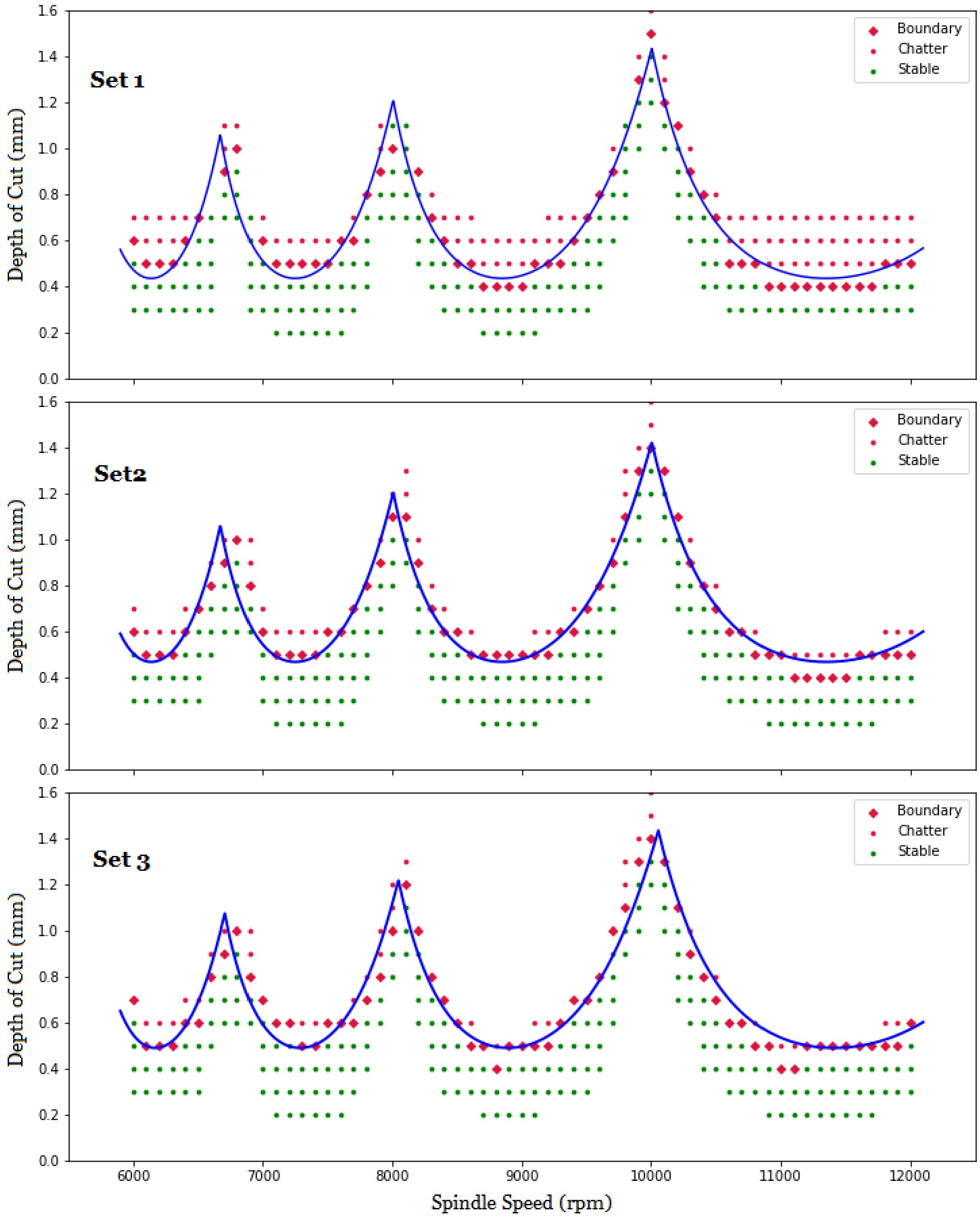

Figure 4.12: Stability lobe diagrams from Newton-Raphson methods on three experimental data sets with 3-flute end mill in the spindle speed range 6000-12000 rpm.

The stability lobe diagrams generated using the in-process modal parameters in

Table 4.12 are illustrated in Figure 4.12 for each data set. This figure shows that the in-process stability lobe diagrams are located on the right-side of the stability lobe diagrams in Figure 4.11 in which the modal parameters in static conditions are used. This happens because of the reduction in natural frequency in dynamic conditions. Comparing the results from Table 4.11 with Table 4.12, it can be seen that stiffness and damping ratio increase during cutting operations.

Table 4.12: In-process Structural dynamics parameters calculated using the inverse method for 3-flute end mill for three sets of experimental data in the spindle speed range of 6000-12000 rpm.

	Set.1	Set.2	Set.3
Natural frequency: f_n (Hz)	2000.7	2000.8	2010.9
Stiffness: k (MN/m)	8.4559	8.1668	8.1256
Damping ratio: ξ	0.030524	0.034030	0.035857

The stability lobe diagrams derived from the inverse approach in Figure 4.12 show that some chatter points are still located in stable regions in some data sets, especially in data set 2 and 3. For example in data set 3, some points with spindle speed in the range of 6500 to 6700 rpm, 7700 to 8000 rpm, and 10200 to 11100 rpm are classified under the stability boundary while they need to be in chatter region. As it is known that the stability lobe diagram generated using the zero-order solution, always has a constant minimum depth of cut for all the lobes. But The experimental results in Figure 4.11 show a different depth of cut for each lobe. To overcome this issue and also calculate more accurate structural dynamic parameters, the spindle speed range was divided into two ranges of 6000-8000 rpm and 8000-12000 rpm and applied the inverse approach to each of these speed ranges separately. The modal parameters derived using the Newton-Raphson method for the speed range of 6000-8000 rpm for three data sets are listed in Table 4.13. The stability lobe diagrams generated based on the results from this table are presented in Figure 4.13. It should be noted that although the stability lobe diagram is plotted for the speed range of 6000-12000 rpm, only the data point in the speed range of 6000-8000 rpm is used as the input of the Newton-Raphson method algorithm for each data set. Table 4.13 shows that the natural frequency increases notably in comparison with the results reported in Table 4.12. As a result, the stability lobe diagrams shifted to the right in Figure4.13. The values of stiffness and damping ratio increase slightly except for the stiffness in data set 3.

Table 4.13: In-process Structural dynamics parameters calculated using the inverse method for 3-flute end mill for three sets of experimental data in the spindle speed range of 6000-8000 rpm.

	Set.1	Set.2	Set.3
Natural frequency: f_n (Hz)	2020.8	2020.8	2030.7
Stiffness: k (MN/m)	8.6261	8.3147	8.0848
Damping ratio: ξ	0.033963	0.036014	0.036548

The results of the inverse approach for the spindle speed range of 8000-12000 rpm for each data set are reported in Table 4.14. The stability lobe diagrams calculated using the results from this Table are plotted in Figure 4.14. It should be noted that although the stability lobe diagram is plotted for the speed range of 6000-12000 rpm, only the data point in the speed range of 8000-12000 rpm is used as the input of the Newton-Raphson method algorithm for each data set. Table 4.14 shows that the natural frequency is the same as the results listed in Table 4.12 except for the data set 3 which shows a reduction in natural frequency. As a result of such reduction, the stability lobe diagram shits to left, as shown in Figure 4.14.

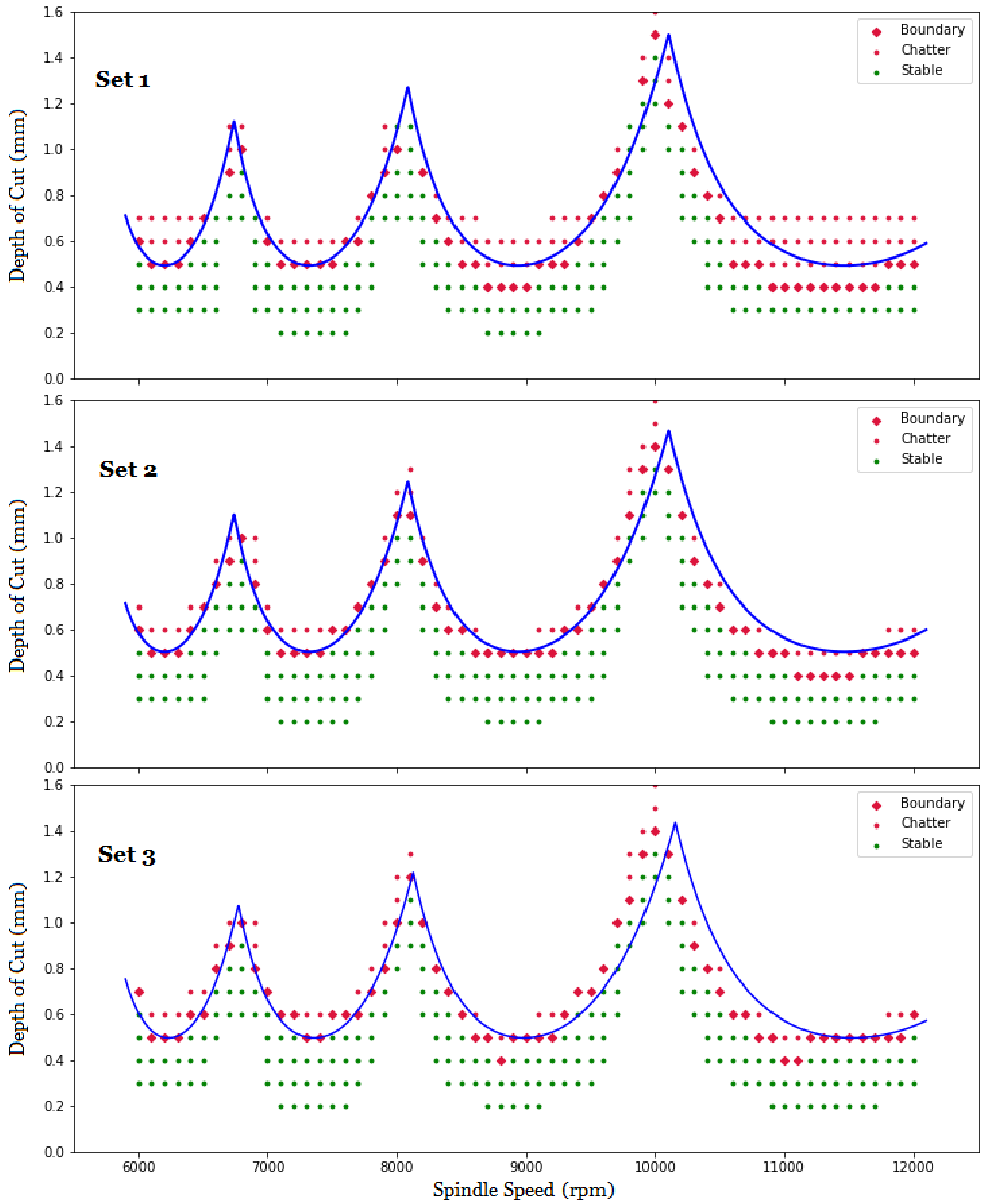

Figure 4.13: Stability lobe diagrams from Newton-Raphson methods on three experimental data sets with 3-flute end mill in the spindle speed range 6000-8000 rpm.

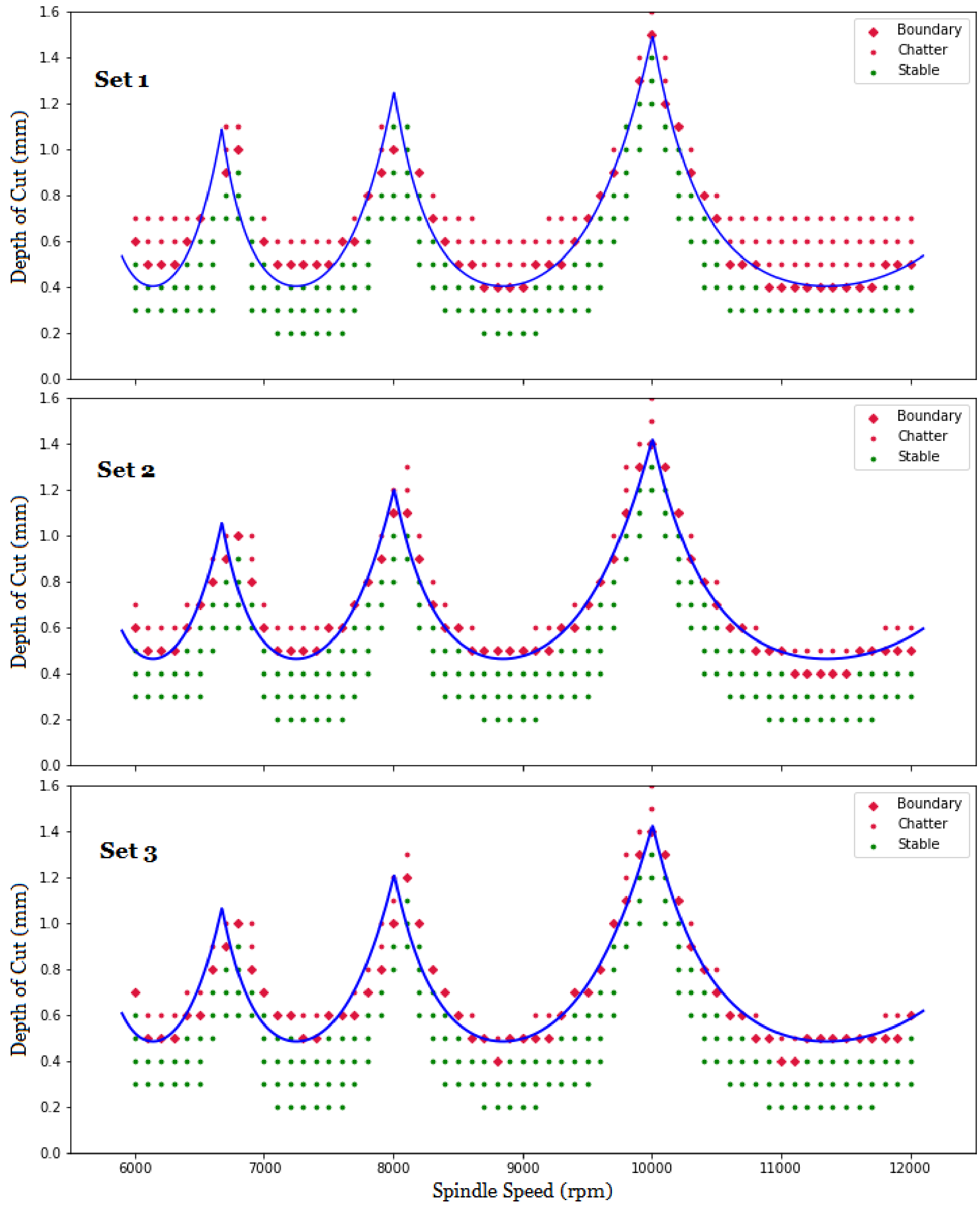

Figure 4.14: Stability lobe diagrams from Newton-Raphson methods on three experimental data sets with 3-flute end mill in the spindle speed range 8000-12000 rpm.

The results for the data set 1 in Table 4.14 show that the stiffness increases while the damping ratio decrease in comparison with the values reported in Table 4.12. It is also observed that the calculated natural frequency values in the speed range of 8000-12000 rpm for each data set are approximately the same.

Table 4.14: In-process Structural dynamics parameters calculated using the inverse method for 3-flute end mill for three sets of experimental data in the spindle speed range of 8000-12000 rpm.

	Set.1	Set.2	Set.3
Natural frequency: f_n (Hz)	2000.7	2000.6	2000.6
Stiffness: k (MN/m)	9.0666	8.1668	8.0850
Damping ratio: ξ	0.026443	0.033660	0.035645

The stability lobe diagrams for all the cases for each data set are illustrated in Figure 4.15. The results indicate that the stability lobe diagrams generated for the speed range of 8000-12000 rpm are so close to the stability lobe diagrams generated for the speed range of 6000-12000 rpm, particularly in data set 2. Also, the stability lobe diagrams generated using the identified values in the speed range of 6000-8000 rpm tend to the right side which shows less reduction in natural frequency at low speed than at high speed.

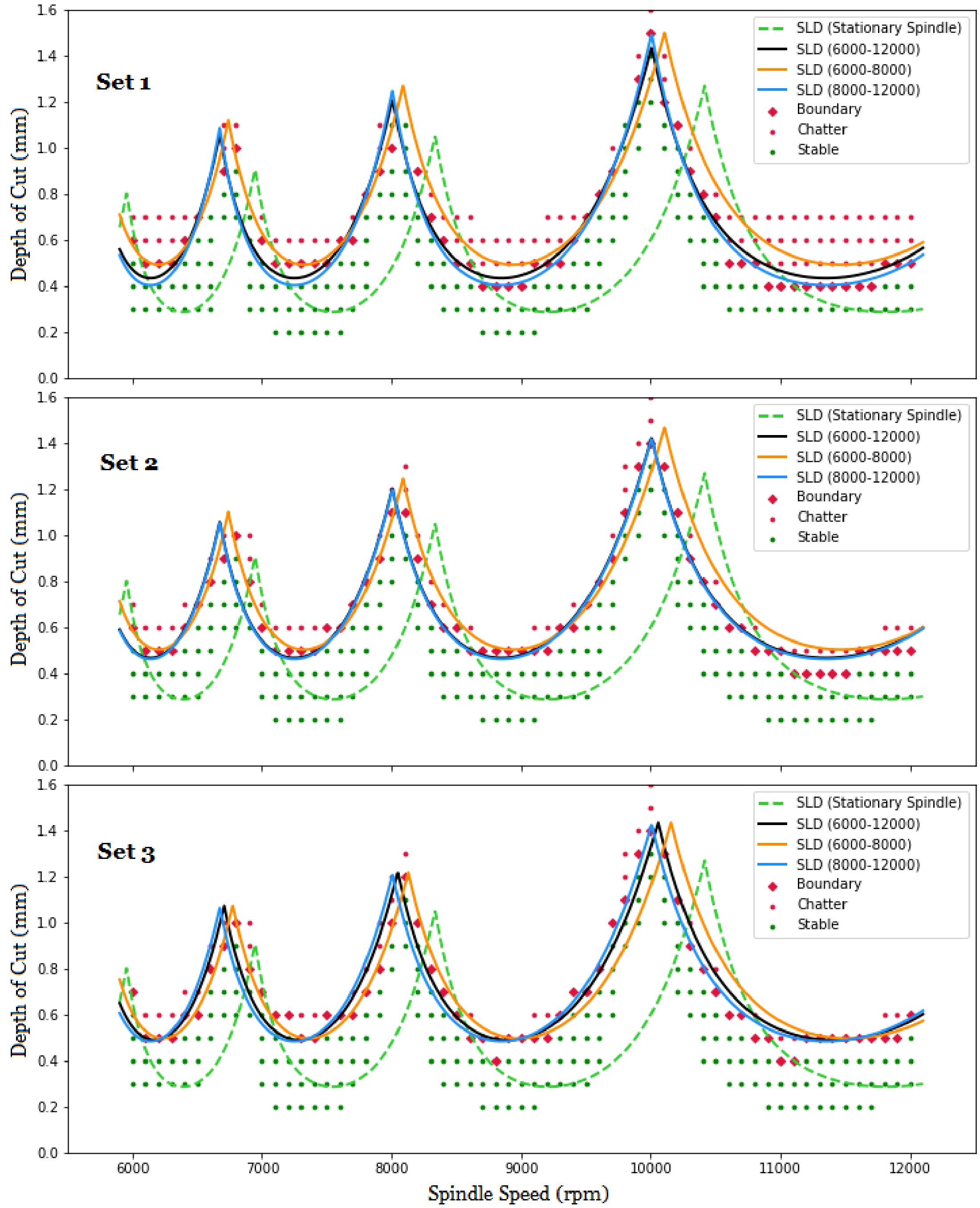

Figure 4.15: Stability lobe diagrams from Newton-Raphson methods using three experimental data sets with 3-flute end mill for different ranges of speed.

Another approach to calculating in-process structural dynamics parameters is to combine all the data sets. Therefore, at each spindle speed, the chatter point with the minimum depth of cut is chosen as the critical chatter point on the stability boundary. So any point above this critical point is chatter, and points below it are stable. The inverse method is applied to this combined data set for three different cases; First on the whole range of speed which is 6000-12000 rpm, then for the low-speed range of 6000-8000 rpm, and finally for the high-speed range of 8000-12000 rpm. The in-process modal parameters derived from the Newton-Raphson algorithm are listed in Table 4.15. The stability lobe diagrams generated based on the extracted modal parameters in this table are illustrated in Figure 4.16. The results in Table 4.15 show that the stiffness increases for the cases in the speed range of 6000-8000 rpm and 8000-12000 rpm in comparison with the identified values considering all the data points in the speed range of 6000-12000 rpm, while the damping ratio slightly decreases. As Figure 4.16 shows the stability lobe diagram generated for the speed range of 6000-8000 rpm tends to shift to the right side of the figure in comparison with the other two in-process stability lobe diagram. This happens since the highest value for natural frequency occurs in the case of the speed range of 6000-8000 rpm.

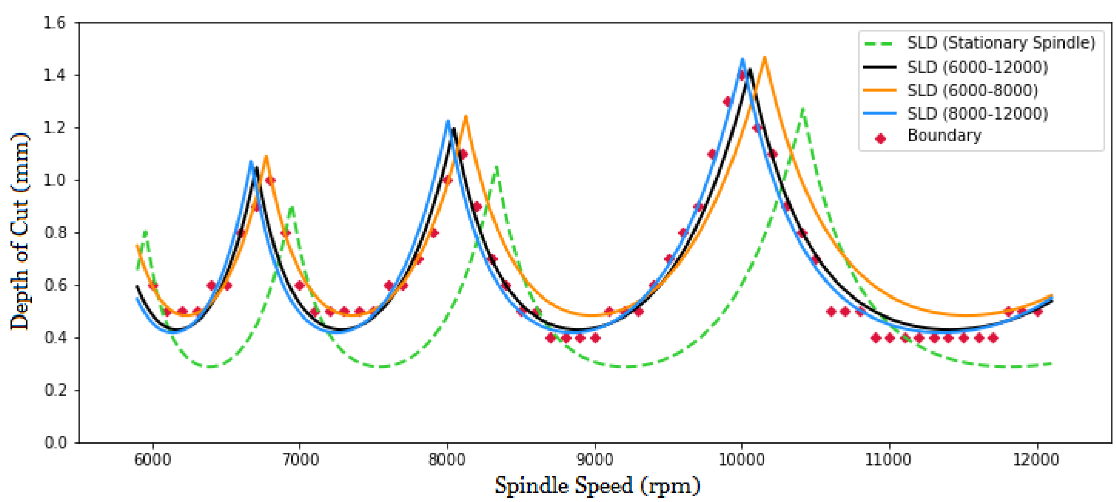

Figure 4.16: Stability lobe diagrams from Newton-Raphson methods combined experimental data set with 3-flute end mill for different ranges of speed.

Table 4.15: In-process Structural dynamics parameters calculated using the inverse method for 3-flute end mill for the combined experimental data set for different spindle speed ranges.

	6000-12000 (rpm)	6000-8000 (rpm)	8000-12000 (rpm)
Natural frequency: f_n (Hz)	2010.9	2030.8	2000.8
Stiffness: k (MN/m)	8.3724	8.4143	8.7564
Damping ratio: ξ	0.030440	0.03407	0.028321

Stability lobe diagrams generated using inverse approach data set 1, 2, 3, and also the combined data set are plotted in Figure 4.17. Since the combined data set includes the least value of depth of cut for the critical chatter points on the boundary at each spindle speed, the stability lobe diagram generated based on this data set can justify data sets 1,2, and 3. Figure 4.17 also shows that SLD generated using the combined data set is so close to the SLD generated using data set 1, while this SLD is a conservative boundary for the data set 2 and 3.

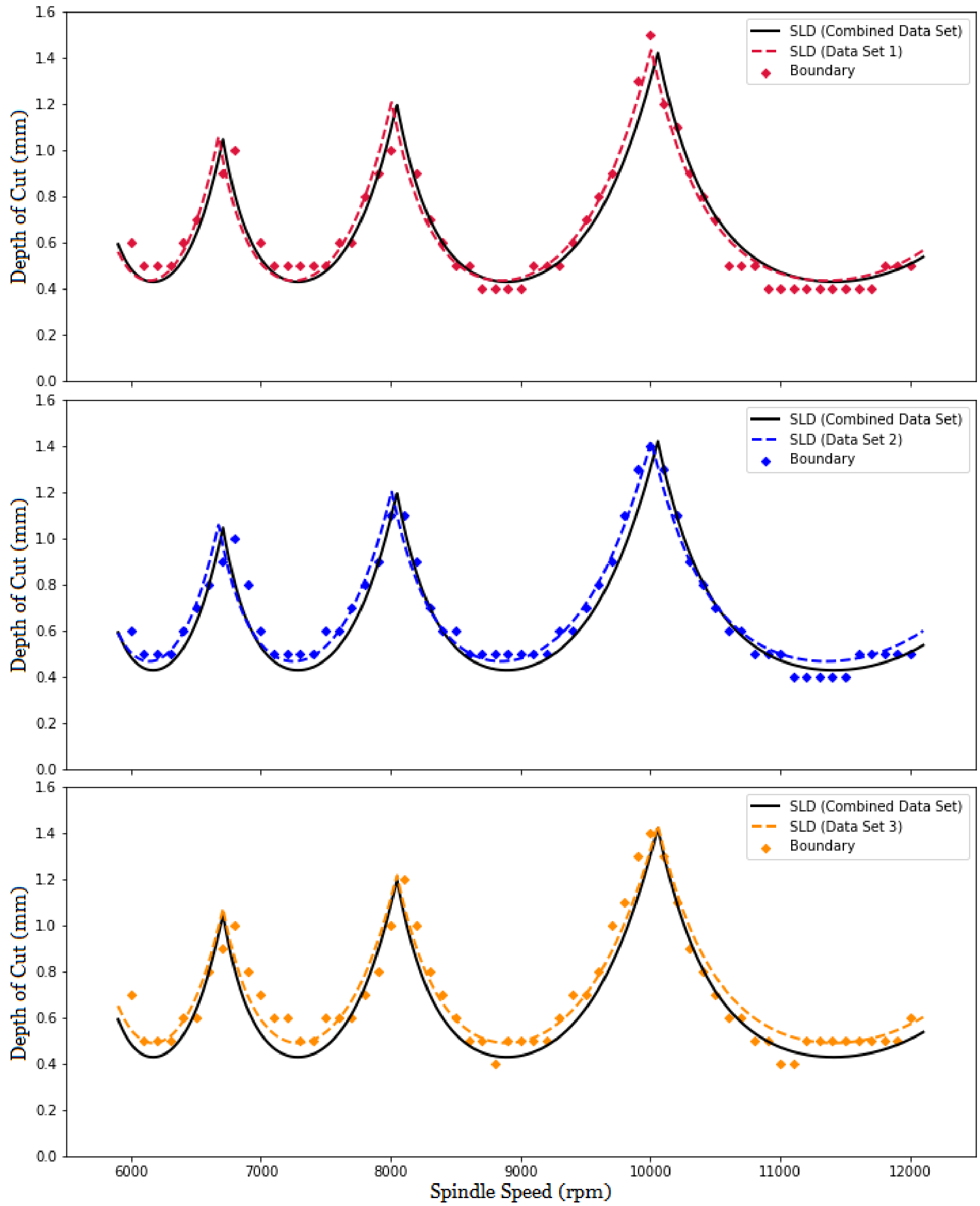

Figure 4.17: Stability lobe diagrams from Newton-Raphson methods using fthe experimental data sets with 3-flute end mill for speed ranges of 6000-12000 rpm.

4.2.4.3 Slot milling using a two-flute end mill

The third set of experimental data [76] considered in this work consists of full-engagement milling of aluminum 7075 plates with a two-flute carbide (ZrN-coated) end mill. The tool has a 0.5-inch diameter with a flute helix angle of 30°. The tool was mounted with a 2.7-inch stick-out. The tool dynamics flexibility is calculated by performing an impact hammer test on the tip of the tool. The frequency response function in X (feed direction) and Y (cross-feed direction) directions are shown in Figure 4.18. Modal parameters calculated from these tests are listed in Table 4.16.

Table 4.16: Modal parameters for the 2-flute end mill at the stationary spindle.

	Feed (X)			Cross-Feed (Y)		
	f_n (Hz)	k (MN/m)	ξ	f_n (Hz)	k (MN/m)	ξ
Mode#1	989.79	23.525	0.04	866.93	26.293	0.03
Mode#2	1215.45	53.863	0.04	1242.66	49.959	0.03
Mode#3	1704.37	11.988	0.02	1712.33	9.206	0.02
Mode#4	1845.40	3.457	0.03	1824.44	5.513	0.02
Mode#5	2626.79	79.974	0.02	1984.74	36.044	0.01
Mode#6	2813.83	188.933	0.01	2604.70	77.025	0.02

The cutting force coefficients are measured by conducting some experiments in the stable region. The radial and tangential are 0.176 and 787.8 MPa, respectively. Three different data sets are collected during the cutting tests. For each data set spindle speed increases from 6000 rpm to 12000 rpm by the step size of 100, and the depth of cut increases from 0.2 mm to 1.2 mm with the step size of 0.1. Each data set includes 238 data points that are labeled and classified as chatter and stable points which are shown in Figure 4.19.

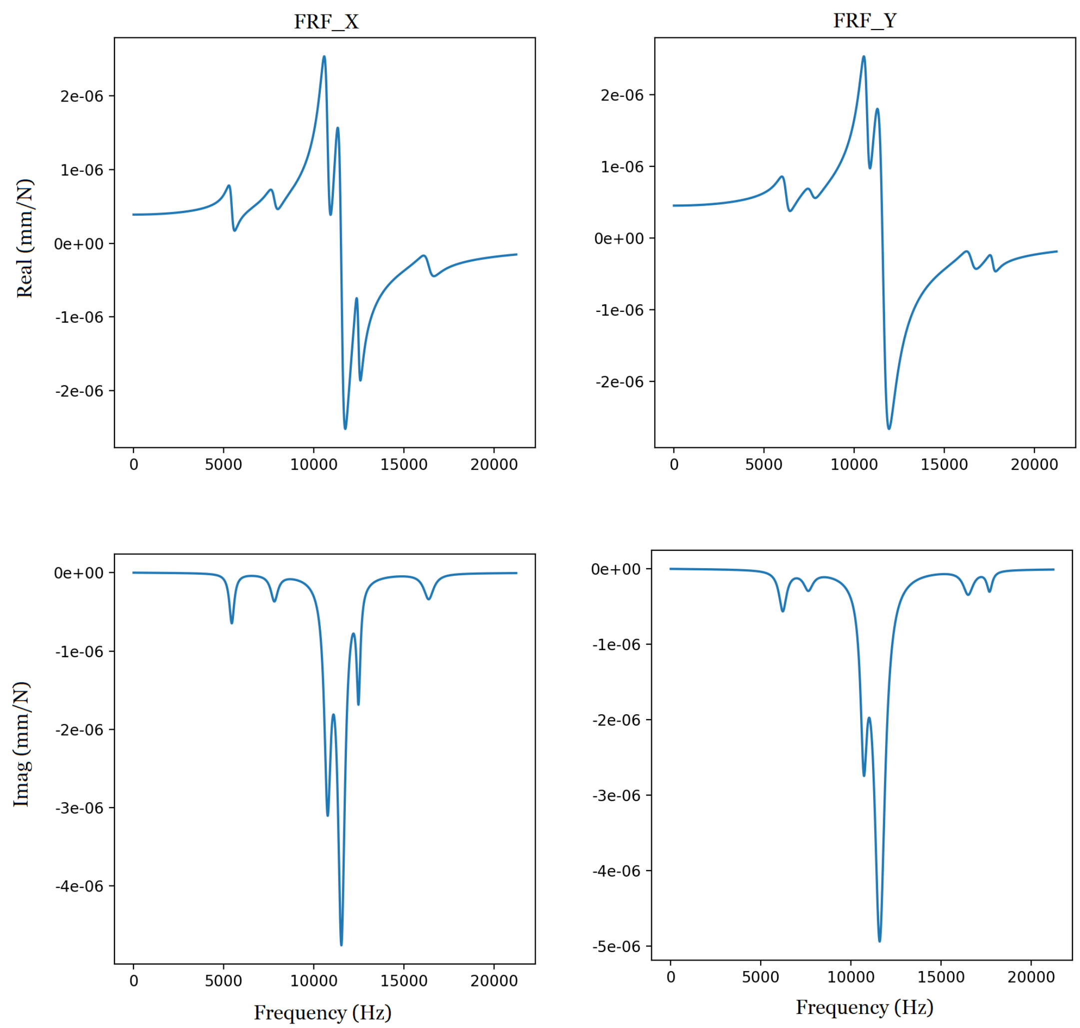

Figure 4.18: Real and Imaginary parts of dynamic flexibility of the 2-flute tool in X and Y directions.

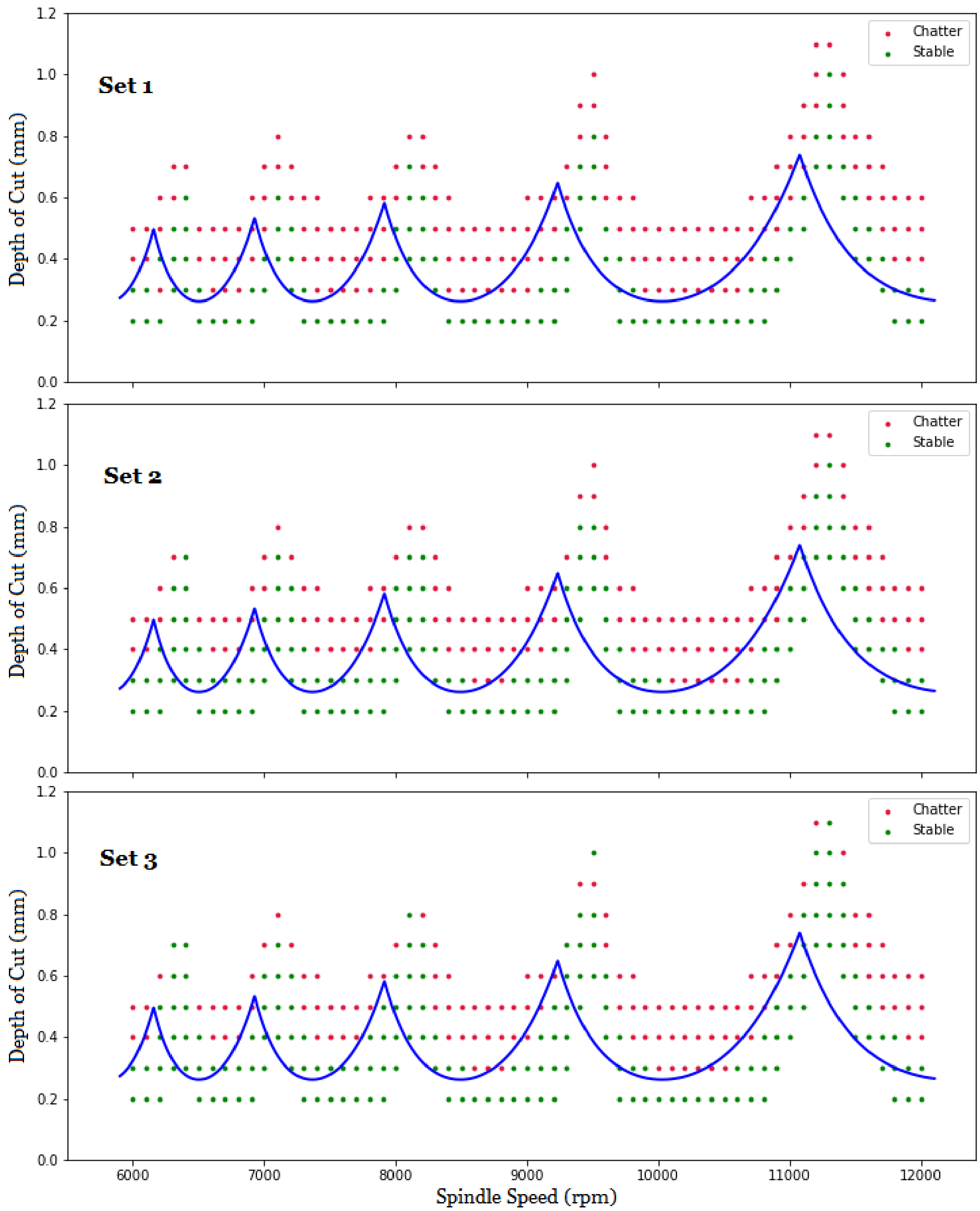

Figure 4.19: Experimental results with 2-flute end mill for three data sets and stability lobe diagrams from impact test on the stationary spindle using zero-order solution.

The values of chatter frequency for the chatter observations on the boundary (chatter point with the minimum depth of cut at each spindle speed value) show that mode 4 in Table 4.16 is the dominant mode and results in an unstable cut in this case. Therefore, only this mode was used in the calculations to generate the stability lobe diagram. Figure 4.19 shows that the stability lobe diagram generated based on the modal parameter measured in stationary spindle can not justify the experimental observations. Similar to the results of the 3-flute case, some points that are labeled as stable in one data set have turned to chatter, and vice versa. So the Newton-Raphson method approach was used to calculate in-process modal parameters for each data set separately. The results for modal parameters for each data for chatter points on the boundary in the spindle range of 6000-12000 rpm are presented in Table 4.17.

Table 4.17: In-process Structural dynamics parameters calculated using the inverse method for 2-flute end mill for three sets of experimental data in the spindle speed range of 6000-12000 rpm.

	Set.1	Set.2	Set.3
Natural frequency: f_n (Hz)	1891.9	1882.4	1882.3
Stiffness: k (MN/m)	5.4890	5.3969	5.5055
Damping ratio: ξ	0.020639	0.024479	0.024605

The stability lobe diagrams generated using the in-process modal parameters in Table 4.17 are illustrated in Figure 4.20 for each data set. This figure shows that, unlike the case of 3-flute end mill, the in-process stability lobe diagrams are located on the left-side of the stability lobe diagrams in Figure 4.19 in which the modal parameters in the stationary spindle are used. This happens because the natural frequency increases during the cutting operations in this example. This result is the opposite of the commonly observed trend of decreasing the natural frequency with increments in the speed. Comparing the results from Table 4.17 with the modal parameters in zero speed condition indicates that the stiffness notably increases in each set while the damping ratio decreases.

The stability lobe diagrams derived from the inverse approach in Figure 4.20 show that some chatter points are still located in stable regions in some data sets particularly in data set 2 and 3 in the speed range of 8000-12000 rpm. Moreover, some stable points are located in the chatter region at low spindle speed. Similar to the case of 3-flute end mill, it is observed that there are different minimum depths of cut for different lobes at low and high speeds. For example in data set 2 and 3, the minimum depth of cut for lobes located in the speed range of 6000-8000 rpm is 0.4 mm while this value is 0.3 mm in the speed range of 8000-12000 rpm. However, it is expected to have the same minimum depth of cut for all the lobes in the stability lobe diagram. To overcome this issue and also calculate more accurate structural dynamic parameters, the spindle speed range was divided into two separate ranges of 6000-8000 rpm and 8000-12000 rpm, and applied the inverse approach to each of these speed ranges separately. The modal parameters derived using the Newton-Raphson method for the speed range of 6000-8000 rpm for three data sets are listed in Table 4.18.

Figure 4.21 shows the stability lobe diagrams generated based on the results from Table 4.18 for the low spindle speed. It should be noted that although the stability lobe diagram is plotted for the speed range of 6000-12000 rpm, only the data points in the speed range of 6000-8000 rpm are used as the input of the Newton-Raphson method algorithm for each data set. Table 4.18 shows that natural frequency increases in each data set compared to the results derived in the speed range of 6000-12000 rpm. Also, the damping ratio and stiffness increase in each data set except for data set 3 where the stiffness is almost the same value.

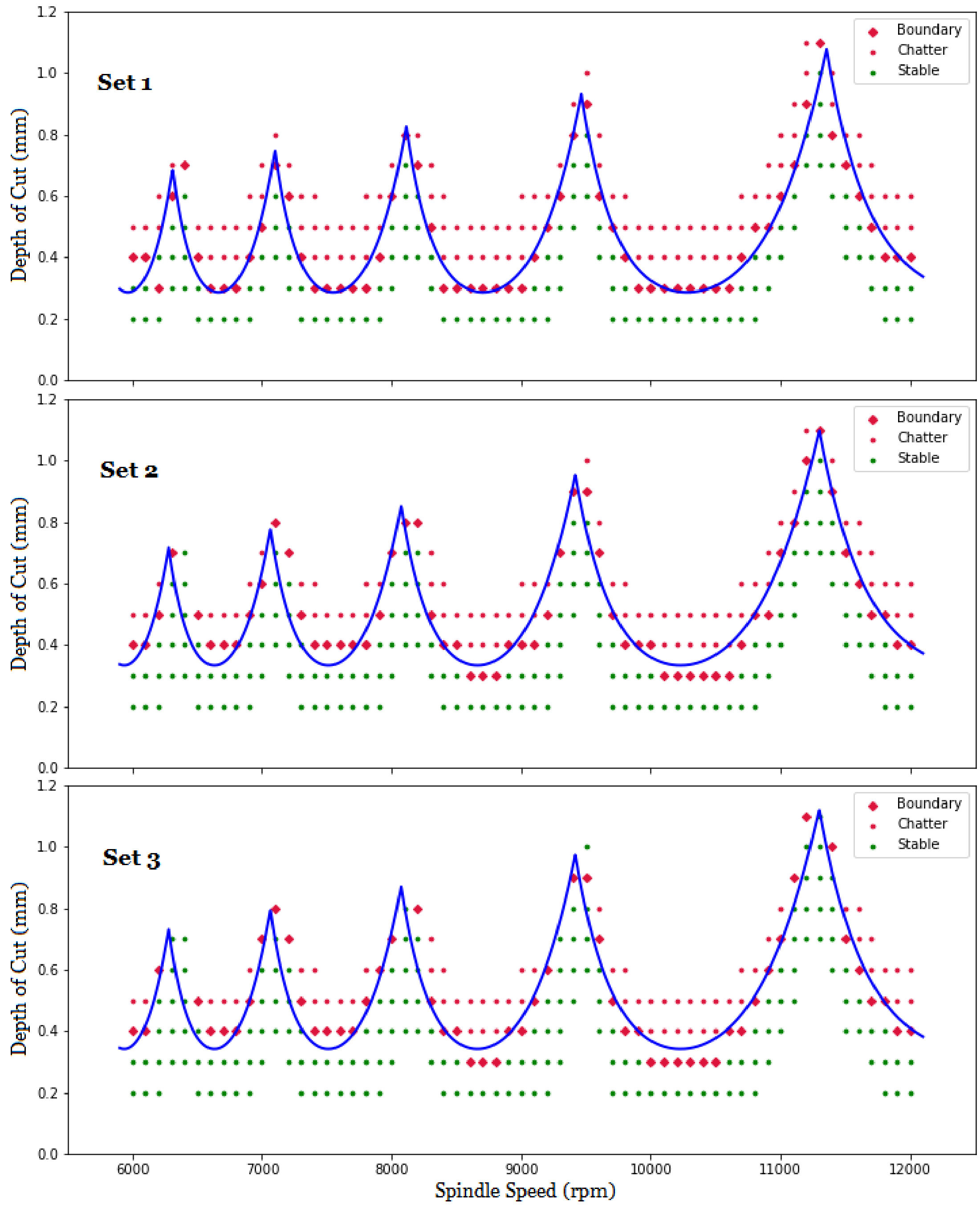

Figure 4.20: Stability lobe diagrams from Newton-Raphson methods on three experimental data sets with 2-flute end mill in the spindle speed range 6000-12000 rpm.

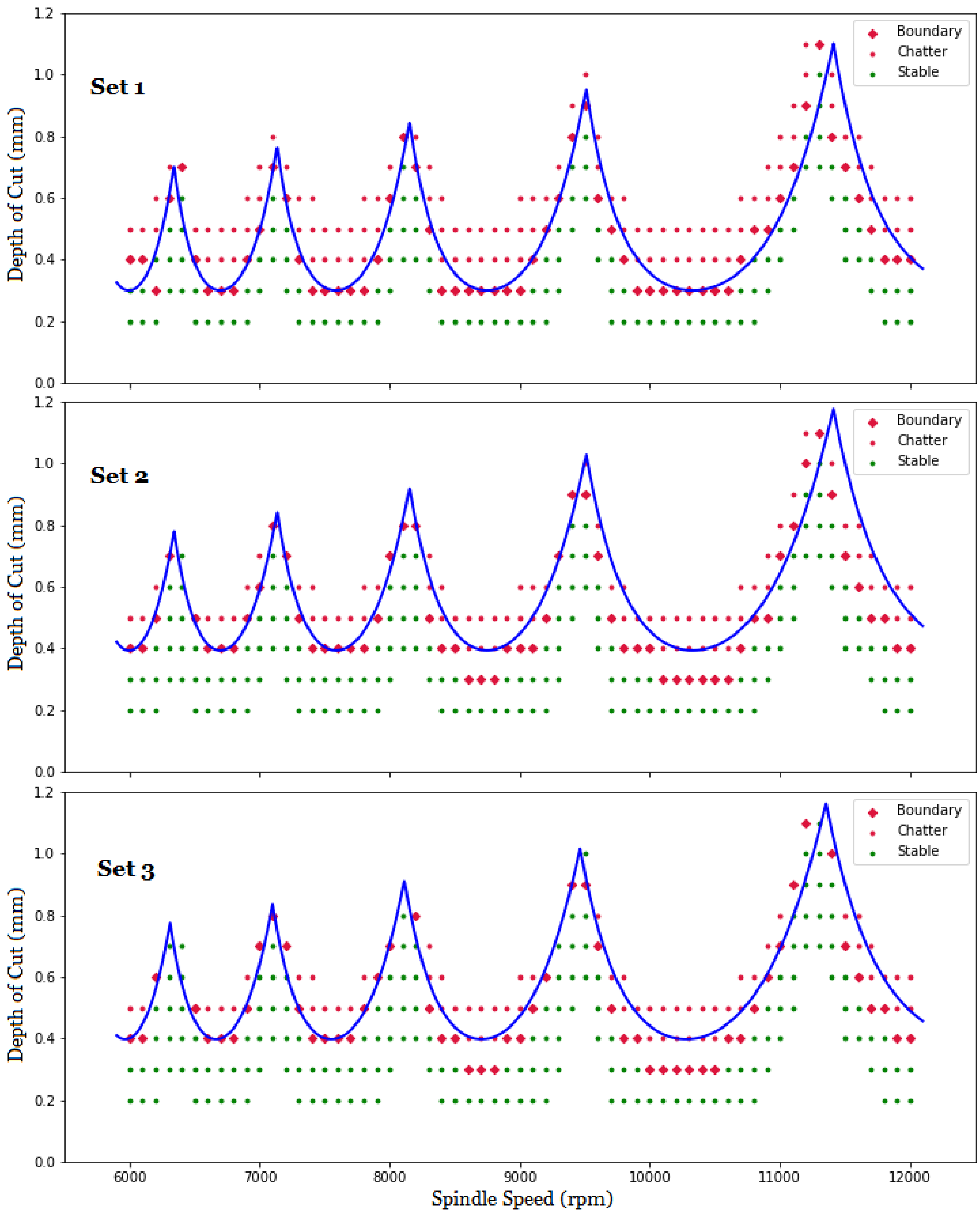

Figure 4.21: Stability lobe diagrams from Newton-Raphson methods on three experimental data sets with 2-flute end mill in the spindle speed range 6000-8000 rpm.

Table 4.18: In-process Structural dynamics parameters calculated using the inverse method for 2-flute end mill for three sets of experimental data in the spindle speed range of 6000-8000 rpm.

	Set.1	Set.2	Set.3
Natural frequency: f_n (Hz)	1901.4	1901.2	1891.8
Stiffness: k (MN/m)	5.5718	5.6157	5.5048
Damping ratio: ξ	0.021329	0.027752	0.028603

To calculate the modal parameters at high speed, the inverse method is applied to points in the speed range of 8000-12000 rpm for each data set. Table 4.19 contains the modal parameters for each data set only considering the data points in the speed range of 8000-12000 rpm. The stability lobe diagrams calculated using the results from Table 4.19 are plotted in Figure 4.22. Again, here only the data points in the speed range of 8000-12000 rpm are used as the input of the Newton-Raphson method algorithm for each data set. However, the data points in the whole range of speed are visualized. Table 4.19 shows that the natural frequency is approximately the same as the results calculated in the speed range of 6000-12000 rpm for each data set. It is also observed that the stiffness values tend to increase while the damping ratio decrease.

Table 4.19: In-process Structural dynamics parameters calculated using the inverse method for 2-flute end mill for three sets of experimental data in the spindle speed range of 8000-12000 rpm.

	Set.1	Set.2	Set.3
Natural frequency: f_n (Hz)	1891.9	1882.4	1882.3
Stiffness: k (MN/m)	5.5718	5.5605	5.9030
Damping ratio: ξ	0.019711	0.021437	0.020775

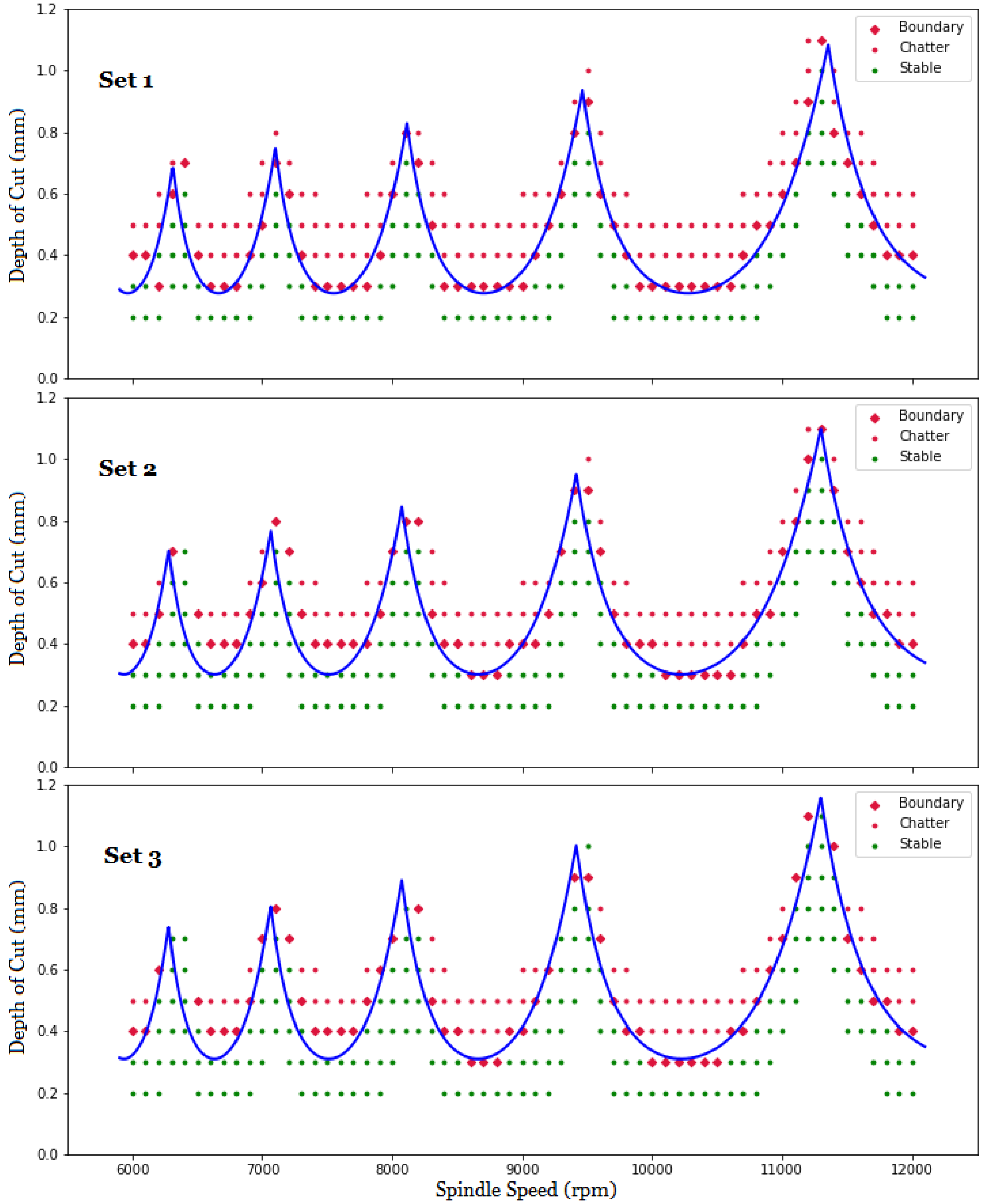

Figure 4.22: Stability lobe diagrams from Newton-Raphson methods on three experimental data sets with 2-flute end mill in the spindle speed range 8000-12000 rpm.

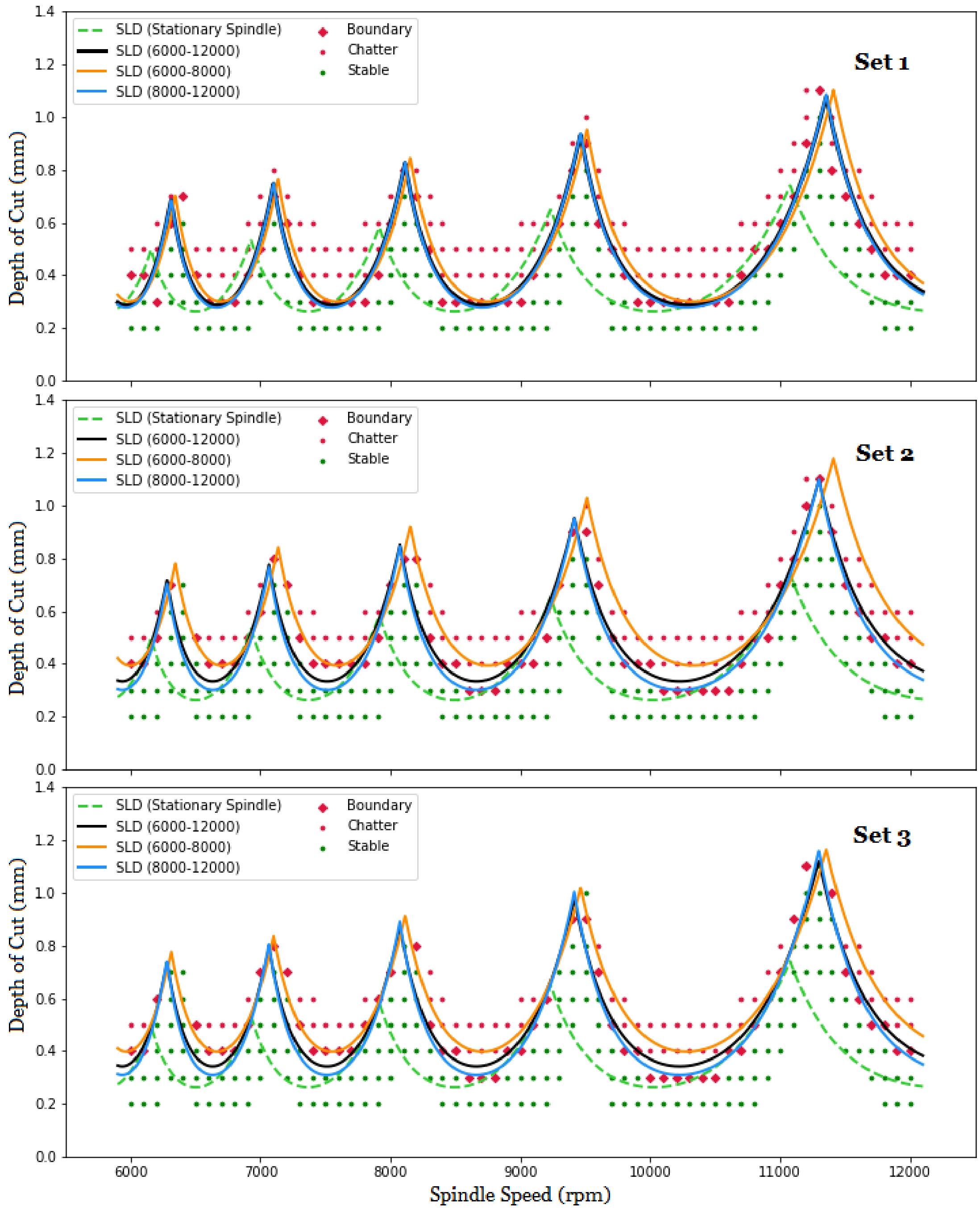

Figure 4.23: Stability lobe diagrams from Newton-Raphson methods using three experimental data sets with 2-flute end mill for different ranges of speed.

The stability lobe diagrams for different speed ranges for each data set are illustrated in Figure 4.23. For data set 1, stability lobe diagrams generated for different speed ranges are so close to each other, since the experimental data points have the same minimum depth of cut of the speed range of 6000-12000 rpm. However, the stability lobe diagram for the speed range of 6000-8000rpm is located on the right-side of the other two stability lobe diagrams. The results for data set 2 and 3 follow a similar trend. The stability lobe diagrams for the speed range of 6000-12000 rpm and 8000-12000 rpm are close to each other. However, the stability lobe diagrams for the speed range of 8000-12000 *rmp* have a smaller depth of cut for each speed value. In the case of low-speed range, although the stability lobe diagram generated using the modal parameters in the speed range of 6000-12000 rpm cover most of the chatter points, the objective function value is smaller if the modal parameters extracted for the speed range of 6000-8000 rpm are used to generate the stability lobe diagram for this range of speed.

As discussed before, some of the chatter points located on the stability boundary in one data set turn out to be stable in another one. So another approach to calculating in-process structural dynamics parameters is to combine all the data sets. In this case, the chatter points with the minimum depth of cut are considered critical chatter points on the boundary for each spindle speed. That means if a point is stable in one data set but is labeled as chatter in another data set, that point will be labeled as chatter in the combined data set. Thus, the stability boundary is made by selecting the critical chatter points. It is assumed that any point above this boundary is chatter, and any point below that is stable. The modal parameters calculated through the inverse approach for the combined data set for three different speed range are listed in Table 4.20, and the stability lobe diagram generated based on these results for each set of data are plotted in Figure 4.24.

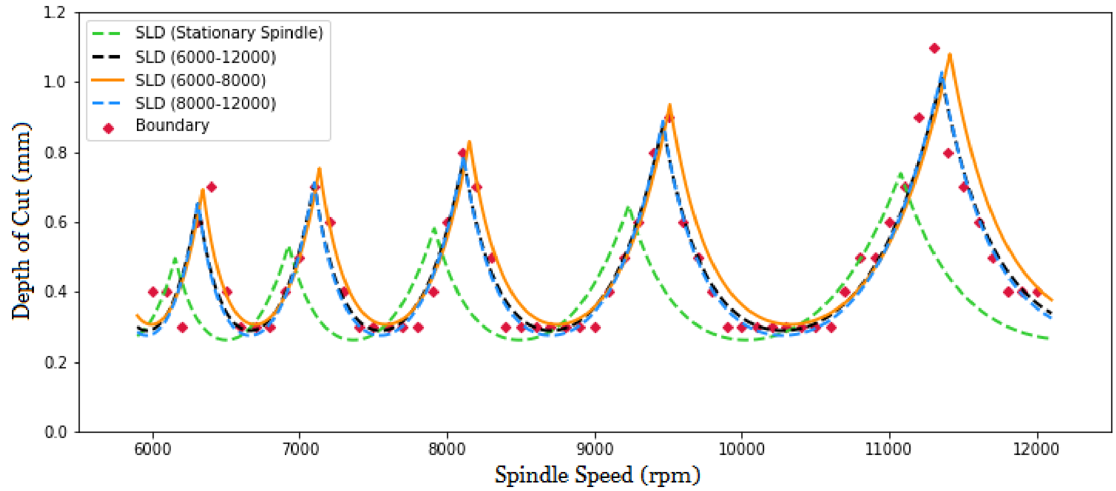

Figure 4.24: Stability lobe diagrams from Newton-Raphson methods combined experimental data set with 2-flute end mill for different ranges of speed.

The results in Table 4.20 show that the calculated natural frequency values are the same for the speed range of 6000-12000 rpm and 8000-12000 rpm. But this value increases in the case of 6000-8000 rpm which results in shifting the stability lobe diagram to the right as shown in Figure4.24. It is also observed a reduction in damping ratio values while the stiffness values rise in these two cases in comparison to the results derived for the speed range of 6000-12000 rpm.

Table 4.20: In-process Structural dynamics parameters calculated using the inverse method for 2-flute end mill for the combined experimental data set for different spindle speed ranges.

	6000-12000 (rpm)	6000-8000 (rpm)	8000-12000 (rpm)
Natural frequency: f_n (Hz)	1891.9	1901.4	1891.9
Stiffness: k (MN/m)	5.0674	5.4063	5.2211
Damping ratio: ξ	0.022817	0.022491	0.020899

Figure 4.25 visualizes the stability lobe diagram generated by the identified values

of modal parameters for three sets of data for the speed range of 6000-12000 rpm. It also shows the Stability lobe diagram for the case of combined data set for the same range of speed. It can be seen that the stability lobe diagram generated using the modal parameters extracted from the combined data set is so close to the stability lobe diagram of data set 1. this is because data set 1 has the minimum critical depth of cut of all the lobes. The SLD for the combined data set also covers the most chatter points in data sets 2 and 3.

Note that in the three different empirical examples, the data set covered 21, 57, and 61 pairs of the depth of cut and spindle speed. In contrast, there were only 3 unknown parameters found through the Newton method. A large number of observations vs. a small number of parameters (inputs of the SLD function) implies that overfitting will not be a serious issue when finding the parameters.

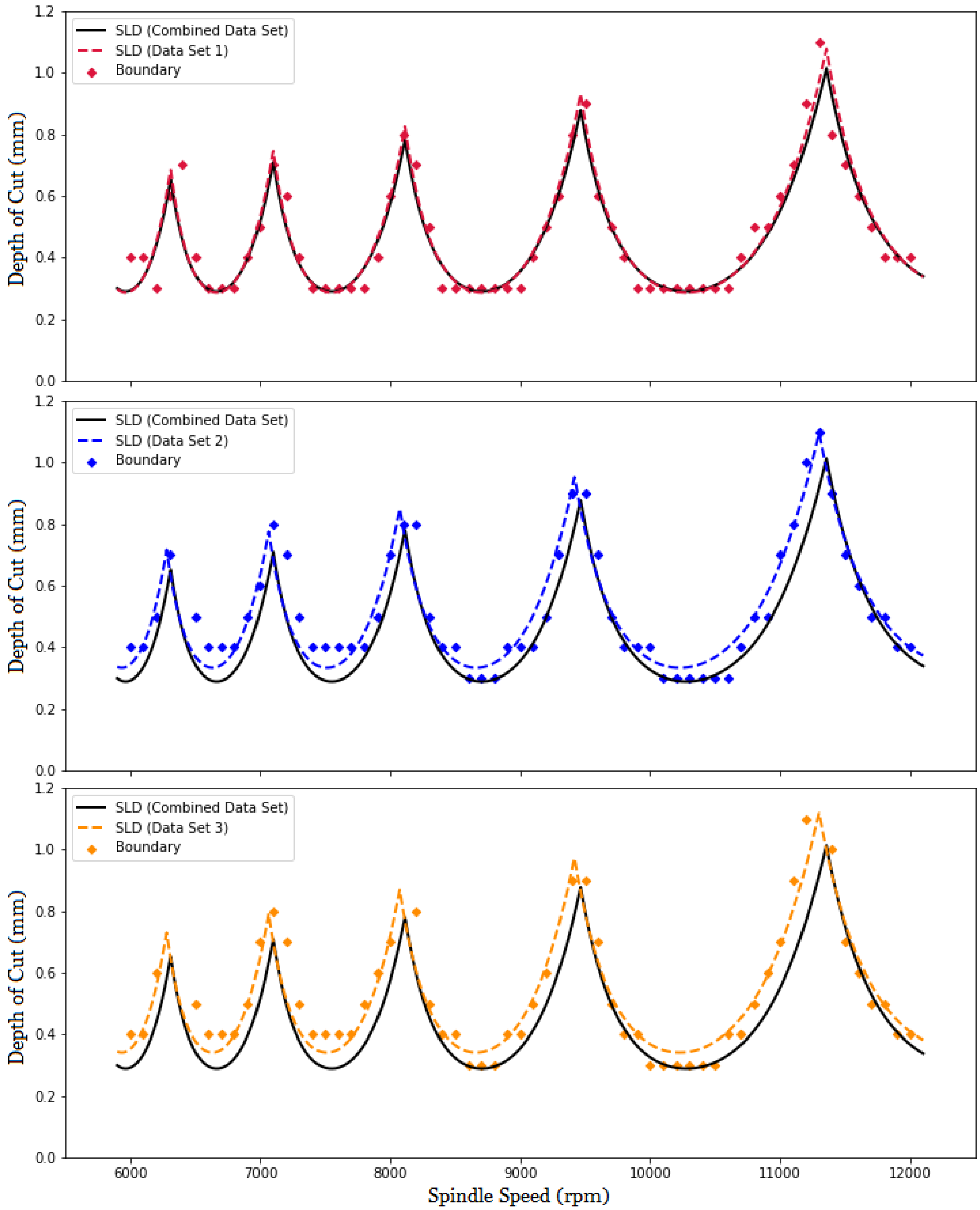

Figure 4.25: Stability lobe diagrams from Newton-Raphson methods using combined and three sets of experimental data with 2-flute end mill for speed ranges of 6000-12000 rpm.

4.3 Uncertainty and Sensitivity Analysis in Stability Lobe Diagram

This work includes defining and measuring the uncertainty of each structural dynamics parameter derived through the inverse approach. Here the main question is: To what extent, the uncertainty of each input parameter leads to the uncertainty in the SLD? For instance, if the first parameter is measured as $p_1 = 10.0 \pm 0.2$, then how much the SLD would be shifted based on the standard deviation of p_1 (here 0.1), and how that shift can be quantified?

In this study, first, the in-process structural dynamics parameters are extracted, given in-process SLD. Conventionally, the SLD is built having the structural dynamics parameters using either frequency-domain or time-domain methods. However, the calculated SLD is not reliable as these parameters change during cutting operations, and the experimental results do not follow the stability boundary. To overcome this issue, the method presented in Section 4.2 is used. Three examples based on synthetic data are presented to illustrate the approach. Also, the algorithm is evaluated on an empirical data set and verified its ability to improve the stability boundary. Furthermore, results from sensitivity analyses performed to calculate the exposure of the stability lobe diagram to each structural dynamics parameter are presented. Although there are some studies in the literature to calculate in-process structural dynamics parameters, they only focus on a few points on the boundary. In this work, a wide range of spindle speed values is covered by using more data points on the boundary.

4.3.1 Newton-Raphson Method with Adjustments

In this study, Mean Log Absolute Error (MLAE) is used as the objective function for the evaluation of each iteration in the Newton method. MLAE is less sensitive to high differences between the reference and the guessed SLDs and therefore may result in smoother convergence of the iterative algorithm.

$$\begin{aligned} MLAE &= MLAE(p_1^*, \cdots, p_m^*) \\ &= \frac{1}{n}\Sigma_{i=1}^{n} \log(1 + |b_i^{exp} - b_i^*|) \end{aligned} \tag{4.11}$$

Here, $(p_1^*, \cdots, p_m^*)$ indicates the initial guess set. b_i^{exp}'s are the set of the depth of cut in the reference SLD and b_i^*'s are the set of the depth of cut in the guessed SLD. Then, the guessed value for each unknown parameter is updated using Eqn. 4.12:

$$p_i^* \leftarrow p_i^* - \frac{MLAE \times S_i}{||S||^2} \times \alpha \quad ; \quad i = 1, 2, \cdots, m. \tag{4.12}$$

Here, α controls the pace ($\alpha \in (0, 1]$), and one may assume $\alpha = 1$ for simplicity of the notation. S_i denotes the sensitivity of the objective function with respect to each parameter which is calculated as follows:

$$\begin{aligned} S_i &= \frac{\partial MLAE}{\partial p_i^*} \\ &= \frac{MLAE(p_1^*, \cdots, p_i^* + \epsilon, \cdots, p_m^*) - MLAE}{\epsilon} \end{aligned} \tag{4.13}$$

where ϵ is a small value added to a guessed parameter (p_i^*) to derive the partial derivative of the objective function with respect to that parameter.

Some adjustments were also applied to enhance the Newton method and accelerate its convergence, as dealing with multivariate functions in the Newton method is sometimes challenging. In Particular, using the Newton-Raphson method, there is a possibility of getting stuck in the local minima. To overcome this issue, a specific threshold is set for the objective function. If the algorithm was not able to improve the objecting function at least by that threshold after a certain number of consecutive iterations, some e.g. 5% jumps are added in each/some parameters. However, adding random jumps does not necessarily improve the results. Thus, the jumps are tried,

Table 4.21: Values used to generate synthetic data set for the three different examples.

Parameter	Ex.1	Ex.2	Ex.3
Natural frequency: f_{nx} (Hz)	903.0	500.0	900.0
Stiffness: k_x (MN/m)	12.53	8.00	9.000
Damping ratio: ξ_x	0.0300	0.0200	0.0200
Natural frequency: f_{ny} (Hz)	903.0	500.0	950.0
Stiffness: k_y (MN/m)	12.53	8.00	10.00
Damping ratio: ξ_y	0.0300	0.0200	0.0100
Tangential cutting force: k_t (MPa)	556.31	695	2173
Normal cutting force: k_n	0.404	0.404	0.268
Start angle: ϕ_s (deg)	0.000	0.000	126.9
Exit angle: ϕ_e (deg)	180.0	180.0	180.0
Number of flutes: N_t	2	4	3

but only applied if they can successfully improve the objective function. This way the algorithm gets a chance to run away from local minima. Moreover, during the experiments, it is observed that sometimes the algorithm fails on the critical points of the stability lobe diagram. Therefore, the algorithm needs to be made more sensitive to the SLD errors at those critical points. That is achievable by giving more weights to the critical points rather than equal weights that are implied in Eq.4.10.

Three different examples were studied to derive the structural dynamics parameters using the multivariate Newton-Raphson method approach. For each example, synthetic data is generated using the Fourier series approach (Zero-Order solution [77]). Each data set includes values of spindle speed and the corresponding depth of cut on the stability boundary. Table 4.21 shows the structural dynamics parameters and cutting parameters used to generate these data sets.

In each example, the SLD made using the information provided in Table 4.21 is considered as the reference SLD. The guessed SLD is made through the Newton-Raphson algorithm and then compared to the reference SLD.

It is assumed that the synthetic data set for each case comes from an experiment,

Table 4.22: Results using Newton method approach for the three examples.

Exp	Value	f_{nx}	k_x	ξ_x	f_{ny}	k_y	ξ_y
Ex.1	Target	903.0	12.53	0.0300	903.0	12.53	0.0300
	Predicted	910.4	13.44	0.0287	910.4	13.44	0.0286
Ex.2	Target	500.0	8.00	0.0200	500.0	8.00	0.0200
	Predicted	503.5	8.66	0.0196	503.5	8.66	0.0196
Ex.3	Target	900.0	9.00	0.0200	950.0	10.00	0.0100
	Predicted	906.8	9.49	0.0183	947.7	9.56	0.0104

and the values for cutting parameters, i.e., normal and tangential cutting forces, number of flutes, and start and exit angles are known. Thus, only the structural dynamics parameters are unknowns, and the goal here is to derive them through the Newton-Raphson approach. It is assumed that there is only one dominant mode in each direction for each example. Therefore, there are totally six unknown parameters for each example. The Newton-Raphson approach is applied for each example separately.

Table 4.22 presents the results derived from the Newton-Raphson algorithm. The predicted values are the results found using the algorithm and the target values are the parameters used to build the reference SLD. The results show that the algorithm converges and finds the parameters that can justify the reference SLD for all the cases, as the predicted values are fairly close to their targets. Figure 4.26 shows the reference and the predicted stability lobe diagrams. The blue curves are generated based on target values and are called the reference SLDs, and the orange curves are generated based on the predicted values after 60 iterations and are called the guessed SLDs. As shown in Figure 4.26, in each example, the two boundaries are very close to each other after 60 iterations. Some of the Newton-Raphson method iterations are visualized for example 3 in Figure 4.27. As Figure Figure 4.28 and 4.27 show, the iterative process does not necessarily imply a monotone convergence. Nevertheless, after enough iterations, the guessed SLD is similar to the reference SLD. Note that

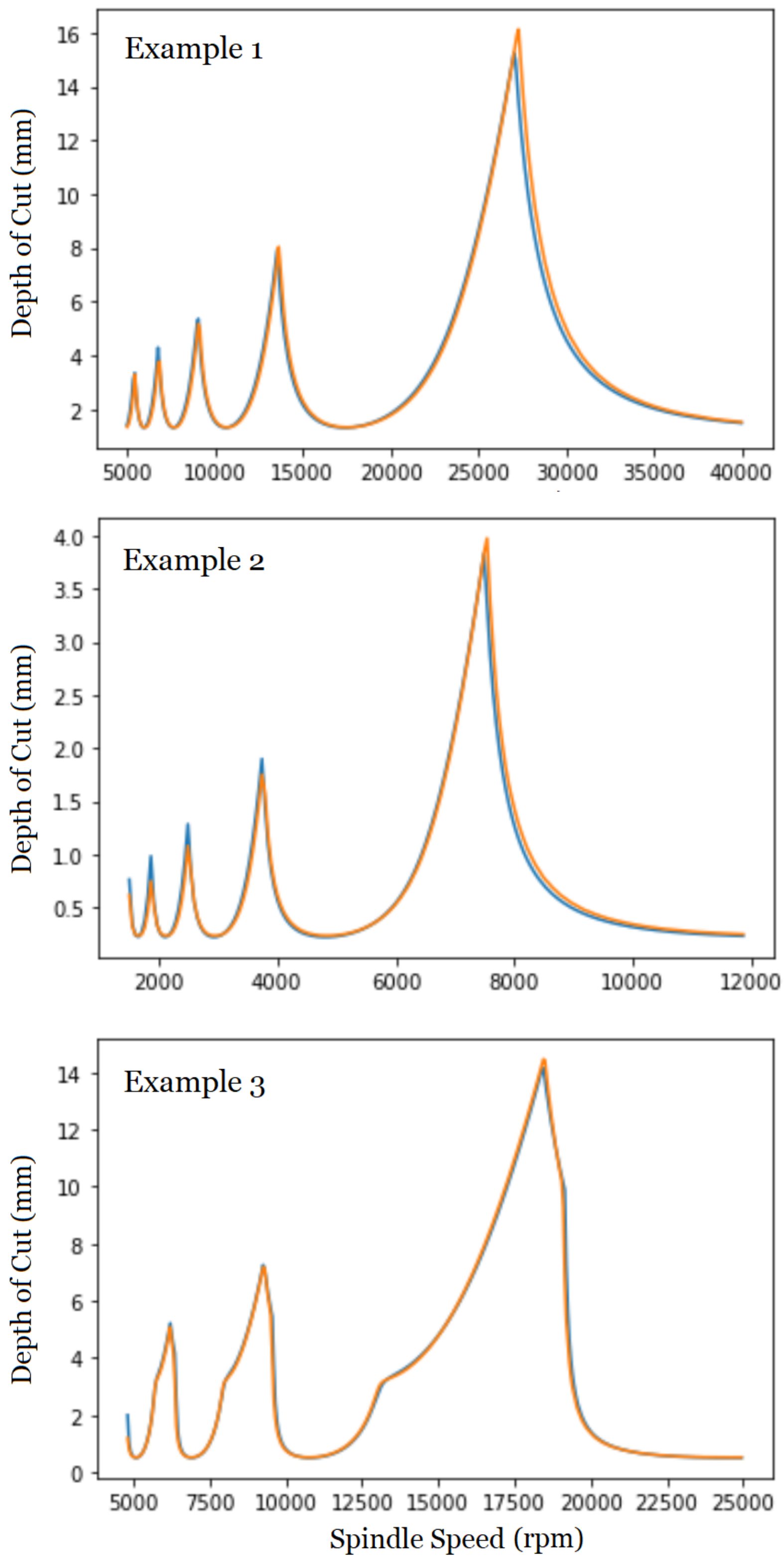

Figure 4.26: Final SLDs for the three examples. Blue curves are the target SLDs while the orange curve shows the calculated SLD in each example.

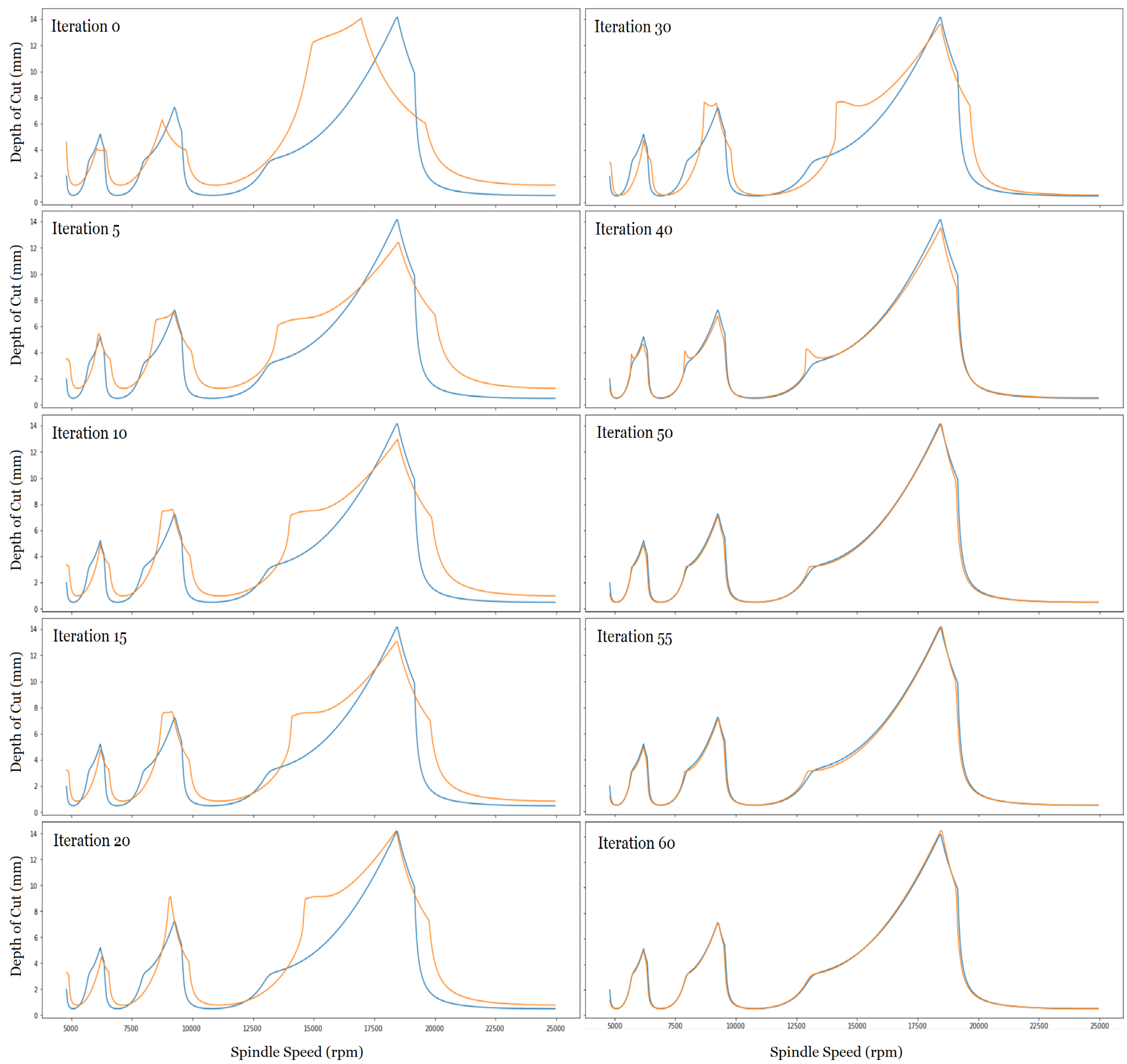

Figure 4.27: Some of the steps in Newton-Raphson approach for example 3. The blue curve is the empirical SLD while the orange curve is the guessed SLD at each step.

the algorithm may keep iterating more to reduce the errors. However, that may also imply more computational cost, while the errors are already negligible, and the results might be already acceptable.

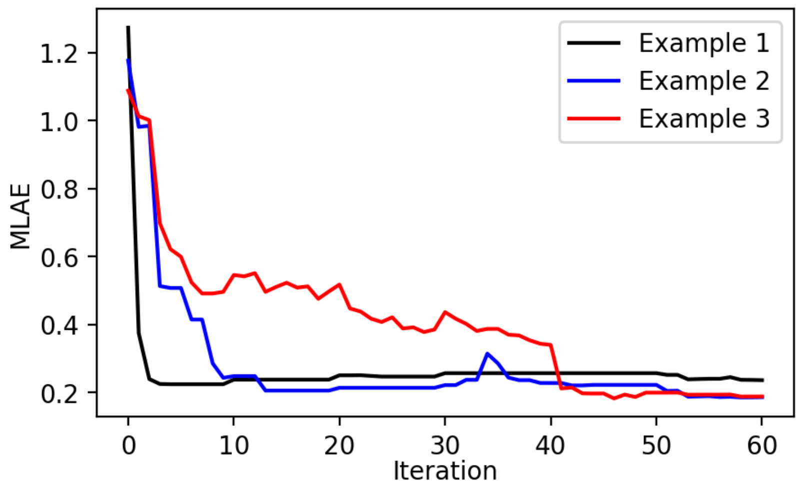

Figure 4.28: The objective function (MLAE) measures the error terms through iterations.

4.3.2 Methodology of Sensitivity Analysis

To analyze the sensitivity of the stability lobe diagram with respect to different parameters, two different approaches are utilized. First, three different examples of SLD using three different parameter sets are tried. For each SLD, the parameters are changed one-by-one by $\epsilon\%$ and a modified SLD is generated each time for different values of $\epsilon \in [-25, 25]$. Then the modified SLD is compared with the original SLD using Mean Squared Error (MSE) for different values of ϵ. Note that when each parameter is changed, the other parameters are kept constant. The different MSE plots will help to analyze the sensitivity of the SLD to each parameter, when that parameter is changed by different ratios. The above-mentioned steps are summarized in Algorithm 1. The predicted parameter sets $(f_{nx}, k_x, \zeta_x, f_{ny}, k_y, \zeta_y)$ as specified in Table 4.22 were used for the three examples.

Figure 4.29 visualizes the results. As shown in the figure, the sensitivity of the SLD with respect to different parameters differs from one example to another. However, generally, the SLD appears to be much more sensitive to f_{nx} and f_{ny} than to the other structural dynamics parameters. Note that the vertical scale for these two

Algorithm 1 Sensitivity analysis on exact parameter set

Input: Parameters=$\{p_1, \cdots, p_m\}$

Output: MSE in SLD when changing each parameter

Make the original SLD: $SLD^* = \{(\Omega_i^*, b_i^*)|\ i = 1, \cdots, n\}$

for j in $1, \cdots, m$ **do**

  for ϵ in $\{-0.20, -0.15, \cdots, +0.20\}$ **do**

    Change the parameters to P':

      $P' = \{p_1, \cdots, (1+\epsilon)p_j, \cdots, p_m\}$

    Make modified SLD using P':

      $SLD' = \{(\Omega_i^*, b_i^{'})|\ i = 1, \cdots, n\}$

    Compute MSE: $MSE_{j,\epsilon} = \frac{1}{n}\sum_{i=1}^{n}(b_i^* - b_i^{'})^2$

  end for

end for

parameters is 20 times larger than other subplots in Figure 4.29 to cover a different range of changes.

The variations in sensitivity plots of different examples as reflected in Figure 4.29, inspire us to use a more generalized approach to aggregate the observations of the sensitivity in different cases with a large number of simulations.

In Figure 4.29, it is noted that the plots are convex in most cases. This is expected. For most iterative algorithms, convexity helps the convergence. However, there are some exceptions, e.g. frequency in example 3, where the sensitivity curve is not convex. Note that all the adjustments and improvements introduced in Section 4.2.2 are to help the algorithm convergence.

In the second approach, the analysis is not confined within the specific parameter set $P = (p_1, \cdots, p_m)$ based on which the original SLD is generated. Instead, one may search and measure the sensitivity of SLD in the neighborhood around a given parameter set. In a Monte Carlo simulation, one may repeatedly choose a new parameter set $P^* = (p_1^*, \cdots, p_m^*)$ where each parameter p_i^* is randomly chosen from the uniform distribution e.g. from $[0.9p_i\ ,\ 1.1p_i]$ or generally from $[(1-t)p_i\ ,\ (1+t)p_i]$

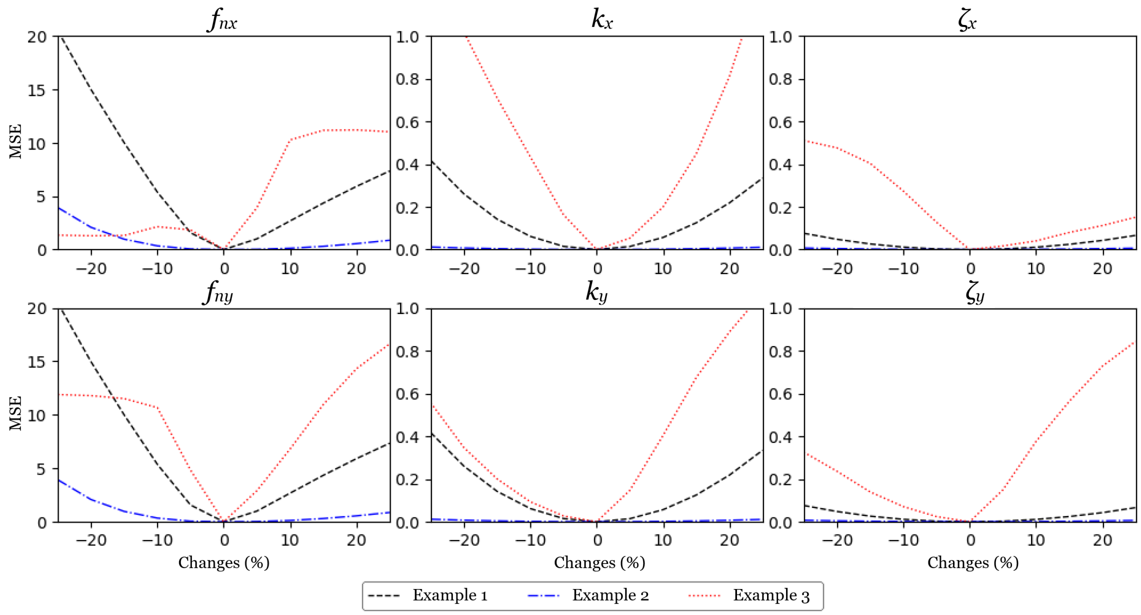

Figure 4.29: Sensitivity of the stability lobe diagram to the changes in structural dynamics parameters.

where t defines the width of the neighborhood. Then the sensitivity of the SLD to each corresponding parameter p_i is measured, using MSE between the SLD using P^* and its modified version where the corresponding parameter is again changed by a small ratio, e.g. $\epsilon = 1\%$. Finally, different results from different Monte-Carlo paths over each parameter are aggregated using aggregators such as mean and standard deviation. The steps are summarized in Algorithm 2. Table 4.23 shows the results of the Monte Carlo simulation with $N = 10,000$ iterations aggregating the sensitivities by the means and the standard deviations. The predicted values in example 1 were used as the given parameter set around which the neighborhood of parameters is constructed.

It is immediately observable from Table 4.23 that SLD sensitivities show large variations in different simulations. But generally, the SLDs are much more sensitive to f_{nx} and f_{ny} than the other structural dynamics parameters.

Also, the Algorithm 2 was applied to empirical data from [2] as discussed in Section 4.2.4.1 using the same setting as used for example 1. Here, the Newton-Raphson

Algorithm 2 Monte Carlo based sensitivity analysis

Input: Parameters=$\{p_1, \cdots, p_m\}$, Neighborhood width t, Number of paths N

Output: MSE in SLD when changing each parameter

for $path$ in $1, \cdots, N$ **do**:

  for j in $1, \cdots, m$ **do**

    $upperbound \leftarrow (1+t) \times p_j$

    $lowerbound \leftarrow (1-t) \times p_j$

    $p_j^* \leftarrow uniform[lowerbound\ ,\ upperbound]$

  end for

  Make the reference SLD using P^*:

    $SLD^* = \{(\Omega_i^*, b_i^*)|\ i = 1, \cdots, n\}$

  for j in $1, \cdots, m$ **do**

    Modify the parameters to P' changing p_j^*:

      $P' = \{p_1^*, \cdots, (1+\epsilon)p_j^*, \cdots, p_m*\}$

    Make modified SLD using P':

      $SLD' = \{(\Omega_i^*, b_i')|\ i = 1, \cdots, n\}$

    Compute MSE:

      $MSE_{j,path} = \frac{1}{n}\sum_{i=1}^{n}(b^* - b')^2$

  end for

end for

for j in $1, \cdots, m$ **do**

  Aggregate the results over parameter j:

    $meanMSE_j = \frac{1}{N}\sum_{path=i}^{N} MSE_{j,path}$

    $stdMSE_j \quad = \{\frac{1}{N}\sum_{path=i}^{N}(MSE_{j,path} - meanMSEj)^2\}^{1/2}$

end for

results from Table 4.10 were used as target parameters. The results are mentioned in Table 4.24. As Table 4.24 shows, again the SLD has the highest sensitivity to the natural frequency. That is why in Table 4.10 where the derived frequencies from the Newton-Raphson method and Method 2 are quite similar, the MSEs are close as well. As Table 4.24 suggests, the SLD is less sensitive to the other parameters, k and ζ. That is why the difference between the derived parameters from the two above-mentioned methods, only results in 20% difference in the Final MSEs (0.000574 in Method 2 vs. 0.000459 in Newton-Raphson).

Table 4.23: Results of Monte Carlo simulation measuring the sensitivity of SLD with respect to different structural dynamics parameters on example 1.

Measure	f_{nx}	k_x	ζ_x	f_{ny}	k_y	ζ_y
Mean Sensitivity	0.06610	0.00080	0.00025	0.06798	0.00078	0.00026
SD of Sensitivity	0.03202	0.00029	0.00012	0.03174	0.00026	0.00013

Table 4.24: Results of Monte Carlo simulation measuring the sensitivity of SLD with respect to different structural dynamics parameters on empirical data from [2].

Measure	f_n	k	ζ
Mean Sensitivity	7.92E-04	3.29E-06	1.86E-06
SD of Sensitivity	1.34E-04	5.45E-07	3.24E-07

4.3.3 Results & Discussion

In this work, the sensitivity of the stability boundary with respect to machine dynamics parameters is investigated. Generally, these parameters are calculated by applying an impact hammer test in the idle state of the machine which results in generating an unreliable stability boundary. This happens because these parameters vary during the cutting process. Thus, a hybrid approach was introduced to finding the in-process structural dynamics parameters under which the physics-based models can support the empirical data. In this approach, a multivariate Newton-Raphson method was utilized to combine the theory with the experimental results. Three synthetic data sets were used to replace the experimental boundary in this study. The algorithm was evaluated as it converged to the correct answers in those three cases and successfully found the underlying structural dynamics parameters. Also, the algorithm was evaluated on an empirical data set, and its ability to improve the stability boundary was verified. The results derived from the algorithm were used to discover the sensitivity of the stability boundary with respect to each parameter. Two different methods were utilized for this purpose. Although the stability border shifts as any structural dynamics parameter changes, the results showed that the natural frequency is the most sensitive parameter.

CHAPTER 5: CONCLUSIONS

In this dissertation, a multivariate Newton method was introduced for the inverse problem. While usually the stability lobe diagram is constructed having the machining structural parameters, this study discusses how one may retrieve the structural parameters, having the SLD. The physics-based stability lobe diagram is usually generated using the structural dynamics and the cutting parameters. However, since the machine dynamics are measured in the stationary spindle, the generated SLD is not reliable as the machine behavior may vary during the cutting operations. Besides, measuring structural dynamics parameters under cutting conditions is difficult and needs new equipment. This study provides a new approach to determining in-process structural dynamics parameters based on a multivariate Newton-Raphson method. The physics-based model is combined with empirical records to extract reliable structural dynamics parameters inversely. Some examples based on synthetic data are presented to illustrate this inverse approach. Also, the algorithm is evaluated on an empirical data set and its ability to improve the stability boundary is verified.

In addition, this work includes defining and measuring the uncertainty of each structural dynamics parameter derived through the inverse approach. Here the main question is that to what extent, the uncertainty of each input parameter leads to the uncertainty in the SLD? The results derived from the algorithm were used to discover the sensitivity of the stability boundary with respect to each parameter. Two different methods were utilized for this purpose. Although the stability border shifts as any structural dynamics parameter changes, the results showed that the natural frequency is the most sensitive parameter.

Furthermore, this work investigated the feasibility of Machine Learning methods to predict tool temperature and maximum cutting force. Support Vector Regressor (SVR) and Gaussian Regression Process (GPR) were utilized in this study. The training/test data for building the ML models are generated from Finite Element (FE) simulations. The FE-generated data consists of cutting speed, uncut chip thickness, and rake angle as the input parameters. The response variables are the cutting force and maximum tool temperature. The optimal SVR and GPR models are selected using a grid search on the training data. The predictions on the test data sets show that both models perform well with high accuracy in predicting cutting force and maximum tool temperature. Between the two models, the mean square errors (MSE) for SVR are less than those for GPR.

CHAPTER 6: FUTURE WORK

A possible future direction of the presented work is to modify and examine the inverse approach during the machining process where more than one dominant mode is involved. Chatter in machining systems can arise from various vibration modes. In the presented study, the inverse method is examined under the condition that chatter originated from only one mode. However, it is possible to face a situation where more than one mode contributes to chatter. Future work could be conducted to explore this situation, and additional modifications might be needed to guarantee the success of the Newton-Raphson inverse method.

In another future direction, the impact of the feed rate may be investigated. The productivity of metal cutting is greatly influenced by the depth of cut, spindle speed, and feed rate. To ensure chatter-free cutting, it is important to determine the optimal values for these parameters. The cutting force required to generate chips increases as the feed rate increases. Consequently, changes in cutting forces could alter the dynamic behavior and stability properties of the machine. Further research could be done to examine how the feed rate impacts in-process structural dynamics parameters. This research would require a larger set of cutting test data at various feed rates. Additionally, the tool stick-out has a significant impact on the structural dynamics parameters. While the modes behave independently, certain modes are extremely influenced by the tool stick-out. It is worthwhile to examine how the tool stick-out affects the in-process structural dynamics parameters. This investigation would necessitate gathering comparable data sets for different stick-out lengths.

The presented study explains how the observed in-process parameters differ from the idle spindle parameters in milling. Also, as mentioned in the presented work, even for the same machine, three slightly different data sets were generated from three identical experiments. So a related question may be worth investigating: Comparing two different machines, if their cutting parameters and the idle spindle structural parameters are the same, are the in-process structural dynamics parameters the same in practice? In other words, to what extent the results would be different? This question requires a separate study in the future.

REFERENCES

[1] M. Eynian, "In-process identification of modal parameters using dimensionless relationships in milling chatter," *International Journal of Machine Tools and Manufacture*, vol. 143, pp. 49–62, 2019.

[2] M. Eynian, "[dataset] experimental stability boundary for a four-flute 10 mm tungsten-carbide end-mill in slot machining of aluminium 7075-t651," 2018.

[3] R. Faassen, "Chatter prediction and control for high-speed milling," *Eindhoven: Eindhoven University of Technology*, vol. 362, 2007.

[4] T. L. Schmitz and K. S. Smith, "Machining dynamics," *Springer*, p. 303, 2009.

[5] Y. Altintas and A. Ber, "Manufacturing automation: metal cutting mechanics, machine tool vibrations, and cnc design," *Appl. Mech. Rev.*, vol. 54, no. 5, pp. B84–B84, 2001.

[6] S. M. R. Mekarthy, M. Hashemitaheri, and H. Cherukuri, "A combined finite element and machine learning approach for the prediction of specific cutting forces and maximum tool temperatures in machining," *Electronic Transactions on Numerical Analysis*, vol. 56, pp. 66–85, 2022.

[7] C. E. Rasmussen, "Advances in gaussian processes," *Advances in Neural Information Processing Systems*, vol. 19, 2006.

[8] J. Yuan, K. Wang, T. Yu, and M. Fang, "Reliable multi-objective optimization of high-speed wedm process based on gaussian process regression," *International Journal of Machine Tools and Manufacture*, vol. 48, no. 1, pp. 47–60, 2008.

[9] M. Hashemitaheri, R. Mittal, H. Cherukuri, and R. Singh, "Extracting the in-process structural dynamics parameters in micro-milling operations," in *International Manufacturing Science and Engineering Conference*, vol. 85819, p. V002T05A052, American Society of Mechanical Engineers, 2022.

[10] M. Hashemitaheri, S. M. R. Mekarthy, and H. Cherukuri, "Prediction of specific cutting forces and maximum tool temperatures in orthogonal machining by support vector and gaussian process regression methods," *Procedia Manufacturing*, vol. 48, pp. 1000–1008, 2020.

[11] J. Tlusty, W. Zaton, and F. Ismail, "Stability lobes in milling," *CIRP Annals*, vol. 32, no. 1, pp. 309–313, 1983.

[12] S. Smith and J. Tlusty, "An overview of modeling and simulation of the milling process," 1991.

[13] S. Smith and J. Tlusty, "Update on high-speed milling dynamics," 1990.

[14] Y. Altintaş and E. Budak, "Analytical prediction of stability lobes in milling," *CIRP annals*, vol. 44, no. 1, pp. 357–362, 1995.

[15] J. Tlusty, "The stability of the machine tool against self-excited vibration in machining," *Proc. Int. Res. in Production Engineering, Pittsburgh, ASME*, vol. 465, 1963.

[16] S. Tobias and W. Fishwick, "Theory of regenerative machine tool chatter," *The engineer*, vol. 205, no. 7, pp. 199–203, 1958.

[17] E. Budak and Y. Altintas, "Analytical prediction of chatter stability in milling-part i: general formulation," 1998.

[18] E. Budak and Y. Altintas, "Analytical prediction of chatter stability in milling-part ii: application of the general formulation to common milling systems," 1998.

[19] Y. Altintas, G. Stépán, D. Merdol, and Z. Dombóvári, "Chatter stability of milling in frequency and discrete time domain," *CIRP Journal of Manufacturing Science and Technology*, vol. 1, no. 1, pp. 35–44, 2008.

[20] G. Stépán, "Delay-differential equation models for machine tool chatter," *Dynamics and chaos in manufacturing processes*, vol. 471152935, pp. 165–192, 1998.

[21] T. Insperger and G. Stépán, "Stability of the milling process," *Periodica polytechnica mechanical engineering*, vol. 44, no. 1, pp. 47–57, 2000.

[22] Y. Altintas, G. Stepan, E. Budak, T. Schmitz, and Z. M. Kilic, "Chatter stability of machining operations," *Journal of Manufacturing Science and Engineering*, vol. 142, no. 11, p. 110801, 2020.

[23] T. Moriwaki and K. Iwata, "In-process analysis of machine tool structure dynamics and prediction of machining chatter," 1976.

[24] A. Kwiatkowski and H. Al-Samarai, "Identification of milling machine receptances from random signals during cutting," *Annals of the CIRP*, vol. 16, no. 1, pp. 110–115, 1968.

[25] I. Zaghbani and V. Songmene, "Estimation of machine-tool dynamic parameters during machining operation through operational modal analysis," *International Journal of Machine Tools and Manufacture*, vol. 49, no. 12-13, pp. 947–957, 2009.

[26] H. Cao, B. Li, and Z. He, "Chatter stability of milling with speed-varying dynamics of spindles," *International Journal of Machine Tools and Manufacture*, vol. 52, no. 1, pp. 50–58, 2012.

[27] Y. Cao and Y. Altintas, "Modeling of spindle-bearing and machine tool systems for virtual simulation of milling operations," *International Journal of machine tools and manufacture*, vol. 47, no. 9, pp. 1342–1350, 2007.

[28] M. Rantatalo, J.-O. Aidanpää, B. Göransson, and P. Norman, "Milling machine spindle analysis using fem and non-contact spindle excitation and response measurement," *International Journal of Machine Tools and Manufacture*, vol. 47, no. 7-8, pp. 1034–1045, 2007.

[29] A. Matsubara, S. Tsujimoto, and D. Kono, "Evaluation of dynamic stiffness of machine tool spindle by non-contact excitation tests," *CIRP Annals*, vol. 64, no. 1, pp. 365–368, 2015.

[30] C.-H. Cheng, T. L. Schmitz, and G. Scott Duncan, "Rotating tool point frequency response prediction using rcsa," *Machining Science and Technology*, vol. 11, no. 3, pp. 433–446, 2007.

[31] V. Paliwal and N. R. Babu, "Prediction of stability lobe diagrams in high-speed milling by operational modal analysis," *Procedia Manufacturing*, vol. 48, pp. 283–293, 2020.

[32] O. Özşahin, E. Budak, and H. N. Özgüven, "In-process tool point frf identification under operational conditions using inverse stability solution," *International Journal of Machine Tools and Manufacture*, vol. 89, pp. 64–73, 2015.

[33] N. Grossi, L. Sallese, A. Scippa, and G. Campatelli, "Improved experimental-analytical approach to compute speed-varying tool-tip frf," *Precision Engineering*, vol. 48, pp. 114–122, 2017.

[34] N. Suzuki, Y. Kurata, T. Kato, R. Hino, and E. Shamoto, "Identification of transfer function by inverse analysis of self-excited chatter vibration in milling operations," *Precision Engineering*, vol. 36, no. 4, pp. 568–575, 2012.

[35] N. Grossi, F. Montevecchi, L. Sallese, A. Scippa, and G. Campatelli, "Chatter stability prediction for high-speed milling through a novel experimental-analytical approach.," *International Journal of Advanced Manufacturing Technology*, vol. 89, 2017.

[36] M. Postel, B. Bugdayci, F. Kuster, and K. Wegener, "Neural network supported inverse parameter identification for stability predictions in milling," *CIRP Journal of Manufacturing Science and Technology*, vol. 29, pp. 71–87, 2020.

[37] F. Burney, S. Pandit, and S. Wu, "A stochastic approach to characterization of machine tool system dynamics under actual working conditions," 1976.

[38] F. Burney, S. Pandit, and S. Wu, "A new approach to the analysis of machine-tool system stability under working conditions," 1977.

[39] G. E. Box, G. M. Jenkins, G. C. Reinsel, and G. M. Ljung, *Time series analysis: forecasting and control*. John Wiley & Sons, 2015.

[40] S. Cho, S. Asfour, A. Onar, and N. Kaundinya, "Tool breakage detection using support vector machine learning in a milling process," *International Journal of Machine Tools and Manufacture*, vol. 45, no. 3, pp. 241–249, 2005.

[41] Z. Jurkovic, G. Cukor, M. Brezocnik, and T. Brajkovic, "A comparison of machine learning methods for cutting parameters prediction in high speed turning process," *Journal of Intelligent Manufacturing*, vol. 29, no. 8, pp. 1683–1693, 2018.

[42] B. Lela, D. Bajić, and S. Jozić, "Regression analysis, support vector machines, and bayesian neural network approaches to modeling surface roughness in face milling," *The International Journal of Advanced Manufacturing Technology*, vol. 42, no. 11-12, pp. 1082–1088, 2009.

[43] Y.-W. Hsueh and C.-Y. Yang, "Tool breakage diagnosis in face milling by support vector machine," *Journal of materials processing technology*, vol. 209, no. 1, pp. 145–152, 2009.

[44] Z. Krizek, Z. Jurkovic, and M. Brezocnik, "Analytical study of different approaches to determine optimal cutting force model," *Archives of Materials Science*, vol. 28, no. 1-4, pp. 69–74, 2007.

[45] D. Kong, Y. Chen, and N. Li, “Gaussian process regression for tool wear prediction,” *Mechanical systems and signal processing*, vol. 104, pp. 556–574, 2018.

[46] G. Zhang, J. Li, Y. Chen, Y. Huang, X. Shao, and M. Li, “Prediction of surface roughness in end face milling based on gaussian process regression and cause analysis considering tool vibration,” *The International Journal of Advanced Manufacturing Technology*, vol. 75, no. 9-12, pp. 1357–1370, 2014.

[47] J. Liu, *Sequential Design for Quantification of Stability in Machining Process: Fusion of Physical and Statistical Models*. PhD thesis, State University of New York at Binghamton, 2018.

[48] M. Lamraoui, M. Barakat, M. Thomas, and M. E. Badaoui, “Chatter detection in milling machines by neural network classification and feature selection,” *Journal of Vibration and Control*, vol. 21, no. 7, pp. 1251–1266, 2015.

[49] J. Friedrich, J. Torzewski, and A. Verl, “Online learning of stability lobe diagrams in milling,” *Procedia CIRP*, vol. 67, pp. 278–283, 2018.

[50] J. Friedrich, C. Hinze, A. Renner, A. Verl, and A. Lechler, “Estimation of stability lobe diagrams in milling with continuous learning algorithms,” *Robotics and Computer-Integrated Manufacturing*, vol. 43, pp. 124–134, 2017.

[51] H. Cherukuri, E. Perez-Bernabeu, M. Selles, and T. Schmitz, “Machining chatter prediction using a data learning model,” *Journal of Manufacturing and Materials Processing*, vol. 3, no. 2, p. 45, 2019.

[52] J. Karandikar, A. Honeycutt, T. Schmitz, and S. Smith, “Stability boundary and optimal operating parameter identification in milling using bayesian learning,” *Journal of Manufacturing Processes*, vol. 56, pp. 1252–1262, 2020.

[53] H. Cao, Y. Yue, X. Chen, and X. Zhang, “Chatter detection in milling process based on synchrosqueezing transform of sound signals,” *The International Journal of Advanced Manufacturing Technology*, vol. 89, no. 9, pp. 2747–2755, 2017.

[54] N.-C. Tsai, D.-C. Chen, and R.-M. Lee, “Chatter prevention for milling process by acoustic signal feedback,” *The International Journal of Advanced Manufacturing Technology*, vol. 47, no. 9, pp. 1013–1021, 2010.

[55] K. Li, S. He, B. Li, H. Liu, X. Mao, and C. Shi, “A novel online chatter detection method in milling process based on multiscale entropy and gradient tree boosting,” *Mechanical Systems and Signal Processing*, vol. 135, p. 106385, 2020.

[56] Y. Fu, Y. Zhang, H. Zhou, D. Li, H. Liu, H. Qiao, and X. Wang, "Timely online chatter detection in end milling process," *Mechanical Systems and Signal Processing*, vol. 75, pp. 668–688, 2016.

[57] G. Chen and Q. Zheng, "Online chatter detection of the end milling based on wavelet packet transform and support vector machine recursive feature elimination," *The International Journal of Advanced Manufacturing Technology*, vol. 95, no. 1, pp. 775–784, 2018.

[58] L. Ding, Y. Sun, and Z. Xiong, "Early chatter detection based on logistic regression with time and frequency domain features," in *2017 IEEE International Conference on Advanced Intelligent Mechatronics (AIM)*, pp. 1052–1057, IEEE, 2017.

[59] R. Rusinek and P. Lajmert, "Chatter detection in milling of carbon fiber-reinforced composites by improved hilbert–huang transform and recurrence quantification analysis," *Materials*, vol. 13, no. 18, p. 4105, 2020.

[60] B. Denkena, B. Bergmann, and S. Reimer, "Analysis of different machine learning algorithms to learn stability lobe diagrams," *Procedia CIRP*, vol. 88, pp. 282–287, 2020.

[61] J. P. Patel, *Finite Element Studies of Orthogonal Machining of Aluminum Alloy A2024-T351.* PhD thesis, The University of North Carolina at Charlotte, 2018.

[62] ABAQUS, "Abaqus 2017 documentation," 2017.

[63] T. Mabrouki, F. Girardin, M. Asad, and J.-F. Rigal, "Numerical and experimental study of dry cutting for an aeronautic aluminium alloy (a2024-t351)," *International Journal of Machine Tools and Manufacture*, vol. 48, no. 11, pp. 1187–1197, 2008.

[64] X. Teng and T. Wierzbicki, "Evaluation of six fracture models in high velocity perforation," *Engineering Fracture Mechanics*, vol. 73, no. 12, pp. 1653–1678, 2006.

[65] X. Yang and C. R. Liu, "A new stress-based model of friction behavior in machining and its significant impact on residual stresses computed by finite element method," *International Journal of Mechanical Sciences*, vol. 44, no. 4, pp. 703–723, 2002.

[66] N. Zorev, "Inter-relationship between shear processes occurring along tool face and shear plane in metal cutting," *International research in production engineering*, vol. 49, pp. 143–152, 1963.

[67] G. R. Johnson and W. H. Cook, "Fracture characteristics of three metals subjected to various strains, strain rates, temperatures and pressures," *Engineering fracture mechanics*, vol. 21, no. 1, pp. 31–48, 1985.

[68] J. Patel and H. P. Cherukuri, "Chip morphology studies using separate fracture toughness values for chip separation and serration in orthogonal machining simulations," in *ASME 2018 13th International Manufacturing Science and Engineering Conference*, pp. V002T04A031–V002T04A031, American Society of Mechanical Engineers, 2018.

[69] M. Asad, F. Girardin, T. Mabrouki, and J.-F. Rigal, "Dry cutting study of an aluminium alloy (a2024-t351): a numerical and experimental approach," *International Journal of Material Forming*, vol. 1, no. 1, pp. 499–502, 2008.

[70] M. Awad and R. Khanna, "Support vector regression," in *Efficient Learning Machines*, pp. 67–80, Springer, 2015.

[71] V. Cherkassky and Y. Ma, "Practical selection of svm parameters and noise estimation for svm regression," *Neural networks*, vol. 17, no. 1, pp. 113–126, 2004.

[72] A. Yeganefar, S. A. Niknam, and R. Asadi, "The use of support vector machine, neural network, and regression analysis to predict and optimize surface roughness and cutting forces in milling," *The International Journal of Advanced Manufacturing Technology*, pp. 1–15, 2019.

[73] C. K. Williams and C. E. Rasmussen, *Gaussian processes for machine learning*, vol. 2. MIT press Cambridge, MA, 2006.

[74] E. Schulz, M. Speekenbrink, and A. Krause, "A tutorial on gaussian process regression: Modelling, exploring, and exploiting functions," *Journal of Mathematical Psychology*, vol. 85, pp. 1–16, 2018.

[75] S. P. Adam, S.-A. N. Alexandropoulos, P. M. Pardalos, and M. N. Vrahatis, "No free lunch theorem: A review," *Approximation and Optimization: Algorithms, Complexity and Applications*, pp. 57–82, 2019.

[76] R. Marandi, "Experimental study of chatter in milling," *Working Paper*, 2023.

[77] Y. Altintas, *Manufacturing automation: metal cutting mechanics, machine tool vibrations, and CNC design*. Cambridge university press, 2012.